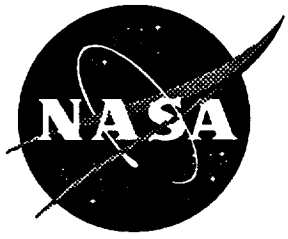
IN-34
033251

NASA Contractor Report 201693



Shock Tunnel Studies of Scramjet Phenomena 1994

Supplements 11 and 12

R. G. Morgan, A. Paull, and R. J. Stalker
The University of Queensland, Brisbane, Australia

Grant NAGW-674
April 1997

National Aeronautics and
Space Administration
Langley Research Center
Hampton, Virginia 23681-0001

SHOCK TUNNEL STUDIES OF SCRAMJET PHENOMENA 1994
NASA GRANT NAGW-674 - SUPPLEMENT 12

Following the format of previous reports, this consists of a series of reports on specific projects. After a brief introduction on each project, the project reports follow in the order of the headings in the introduction.

"Program A" corresponds to work funded jointly by NAGW-674 and Australian sources, and "Program B" to that funded by Australian sources alone.

PROGRAM A

(i) Hypersonic Simulation in a New Large Scale Experimental Facility
(C.J. Doolan and R.G. Morgan)

(ii) Design and Construction of the X-2 Two-Stage Free Piston Driven Expansion Tube
(C.J. Doolan)

A new expansion tube facility has been built, and is in the process of being commissioned. It has a bore of 90 mm, and has been designed for peak rupture pressures of 100 Mpa. It is configured with multiple sections and diaphragm location stations to give optimised performance over a range of sub and superorbital conditions. It has a compound piston arrangement for a two stage compression, designed to maximise the length of shock expansion tube which can be driven within a fixed total facility length. Experiments have been successfully performed with a dummy first stage piston, and a rubber energy absorbing brake. The results agree well with a one-dimensional stress wave model of the piston impacting on the rubber, and codes for piston motion. Strain of the rubber is restricted to approximately 20% at which level no damage is to be expected in the buffer material, and none has been observed, indicating that the mechanism will be fully reuseable. Testing of the two stage piston is scheduled for September 1995. More details available Doolan and Morgan, Colorado 1994 and progress report Con Doolan 1995.

Of special relevance to the NASA program is the provision for a supplementary shock heated driver section which can provide a sound speed buffer to filter noise from the driver section, and prevent it reaching the test section. Potentially this permits testing at sub orbital speeds with high temperature driver conditions which have been previously been found to prelude satisfactory operation. If this operating mode is shown to be viable, then the total pressure simulating capability of the expansion tube will be greatly increased. Theoretical and experimental study of this concept is underway. Preliminary results on the X1 configuration of the TQ facility have demonstrated clean pitot traces at speeds of about 6km/sec, with heated driver gas. This condition was found unworkable by Allan Paull in his original investigation into noise propagation into expansion tubes. A useable test flow has not yet been demonstrated through heat transfer measurements, and the test time, as expected, was greatly reduced. Study is continuing with the aim of scaling the concept up to larger facilities which may create a greater range of perturbation frequency, and defining the test time reduction associated with the technique.

Boundary Layer Blockage in Expansion Tube Nozzles
(O. Sudnitsin and R.G. Morgan)

The realisation of higher pressures in expansion tubes opens the option of using expansion nozzles to create a greater range of test conditions, and in particular to increase the geometric size of the test core. The question of where to start the expansion is being investigated under this grant by Olga Sudnitsin, supervisor Richard Morgan.

Three configurations are possible, with the flow expansion occuring at the driver coupling to the shock tube, the acceleration tube inlet, or the acceleration tube outlet. A perfect gas 1D non-dimensional analysis has been performed to assess which configuration is likely to be attractive with the first selection criteria being the overall nose to tail pressure ratio between driver and test gas. If the operating pressures look viable, then further investigation of other considerations, such as test time, geometrical complexity, viscous effects, suitability of test flow for combustion purposes and provision of matched interfaces for filtering flow disturbances is done. The preferred option is seen to be strongly dependent on flow velocity, which is conveniently normalised by the driver speed of sound.

For the first experimental study, the configuration chosen uses the nozzle attached to the acceleration tube exit. This is seen to perform reasonably well in the medium speed range (test speed/driver sound speed 1.5 to 2.5) and is the simplest and cheapest to implement. A conical nozzle with 9/1 area ratio has been designed for the X1/TQ expansion tube and is currently under construction. With the expansion of high Mach number flows, boundary layer blockage can be significant. A von Karmen integral method was used to estimate the development of boundary layer displacement thickness during the expansion, whcih was incorporated into a one-dimensional analysis to predict the nozzle exit conditions. The nozzle is instrumented to give wall static pressure readings along the expansion surface, which will be used in conjuction with test section pitot measurements to verify the analysis.

(iii) Skin Friction in a Thrust Nozzle
Lift, Drag and Thrust Measurement in a Hypersonic Impulse Facility
(S.L. Tuttle, D.J. Mee and J.M. Simmons)

Measurement of the thrust on a two-dimensional thrust nozzle is reported here. There was considerable difficulty associated with the need to make the nozzle dynamically independent of the combustion chamber, but the results finally obtained demonstrate that a local skin friction coefficient of 0.003 appears to be adequate for thrust nozzles. Results are also presented demonstrating the use of the stress wave force balance for simultaneously measuring lift and drag.

PROGRAM B

(i) Mixing and Combustion

(a) Measurement of Scramjet Thrust in Shock Tunnels
(R.J. Stalker, J.M. Simmons, A. Paull and D.J. Mee)

Using results obtained in shock tunnels, some approximate criteria regarding model size and nozzle reservoir pressure for testing of complete scramjet vehicle configurations are obtained. Then the principle of the stress wave force balance, for measuring the axial force on such model configurations in millisecond test times, is explained. The history of the development of the stress wave force balance is then briefly outlined, and measurements of thrust/drag on an axisymmetric scramjet configuration are presented, showing net positive thrust at velocities up to 2.4 km/sec.

(b) Scramjet Thrust Measurement in a Shock Tunnel
(A. Paull, R.J. Stalker and D.J. Mee)

This note reports the same measurements of scramjet thrust/drag as the previous paper. A luminosity photograph of the model during a test which produced thrust is also shown but, as it is a time integrated photograph, it should be interpreted with caution.

(c) Supersonic Combustion Ramjet Propulsion Experiments in a Shock Tunnel
(A. Paull, R.J. Stalker and D.J. Mee)
(Published in the Journal of Fluid Mechanics, August 1995)

This paper considers the aerodynamic-forces, both external and internal, which govern the net production of thrust for an axisymmetric fully integrated scramjet configuration. Measurements were found to be consistent with established theoretical models, used with some simplifying assumptions. The model was chosen for ease of manufacture and analysis and no serious attempt was made to optimize the shape. Therefore the net inviscid drag was substantial. Apart from this, the skin friction drag in the combustion chambers made substantial contribution to the total drag, and this increased when combustion took place. The skin friction in the thrust nozzle made a small contribution to the drag. The fuel used was 87% hydrogen, with 13% silane and yielded a maximum specific impulse of 175 sec.

(d) Species Measurements in a Hypersonic, Hydrogen-Air, Combustion Wake
(K.A. Skinner and R.J. Stalker)

Measurements of species concentrations in a two-dimensional wake formed by the injection of hydrogen from the trailing edge of an injection strut spanning the flow are reported here. The stagnation enthalpy, and hence the free stream temperature, was varied over a range from which no combustion occurred to where 50% combustion of the mixed hydrogen took place. It was found that the amount of hydrogen mixed was independent of the amount injected.

(ii) Skin Friction and Heat Transfer Measurements
A Skin Friction Gauge for Impulsive Flows
(C.P. Goyne, A. Paull and R.J. Stalker)

This reports further development of the skin friction gauge. The gauge can now be calibrated by a method which is independent of the flow. It is still apparently subject to thermal effects in the flow, but when steps are taken to correct the results for this, reasonable measurements of the turbulent skin friction are obtained.

(ii) Mass Spectrometric Measurements
Mass Spectrometer Measurements of Test Gas Composition in a Shock Tunnel
(K.A. Skinner and R.J. Stalker)

Mass spectrometer measurements of the concentration of 0_2, N0, and 0 relative to N_2, at stagnation enthalpies up to 12.5 MJ/kg, have been taken in a hypersonic nozzle. They show that the concentration of N0 is approximately 60% higher than the values predicted by using conventional chemical kinetics models, and that the dissociation of oxygen in the free stream is delayed to considerably higher enthalpies than predicted.

AIAA 94-2492

Hypervelocity Simulation in a New Large Scale Experimental Facility

C. J. Doolan and R. G. Morgan
The University of Queensland
Brisbane, Australia

18th AIAA Aerospace Ground Testing Conference
June 20-23, 1994
Colorado Springs, Colorado

HYPERVELOCITY SIMULATION IN A NEW LARGE SCALE EXPERIMENTAL FACILITY

AIAA-94-2492-CP

Con J. Doolan* & Richard G. Morgan**
Department of Mechanical Engineering
The University of Queensland
Brisbane, Australia

Abstract

This paper discusses a proposed new large scale free-piston driven expansion tube facility (X-3) which can operate in either a super or sub-orbital mode. This will allow experimentation into super-orbital aerobrake flowfields along with studies into sub-orbital hypersonic propulsion. In order to decrease facility cost and complexity, a new two-stage driver concept is utilised.

Simple, one-dimensional calculations are presented which predict test-time and test flow conditions within this new facility. The amount and quality of the test-time is seen to be dependant on interactions between various gas dynamic events occurring within the expansion tube. Results show that approximately 200 μs of test-time is available at the super-orbital (13-16 km/s) conditions. It is predicted that there is an order of magnitude increase in the stagnation pressure over reflected shock tunnels when operating in the sub-orbital mode.

As a number of new concepts are to be used in the design of X-3, an experimental prototype (X-2) incorporating these features is currently under construction. Pertinent design and technology issues of this machine are also presented.

Nomenclature

P_1	Driver gas pressure.
P_2	Reservoir pressure.
x	Distance piston has travelled.
	Tube spatial coordinate (m).
L	Driver length.
t	Tube temporal coordinate (s).
u	Gas velocity (m/s).
a	Gas speed of sound (m/s).
H_0	Stagnation enthalpy (MJ/kg).
A_R	Two-stage driver area ratio.
M	Mach Number
Greek	
λ	Compression ratio.
λ_1	First stage compression ratio.
γ	Ratio specific heats.
Subscripts	
1	Region before unsteady expansion.
2	Region after unsteady expansion.
	Sub-orbital shock heated test gas region.
3	Expanded driver gas region.

Introduction

Recent interest in interplanetary exploration, particularly manned Mars missions, has prompted researchers to develop feasible technical architectures for such journeys. There are many factors which will determine the safest and most economical flight plan,[1,2] including exposure time to microgravity and cosmic radiation, propulsion technology and initial mass in low Earth orbit (IMLEO). The IMLEO has emerged as one of the most important parameters in determining overall cost and flight time[1] and 10^6 kg is commonly regarded as the practical upper limit for manned Mars missions.

Walberg[2] shows that for most manned Mars mission scenarios propulsive chemical vehicles may not be feasible from a mass standpoint alone. However, IMLEOs fall below the 10^6 kg 'barrier' when a combination of either chemical or nuclear thermal propulsion is used with the aerobraking manoeuvre. Aerobraking involves the use of atmospheric drag instead of propulsive braking to either insert the incoming vehicle into a convenient planetary orbit or to directly descend to the planet's surface. In fact, it has been shown that aerobraking can reduce the IMLEO by 20-60%.[3]

Most proposed aerobraking scenarios use the manoeuvre at both the destination planet and Earth return orbital insertion points. However, the entry speeds encountered are extremely high, ~13 km/s for Earth return and

* Graduate Student, Student Member AIAA
** Senior Lecturer, Member AIAA

Copyright © 1994 by the American Institute of Aeronautics and Astronautics Inc. All Rights Reserved.

~8.5 km/s for Mars entry.[2] Despite the advances in aerothermodynamic analysis and experimentation over the last three decades, the flowfield around an aerobraking vehicle returning to Earth at such high speed is still largely not understood.

Computational fluid dynamicists have tackled this problem (Refs. 4-7) with some success, however as with all CFD work, the results need to be calibrated against physical data gained in wind tunnels, hypervelocity ranges or flight tests. Clearly, ground testing in high speed wind tunnels provides a lower cost option than range or flight tests. Nevertheless, there are few wind tunnels existing or planned which can adequately simulate the required super-orbital re-entry velocities in air.

One method of generating short duration steady gas flow at super-orbital speed is through the use of the free-piston driven super-orbital expansion tube (SOET) (fig. 1). This impulsive device is a derivative of the well known expansion tube concept. It has a number of distinct advantages over other short duration test facilities including a longer test time at super orbital speed. Calculations show an order of magnitude increase in test times over the simple shock tube coupled to a high energy driver. The SOET does not produce the shock heated plasma associated with the high shock speeds required to generate super-orbital velocities in shock tubes and reflected shock tunnels. Rather the SOET accelerates the test gas through an unsteady expansion which does not require the flow to be stagnated, thereby reducing radiation losses. Finally, the SOET also has the added advantage of increased stagnation enthalpy by using the unsteady expansion principle.

A hypersonic vehicle using an airbreathing scramjet propulsion system offers a low cost alternative to conventional chemical rocketry.[8] Through research over the last decade, scramjet performance seems to be well understood up to a flight Mach number of about 12. At higher flight Mach numbers simulation in existing ground test facilities is not adequate for realistic scramjet ascents[9]. For example, the free-piston driven reflected shock tunnel is quite capable of achieving the flow energy (stagnation enthalpy). However, stagnation pressure is limited to around 120 MPa[9] which is too small for scramjet ascents beyond Mach 12.

As the test flow in an expansion tube is processed through an unsteady expansion, it is predicted that given an adequate high performance driver (pressure and temperature), the necessary stagnation enthalpy *and* pressure will be simulated for a complete scramjet ascent trajectory. Thus, the expansion tube/tunnel is an attractive propulsion research facility option due to its performance characteristics and its relatively chemically clean (low level dissociation) flow.[10]

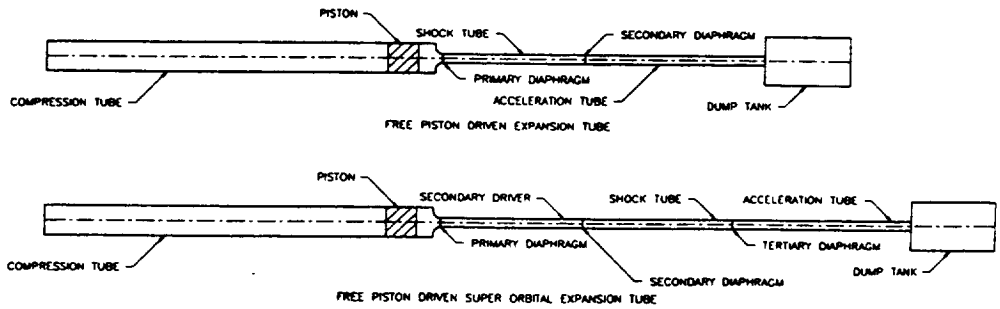


Figure 1. Expansion Tube and SOET.

It is now proposed that a new large scale hypervelocity facility can be built which can simulate the flow conditions at the sub-orbital (< 7 km/s) and at the super-orbital (12 - 16 km/s) range of flight velocities. In order to do this the device will incorporate a large free piston driver which will operate an expansion tube in either sub-orbital or super-orbital modes. Operation modes are determined by the number and placement of diaphragms. It will be shown that test-time can be optimised by using a principle termed here as 'active geometry'.

This new tunnel will be the largest in the 'X' series of expansion tube facilities. Currently in operation is X-1. X-1 is a pilot facility (37mm bore) which has demonstrated that super orbital simulation is possible using unique driver/shock tube arrangements.[11] X-2 is medium sized facility of 85 mm bore which is currently under construction. The purpose of X-2 is to optimise, on a smaller scale, the new driver concepts and shock tube arrangements to be used on the large scale facility, X-3. X-3 will have a large bore (~200 mm) in order to fit large models in the test section. The design temperature and pressure of its driver will be approximately 6000 K and 200 MPa respectively in order to drive the necessary shock speeds for super-orbital simulation and sub-orbital stagnation pressure objectives.

This paper discusses new driver concepts and shock tube arrangements to be used for X-3. An expected operating envelope will also be presented along with design and technology issues associated with the mid-sized X-2.

Two-stage Free-Piston Driver

In order to build the X-3 within typical university budgets (10^5's instead of 10^6's) design changes are required which alter the structure of the usual free-piston driven facility. Most free-piston drivers in the past have employed a large area reduction between the driver and driven tubes. This allows certain benefits such as increased shock speed (for a given driver-to-driven tube fill pressure ratio) and a long 'holding time' characteristic due to the steady flow process present between the driver and the diaphragm throat. The benefits the area change provides have virtually made it a standard feature of free-piston driver designs.[12,13]

However, the large change in section at the highly pressurised primary diaphragm station induces large axial and circumferential loads. The stresses caused by these loads can be reduced by using expensive thick-walled high tensile steel or by simply eliminating the area change. By doing away with the area change a large part of the facility cost has been removed but a different design attitude is required in order to deal with the constraints of the constant area driver.

Specifically, there are two adverse influences allied with the constant area driver. Firstly, a drop in performance is expected resulting in approximately double the required burst pressure. This is discussed both theoretically and experimentally by Morgan and Stalker.[11] The driver must now be designed for higher pressure which partially offsets its advantage.

In conventional free piston designs, piston velocity helps maintain a constant driver pressure after diaphragm rupture. If there is sufficient area change the expansion waves travelling upstream from the burst diaphragm are cancelled by the forward movement of the piston. This creates a 'holding time' which is usually much longer than the test flow duration. This characteristic essentially produces a constant pressure driver. In order to duplicate this with a constant area driver, piston velocities approaching the driver speed of sound (~5000 m/s) are required. As such high piston velocities are clearly impractical, an adequate volume of hot driver gas needs to present before the primary diaphragm bursts so the reflection of the unsteady expansion fan is delayed long enough to simulate an adequate 'holding time'. Test-time is directly related to this pseudo holding-time as will be shown in later sections.

For 75 m of total facility length, the approximate length of hot driver gas necessary for an adequate test-time over a range of conditions is 1.0 m. Consequently if a conventional single bore driver is used at a compression ratio of 100 (required for previously stated conditions), the corresponding overall length of driver equipment is 100 metres. Most research institutions would find it hard to raise the capital or the laboratory space for such a machine. Instead, radical changes initially proposed by Morgan[14], are performed to the layout of a single bore driver.

These design modifications consist of a compound isentropic free-piston driver which employs an area change between two, in-line, compression stages (fig. 2(a)), similar to a two stage compressor. Utilising a concentric two-piece piston, the two stage driver is capable of achieving the required volume of gas before the primary diaphragm by simply being able to compress a larger initial driver volume to high temperatures through high compression ratio's (λ=60-100).

Figure 2(b) shows a typical pressure distance plot for a free-piston driver. Noticing that during the early stages of the compression process swept volume is high and pressure rise is only moderate, the first stage of the two-stage driver is of large bore and light construction. The position of area change is chosen so that the pressures on either side of the compound piston are approximately

matched. This location is the point where the piston attains its maximum kinetic energy - 80-95% of the available reservoir work. Now, this kinetic energy must be transferred to the driver gas ahead of the piston. This is achieved by the compound piston separating at the area change and allowing the inner piston to compress the driver gas to the desired conditions. In order to maximise performance, the inner piston must contain a major proportion of the compound piston mass. If this is not the case, reservoir work is wasted by stopping the outer piston at the area change. It is planned to decelerate the outer piston at the tube interface by a combination of gas and rubber buffers.

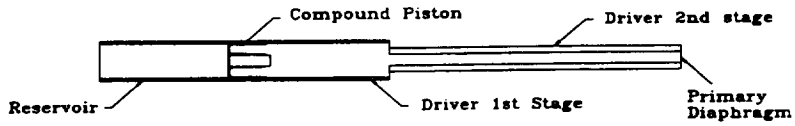


Figure 2(a). Two Stage Driver Concept.

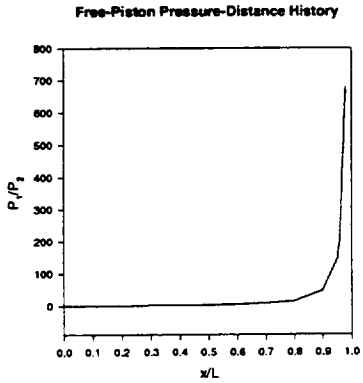


Figure 2(b).

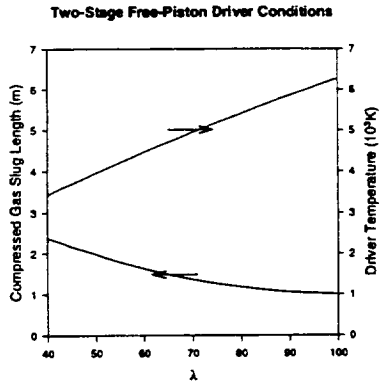


Figure 3.

Figure 3 displays the expected driver conditions for an anticipated driver length of 25 metres. Calculations were performed using a perfect gas analysis assuming isentropic flow. A two-stage driver geometry of $\lambda_1 = 6$ and $A_R = 9$ was assumed for design reasons given in the text.

Expansion Tube Test-Time Optimisation

Given a particular driver condition (figure 3), there exists an optimal arrangement of shock tubes which will give a maximum amount of test-time for a particular flow enthalpy (ie. choice of shock speeds). In order to explain this phenomenon, it is necessary to examine the flow interactions within an expansion tube.

During the operation of an expansion tube, any region containing a density discontinuity is a potential location for wave reflection.[15]

Simple unsteady wave trajectories can be described by one-dimensional gas dynamics using the characteristic equation,

$$\frac{dx}{dt} = u \pm a \qquad (1)$$

Ideally, at diaphragm rupture an unsteady expansion fan centred at the diaphragm propagates through its surrounding fluid medium. the wave propagates as a *u-a* wave, that is, the negative part of equation (1). When the leading edge of this wave encounters a density discontinuity such as a contact surface or the front face of the piston, the wave is partially reflected and becomes what is known as a cross characteristic or *u+a* wave (Fig. 4). The reflected wave now travels back through the unsteady expansion forming the leading edge of an analytically indeterminate non-simple wave. However, the leading edge of this wave is still determinate and its trajectory path through an unsteady expansion can be described by the equation[15]

$$t_2 = t_1 \left\{ \frac{a_2}{a_1} \right\}^{\frac{\gamma+1}{2(1-\gamma)}} \qquad (2)$$

This non-simple wave leading edge emerging from the unsteady expansion is now travelling faster than the upstream fluid so it can overtake other flow events and, if unaccounted for, severely reduce the available test-time (fig. 4(a)).

It can now be seen that the available test-time has a strong dependence on the interaction between the unsteady expansion waves and the fluid interfaces of an expansion tube flow. If the lengths of tube which represent the different portions of the expansion tube can be arranged to suit the specific requirements of the flow then the test-time can be optimised. That is, if the leading edge of the non-simple wave caused by the reflection off a previous density discontinuity can arrive at the same time or after the interface arrives at the leading edge of the next centred unsteady expansion fan (fig. 4(b)), then test-time can be maximised. However, for a given set of shock tube lengths, the condition where the waves are aligned for optimal test flow can only occur at a given test-flow enthalpy or choice of fill pressures.

For use as a versatile research tool at varying enthalpy conditions, it is planned to use multiple diaphragm stations along the length of the facility and use only those which provide optimal test-times at each condition. This concept has been termed the 'active geometry' expansion tube[16].

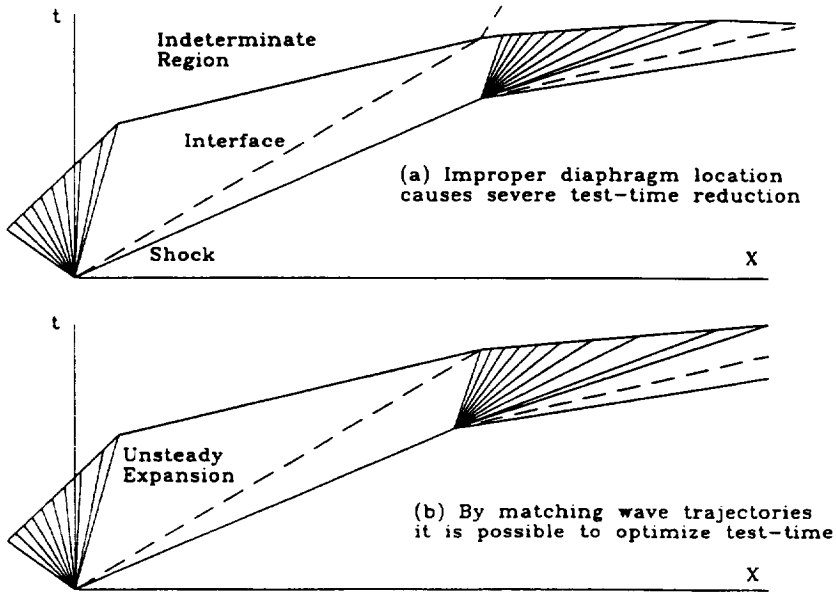


Figure 4. Test-Time Optimisation in an Expansion Tube.

X-3 Test Flow Conditions

Super-orbital Mode

Due to the high shock speeds needed for super-orbital simulation, a perfect gas analysis is not appropriate for determination of test flow conditions. Incorporation of high temperature gas effects and viscous effects within the tube are necessary to estimate the test-time as well as the test conditions.

High temperature or real gas effects alter the predicted (perfect gas) conditions which in turn affect the trajectories of the unsteady wave characteristics which are vital in test-time calculations. Following the results of Neely and Morgan[17] equilibrium chemistry is assumed in air across both the unsteady shock wave and through the unsteady expansion into the test section. Calculations are performed using a real gas flow solver known as EQSTATE[18]. It is expected to fill the secondary driver and acceleration tube with helium which should not experience noticeable real gas effects.

Boundary layers within the shock tube act as an aerodynamic sink and absorb mass from the region between the shock and the contact surface. This has the consequence of attenuating the shock wave and accelerating the contact surface until they are both travelling at the same speed and are separated by some limiting value. Mirels[19] theory has long been used as a tool for determining test-time in shock tubes. Mirels' analysis is extended here to determine the test-times in the proposed expansion tube arrangements.

Experimental evidence[11,17] has shown that the full Mirels analysis need only be performed in the air filled shock tube. The high shock speeds present in the low pressure acceleration tube (helium filled) produce an almost instantaneous matching of shock and interface speeds. This condition has been noticed experimentally and is most easily analysed by ignoring the acceleration tube interface trajectory altogether when operating at super-orbital velocities.

Preliminary Lagrangian x-t diagrams for the super-orbital mode are shown in figure 5. The two conditions shown are at (a) 13 km/s (H_0 = 100 MJ/kg) and (b) 16 km/s (H_0 = 180 MJ/kg). Condition (b) is expected to be the operational limit of the new X-3 facility due to boundary layers in the acceleration tube. Simple calculations based on a turbulent (Mirels[19]) boundary layer (assuming a 1/7th power law velocity profile with the Howarth transformation[20] and equilibrium chemistry[18]) suggest that the acceleration tube has half the tunnel bore as a useable test-core at the 180 MJ/kg condition.

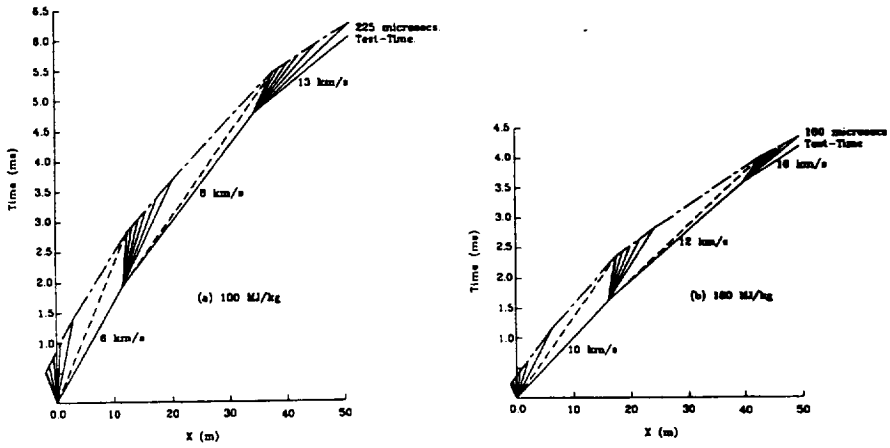


Figure 5. Expected X-3 Super-Orbital Test Flow Duration.

As shown in figure 5, the expected test-time is around 200μs for super-orbital simulation. No other existing or planned facility could produce such long test-times at comparable speeds without severely compromising the chemical integrity of the flow. Figure 6 compares the equilibrium test-gas compositions of both the X-3 SOET and a conventional shock tube at the 100 MJ/kg condition. These calculations were performed using the real gas solver EQSTATE[18] mentioned earlier assuming the same test-section static pressure (1.5 atm) in each case. EQSTATE solves conservation equations using an 8 species air model which includes ions and electrons. It can be seen that the SOET has much lower levels of dissociation than a conventional shock tube at high enthalpy.

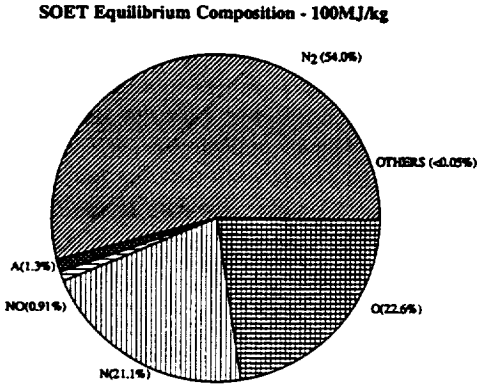


Figure 6(a). SOET Test Gas Composition. (% Mass Fraction)

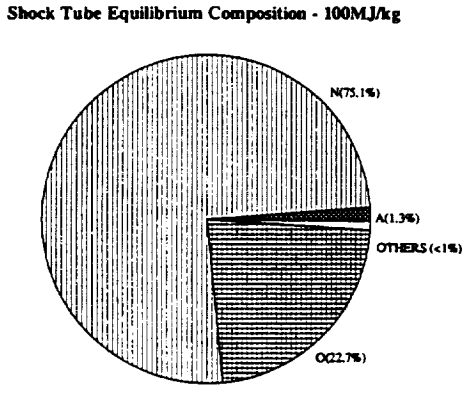


Figure 6(b). Shock Tube Test Gas Composition. (% Mass Fraction)

Sub-Orbital Mode

High enthalpy reflected shock tunnels are limited in their ability to simulate supersonic combustor flow stagnation pressures above a flight Mach number of about 12. The stagnation pressure achievable in a reflected shock tunnel is indicative of the nozzle supply pressure attained immediately after shock reflection. A typical structural design limit for the driver and nozzle supply region of a large scale facility is 200 MPa. In practice it has been found that operation at the design limit causes extreme erosion of the shock tube reservoir and nozzle throat regions and a more conservative value of 120 MPa has been found to be a maximum routine operating pressure.

Perfect gas computations show that by coupling the regular expansion tube to a high performance two-stage driver, both energy and pressure can be simulated for the entire flight path of an ascending airbreathing engine. The moderate shock speeds associated with suborbital operating conditions (2-4 km/s) theoretically cause negligible viscous and chemical action within the shock tube.

In order to assess the applicability of the expansion tube to scramjet combustor ascent trajectories, it has been necessary to assume a general flight path for such a vehicle. Bakos[9] has determined an optimised flight path of a generic scramjet powered vehicle. In this trajectory, the combustor inlet pressure has been constrained to be one atmosphere for all flight conditions. This value is generally accepted as necessary to ensure near-equilibrium combustion within one metre of entering the combustor. Also the flight path has been modified to suit the aeroheating limitations of likely aerospace materials. From this study, a typical scramjet combustor is expected to experience a maximum total pressure of 2400 atmospheres.

An important factor in the selection of operating conditions for expansion tubes is achieving the correct driver speed of sound to minimise noise in the test flow. Paull[15,21] identified a mechanism whereby transverse waves originating in the driver gas can focus to a dominant frequency when passed through an unsteady expansion. These waves, if left unattended, can stay with the test-gas and produce unacceptable noise levels in the test-flow. It has been shown by Paull that these disturbances can be attenuated by setting up a gas dynamic filter across the driver gas/test gas interface. To provide an effective gas

dynamic filter, a speed of sound increase across the interface ($a_3/a_2 < 1$) is required[21]. For a given test condition, the noise is controlled by the Mach number the driver gas is expanded to behind the test gas in the shock tube. Experimental results using the small bore X-1 indicate the driver gas needs to expanded to about $M_3 = 4$.[15] However, theoretically it has been postulated that the driver gas expansion can be reduced to approximately $M_3 = 2.3$[21] when using a large bore constant area driven expansion tube. Most probably the amount of driver gas expansion lies in between these two limits. Figure 7 compares the test conditions in X-3 operating in the sub-orbital mode at two different expanded driver gas Mach numbers with the maximum flight conditions determined by Bakos. It can be seen from the calculations presented here that X-3 should be able to simulate both energy and pressure requirements for a hypersonic airbreathing propulsion system over its entire flight path.

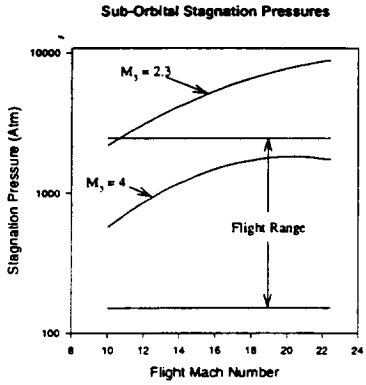


Figure 7.

Figure 8 shows the expected test-times for the various flight Mach numbers for the chosen scramjet ascent trajectory. Test-times are determined using the active-geometry technique discussed earlier. In each case, the driver compression ratio is modified so that test-time is maximised for approximately 50 m of shock tube space. It can be seen that test-times are of the same order or larger than other free-piston impulse facilities operating at these enthalpy conditions.

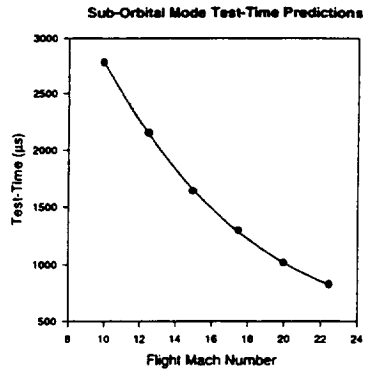


Figure 8.

X-2 Design and Technology Issues

The test-times and conditions shown above have been computed using certain assumptions about the performance of the new facility. Firstly, the driver has been assumed to be isentropic with no losses. This is an idealistic assumption, however it is difficult to quantify the losses on a new facility, especially with a previously untried driver concept. Also, the mechanisms that occur in a constant area driven shock tube must be better understood so more accurate determination of test-time and more importantly, diaphragm locations for the large scale X-3 can be made. Practical issues such as diaphragm opening times, contamination of test gas and diffusive mixing at the gas interfaces all need more understanding in expansion tube situations along with their interactions with a two stage driver.

The best way to test the validity of these concepts is to build an experimental facility which will test all of these parameters but on a smaller scale. The mid-sized X-2 expansion tube has been designed specifically for this purpose and is currently under construction. It seems pertinent to discuss some design and technology issues of this new facility.

The X-2 will have 10 m of different lengths of shock tubes to be used to validate the active geometry concept. Expected test-times lie in the range 25-45 μs when operating in the super-orbital mode.

Driver Geometry

Following the results of Morgan,[14] it can be shown that the overall driver length can be reduced by a factor of 4 if an area reduction of approximately 9 is used within the two stage driver. This is a sufficient length reduction

for a two-stage driver of 25 metres to be used for future super-orbital work.

For safety reasons, the first stage compression ratio (λ_1) must be chosen so that there is no net separating force during the initial compression stroke. This easily achieved by ensuring that the reservoir pressure behind the piston is always lower than the compressed gas in front of it. A first stage compression ratio of 6 ensures this condition is satisfied and also keeps piston separation pressures to manageable levels. Keeping $\lambda_1 = 6$ also has favourable implications for piston design.

It was fortunate that large pieces of ex-military artillery stock became available which provided a cheap source of high tensile steel. This fixed the second (high pressure) stage of the driver to approximately two metres. Therefore, using basic algebra, the first stage length is set at around 1.1 m. This means an equivalent single bore free-piston driver would be approximately 12.5 metres long.

Piston Design

An important part of the two-stage driver is the compound piston. As discussed previously, to fully exploit the two-stage concept, most of the piston mass needs to be concentrated in the central piston which separates and compresses the driver gas to high pressure.

Due to the high energies and rates of transferral between gas potential and piston kinetic energy it is important for the heavy inner piston not to separate at any point other than the desired location. It would be catastrophic if the conditions were improperly set and the pistons separated before the change-over point. It is therefore necessary to devise a fail safe system where this scenario is impossible.

It is proposed to place brakes on the inner piston as is done in most large scale free piston drivers. This stops piston rebound during final compression. However, in the unlikely situation where the piston brakes completely fail and the primary diaphragm does not burst, the outer piston must be designed to catch and hold the inner piston when it is propelled back to the change-over point.

A sketch of the proposed compound piston is shown in figure 9. There is a small piece of threaded rod which connects the pistons and acts as a tangible link between the two. The ultimate force that the link is designed to withstand is set to the most extreme separating force possible (compression tube overfill). The energy required to break the link is an insignificant fraction (<0.05%) of the overall piston kinetic energy at change over. Thus, the tangible link acts as the fail safe mechanism required to stop catastrophic piston separation.

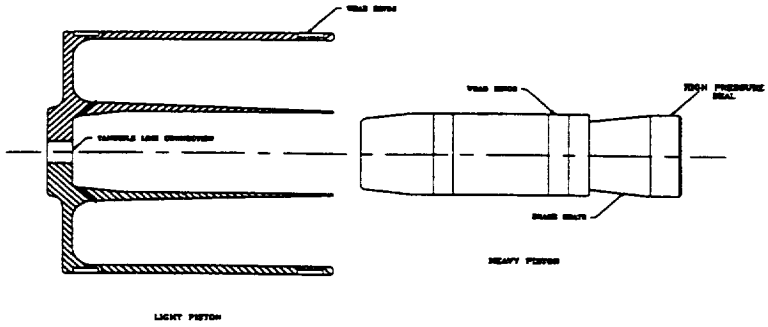


Figure 9. Sketch of Compound Piston.

Attention is also drawn to the rear face of the piston. It is blanked off so the reservoir cannot transfer any more energy beyond the first stage. It is designed this way so the outer piston always has positive pressure locating it against the change over point. This is for the scenario of simultàneous brake failure and a non-bursting diaphragm. If this occurs the

outer piston is ready and waiting for the returning projectile. There are also small matching tapers on the inside and outside of the connecting pistons. It is intended that once the pistons re-connect, most of the energy can be absorbed through a combination of sliding friction and plastic deformation at the tapered surfaces.

The large bore of the first stage compression tube induces high flow rates from the reservoir. A large flow area is therefore required in order to push the combined piston mass. The most efficient reservoir/driver design is to directly connect the reservoir to the driver as shown in figure 10. The piston is launched via a double diaphragm arrangement directly upstream from the reservoir.

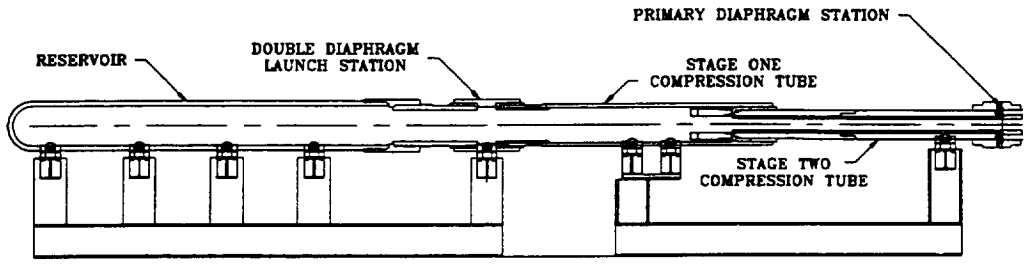


Figure 10. Two-Stage Driver for the X-2.

Conclusions

It can be seen that enhanced performance ground testing equipment is required for research into future super-orbital technology and upper flight Mach number hypersonic propulsion systems. Preliminary calculations for the X-3 facility described in this paper show adequate simulation capabilities for both these flight regimes.

The X-3 will use a new generation free-piston driver utilising two, in-line, compression stages and a compound piston. This new driver concept is designated the two-stage free-piston driver. By removing the area change at the primary diaphragm throat, a large part of the facility cost is reduced. However, efficient wave management is required for a sufficiently long test-time.

The available test-time is seen to have a strong dependence on the interactions of waves, multiple interfaces and boundary layers. In the super-orbital mode of operation (H_0 = 100-180 MJ/kg) test-time is approximately 200 μs. The flow at H_0 = 100 MJ/kg is also seen to be significantly less dissociated than the equivalent enthalpy condition in a shock tube.

Reflected shock tunnels are limited in their total pressure simulations above a flight Mach number of about 12. Operating in the sub-orbital mode, X-3 is shown to adequately simulate both energy and pressure over a

complete scramjet ascent trajectory with a test-time similar to a reflected shock tunnel.

The active geometry concept presented in this paper assumes planar shocks and interfaces along with ideal diaphragm rupture. The two-stage driver performance is also assumed isentropic with no losses. Before a large scale facility can be built, optimisation of driver and expansion tube conditions must be determined with these factors in mind. The mid-sized X-2 has therefore been designed with the specific intent of answering these questions along with developing the technology base for a large scale two-stage free-piston driver.

Acknowledgments

The authors would like to gratefully acknowledge the financial support provided through the Australian Research Council and NASA grant NAGW-674.

References

[1]Lyne, J.E., "Physiologically Constrained Aerocapture for Manned Mars Missions," NASA TM103954, August 1992.

[2]Walberg, G., "How Shall We Go to Mars? A Review of Mission Scenarios," *Journal of Spacecraft and Rockets*, Vol. 30, No. 2, March-April 1993, pp129-139.

[3]Braun, R.D., Powell, R.W. and Lyne J.E., "Earth Aerobraking Stratagies for Manned Return from Mars," *Journal of Spacecraft and Rockets*, Vol. 29, No. 3, May-June 1992, pp297-304.

[4]Mitcheltree, R.A. and Gnoffo, P.A., "Thermochemical Nonequilibrium Issues for Earth Re-Entry of Mars Mission Vehicles," *Journal of Spacecraft and Rockets*, Vol. 28, No. 5, Sept-Oct 1991 pp552-559.

[5]Henline, W.D., "Thermal Protection Analysis of Mars-Earth Return Vehicles," *Journal of Spacecraft and Rockets*, Vol. 29, No. 2, March-April 1992, pp198-207.

[6]Chen, Y.K., Henline, W.D., Stewart, D.A. and Chandler, G.V., "Navier-Stokes Solutions with Surface Catalysis for Martian Atmospheric Entry," *Journal of Spacecraft and Rockets*, Vol. 30, No. 1, Jan-Feb 1993, pp32-42.

[7]Tauber, M.E., Yang, L. and Paterson, J., "Flat Surface Heat-Transfer correlations for Martian Entry," *Journal of Spacecraft and Rockets*, Vol. 30, No. 2, March-April 1993, pp164-304169.

[8]Sharma, P.S. and Park, C., "Operating Characteristics of a 60- and 10-cm Electric Arc-Driven Shock Tube-Part I:The Driver," *Journal of Thermophysics*, Vol. 4, No. 3, July 1990, pp259-265.

[9]Bakos, R., "An Investigation of Test Flow Nonequilibrium Effects on Scramjet Combustion," Phd Thesis, University of Queensland, 1993.

[10]Chinitz, W., Erdos, J.I., Rizkalla, O., Anderson, G.Y. and Bushnell, D., "Facility Opportunities and Associated Stream Chemistry Considerations for Hypersonic Airbreathing Propulsion," *AIAA 17th Ground Testing Conference*, Nashville TN, July 6-8, Paper 92-3991.

[11]Morgan, R.G. and Stalker, R.J., "Double diaphragm Driven Free Piston Expansion Tube," *Proceedings 18th Int. Symp. Shock Tubes and Waves*, Springer-Verlag, 1991

[12]Stalker, R.J. and Morgan, R.G., "The University of Queensland Free-Piston shock Tunnel T4 - Initial Operation and Preliminary Calibration," *Fourth National Space Symposium*, Adelaide, Australia, 1988.

[13]Winders, Barlow and Morrison, Pty., Ltd., "GASL Free-Piston Driven Exansion Tube Performance Predictions," W.B.M.-Stalker Report No., 3732, January, 1989.

[14]Morgan, R.G., "A Compound Isentropic Free Piston Driver for Expansion Tunnels," *Proceedings Eleventh Australian Fluid Mechanics Conference*, Hobart Australia., 1992.

[15]Paull, A. and Stalker, R.J., "Test-Flow Disturbances in an Expansion Tube," *Journal of Fluid Mechanics*, Vol. 245, 1992, pp493-521.

[16]Doolan, C.J., and Morgan, R.G., "Test-Time Optimization of a Large Scale Hypervelocity Expansion Tunnel," *Eighth National Space Symposium*, Brisbane Australia,1993.

[17]Neely, A.J. and Morgan, R.G., "Flow Measurements and Calibration of a Superorbital Exapnsion Tube," *Proc. Eleventh Australian Fluid Mechanics Conference*, Hobart, Australia, 1992.

[18]Rizkalla, O., "EQSTATE: Real Gas Flow Calculator," General Applied Science Laboratories Inc., New York, 1990.

[19]Mirels, H., "Shock Tube Test Time Limitation Due To Turbulaent-Wall Boundary Layer," *AIAA Journal*, Vol. 2, No. 1, Jan. 1964, pp84-93.

[20]White, F.M., "Viscous Fluid Flow", McGraw Hill Inc., New York, 1991, pp531-532.

[21]Paull, A., "Noise Reduction in Argon Driven Expansion Tubes," *19th International Symposium on Shock Waves*, Marseille, 1993.

Design and Construction of the X-2 Two-Stage Free Piston Driven Expansion Tube

Con Doolan

Department of Mechanical Engineering

The University of Queensland

Brisbane, Australia

August, 1995

1 Introduction

This report outlines the design and construction of the X-2 two-stage free piston driven expansion tube. The project has completed its construction phase and the facility has been installed in the new impulsive research laboratory where commissioning is about to take place. The X-2 uses a unique, two-stage driver design which allows a more compact and lower overall cost free piston compressor. The new facility has been constructed in order to examine the performance envelope of the two-stage driver and how well it couples to sub-orbital and super-orbital expansion tubes. Data obtained from these experiments will be used for the design of a much larger facility, X-3 utilizing the same free piston driver concept.

1.1 Two-Stage Driver Concept

When designing the high pressure diaphragm station for free piston shock tubes, it is quickly realised that a substantial portion of the facility cost can be removed by adopting a constant area between the driver and the driven tubes. However, if using a conventional single-bore free piston driver, in order to maintain an adequate supply of driver gas after diaphragm burst the overall facility length becomes impractical. By splitting the driver gas compression process into two parts, a reasonable quantity of driver gas can be supplied with a much reduced compression tube length (approximately a factor of four).

Examining the pressure history that would be expected during any free-piston driver operation cycle (figure 1), it can be seen that most of the compression process occurs with the pressure level remaining below 2% of the final pressure achieved. During this low pressure phase, about 85% of the available reservoir work is converted into piston kinetic energy, the remainder being stored in both the reservoir and driver gases. Therefore, by increasing the bore of the compression tube over the low pressure phase, the volumetric displacement required to accelerate the piston to the required speed can be achieved in a reduced length.

A schematic of the two stage driver concept (first suggested by Morgan[1]) is shown in figure 2. The concept requires a compound piston arrangement consisting of a light aluminium outer and heavy stainless steel inner. At the termination of the large bore first stage, the

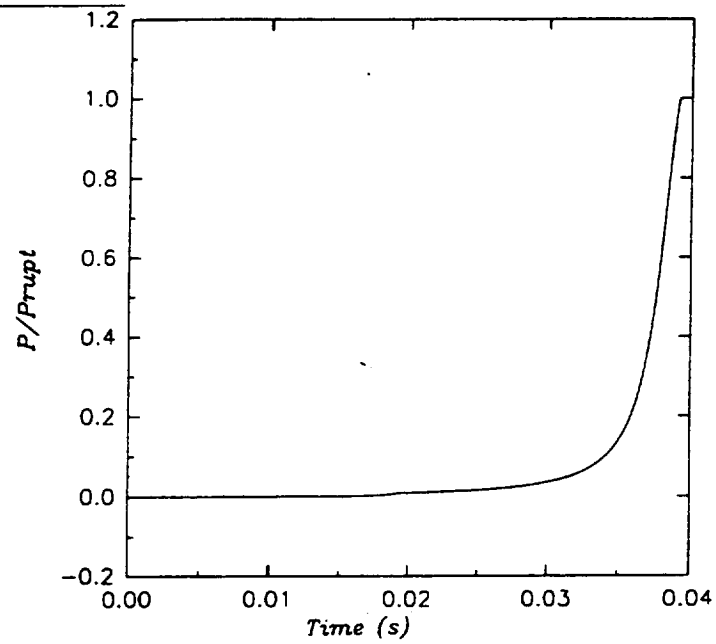


Figure 1: Theoretical pressure history of compression process in a free piston driver

pistons separate. The outer piston is stopped by the use of a buffer and the inner piston (which contains most of the kinetic energy) is allowed to compress the driver gas to high pressure in the small bore second stage.

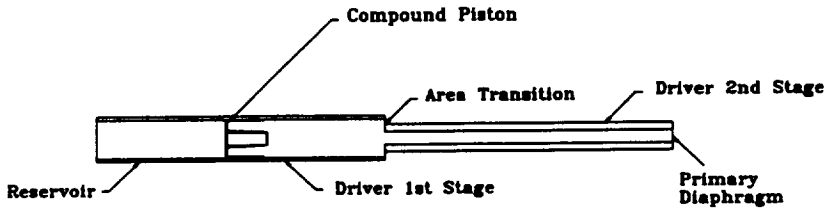


Figure 2: Two Stage Free-Piston Driver Concept

1.2 Basic Theory of Two-Stage Free Piston Drivers

Preliminary operating performance and benefits of two-stage free piston drivers over conventional single stage machines can be seen by considering some elementary gas dynamic theory. Perhaps the two most important criteria for assessing the two-stage driver are size (length) of the final gas slug and its temperature before diaphragm burst. The temperature can be achieved by using a sufficiently high compression ratio, while the final gas slug length

depends upon the geomtery of the facility. The designer must be careful in selecting the geometry of the driver as it influences safety as well as operational issues.

The overall compression ratio (λ) for any free piston device can be written as

$$\lambda = \frac{V_t}{V_f} \tag{1}$$

where V_t is the total driver volume and V_f is the volume of the compressed driver gas just prior to rupture. For two-stage drivers this can be rearranged as,

$$\begin{aligned} \lambda &= \frac{V_1 + V_2}{V_f} \\ \lambda &= \left(\frac{V_1 + V_2}{V_2}\right)\left(\frac{V_2}{V_f}\right) \\ \lambda &= \lambda_1 \lambda_2 \end{aligned} \tag{2}$$

where V_1 and V_2 are the volumes of the driver first and second stages respectively. λ_1 can be considered the first stage compression ratio and λ_2 is the second stage compression ratio.

The first stage compression ratio can be manipulated to yield,

$$\begin{aligned} \lambda_1 &= \frac{V_1}{V_2} + 1 \\ \lambda_1 &= A_R L_R + 1. \end{aligned} \tag{3}$$

A_R and L_R are the area and length ratios between the first and second stages respectively. Using equations 1, 2 and 3 gives the ratio of final compressed driver gas lengths for the two and single stage drivers respectively in terms of driver geometry,

$$\frac{x_T}{x_S} = \frac{A_R \lambda_1}{A_R + \lambda_1 - 1} \tag{4}$$

Leaving equation 4 for the moment, we will consider the pressures across the compound piston during the compression in the first stage. If the pressure ratio of the driver gas to the reservoir gas becomes greater than unity, a potentially dangerous situation exists. The more massive inner piston contains more inertia than the aluminium outer therefore if an acceleration reversal occurs, the pistons may separate prematurely, causing damage to the facility. The geometry and operating conditions can be chosen so as to minimise this risk. By assuming an ideal description of the gas dynamics,

$$PV^\gamma = const. \tag{5}$$

(where P is the gas pressure, V is the volume and γ is the ratio of specific heats) and using the expressions derived above, the following formulae can be described:

$$\frac{P_{df}}{P_{r*}} = \alpha\lambda \left(\frac{\gamma_d - 1}{\gamma_r - 1}\right) \left(\frac{1 - (1 + 1/\alpha + 1/\alpha\lambda_1)^{1-\gamma_r}}{1 - \lambda^{1-\gamma_d}}\right) \tag{6}$$

$$\frac{P_d}{P_r} = \frac{P_{df}}{P_{r*}} (\lambda_1/\lambda)^{\gamma_d} (1 + 1/\alpha - 1/\alpha\lambda_1)^{\gamma_r} \tag{7}$$

Here, $\frac{P_{df}}{P_{r*}}$ is the ratio of final driver pressure to initial reservoir pressure, α is the ratio of volumes between the reservoir and the driver and γ_r and γ_d are the ratio of specific heats for the reservoir and and the driver gas respectively. $\frac{P_d}{P_r}$ is the pressure ratio across the piston after the stage one compression process.

Equations 4, 6 and 7 can be used to provide an estimate of facility performance with respect to a particular chosen geometry (i.e. α, A_R and λ_1). Figure 3 shows the increase in slug length available over single stage machines for various area ratios (A_R) and stage one compression ratios (λ_1). Figure 4 shows the variation of the compound piston pressure ratio (P_d/P_r) with λ_1 and compression ratio (λ). These results illustrate that in order to keep P_d/P_r below unity over a large range of compression ratios, λ_1 must be kept below 6. Also, by limiting the area ratio to 9 (to keep the first stage bore reasonably small) 3.5 to 4 times the slug length of compressed gas generated in a single stage machine can be used if λ_1 is kept between 5 and 6. Alternatively, this ratio can be thought of as the decrease in length a two stage driver offers over conventional drivers for the same amount of driver gas, at the same condtions before diaphragm rupture. For these calculations, α was assumed equal to 2.9.

Although this analysis is simple, it allows a convenient way of sizing the components for X-2 and for showing the benefits of the two-stage free piston driver for a constant area diaphragm station facility.

2 X-2 Facility Construction

This section will outline the major features of the X-2 two-stage expansion tube. The primary aim of the X-2 project is to determine the capability of a two-stage driver with respect to

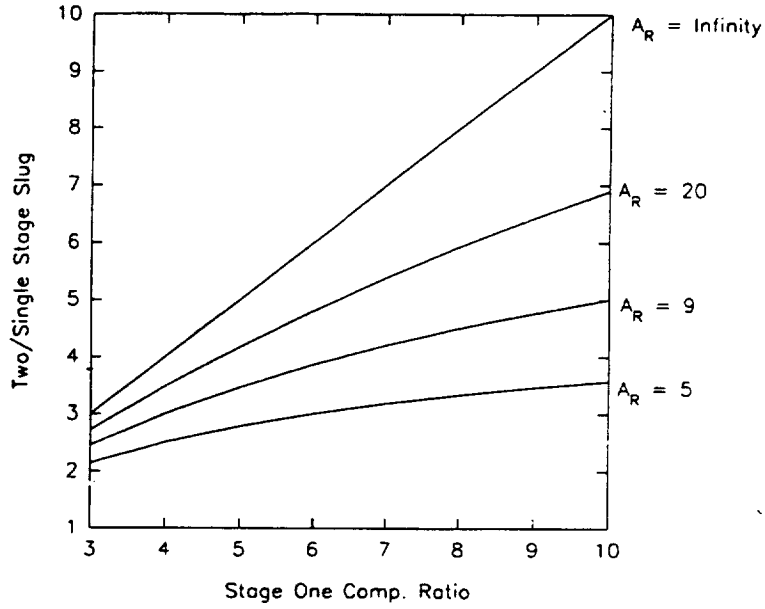


Figure 3: Increase in slug length of two/single stage free piston drivers

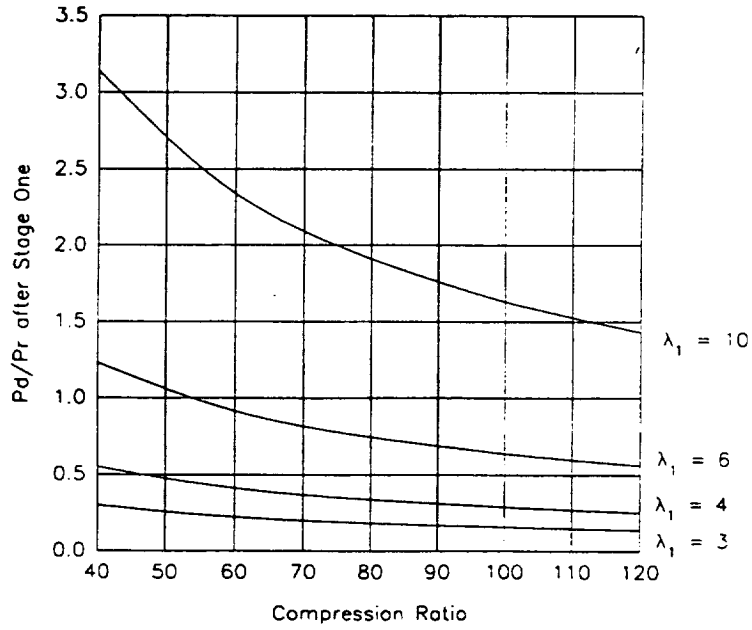


Figure 4: Pressure ratio accross compound piston after stage one

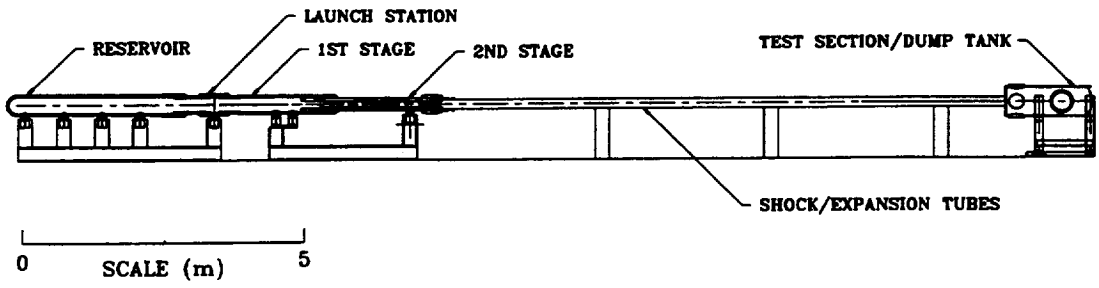


Figure 5: X-2 Facility Layout

the operation of expansion tubes. In order to achieve reasonable test times, the driver must leave an adequate volume of driver behind the diaphragm proir to burst. In a constant area driver, this equates to the distance between the front piston face and the diaphragm. If this distance is too small, unsteady expansion waves reflect off the piston too early and cause premature termination of the test flow.

Figure 5 shows the layout of the X-2 facility. The driver uses a large reservoir to accelerate the piston. The reservoir volume is 0.23 m^3 and is approximately three times the volume of the driver itself. The reservoir is shown in figure 6.

The compound piston is required to be accelerated to a high speed (50-100 m/s) within the first stage (1.1 metres of compression allowed) and because the first stage has a large bore (273 millimetres), a piston launch mechanism is required which provides little flow resistance to the reservoir gas. For this reason a double diaphragm arrangement is used to launch the piston. The launch station is shown in figure 7. The operating principle is relatively simple and well known: the space created between the two diaphragms is filled to half the diaphragm burst pressure. The reservoir is now filled to the full burst presssure. Piston launch is initiated by the venting of the space between the diaphragm to atmosphere, resulting in diaphragm burst.

The first stage compresson tube provides the bulk of the compression process, which is done at low pressure (up to 2 MPa). The outer piston is stopped at the end of the first stage by the use of a large rubber buffer (fig. 8), bonded to a mounting plate attached to the end wall of the second stage. The size of the buffer depends on the amount of energy required to be shed from the outer piston at impact. The current buffer has been designed to

withstand a 25 KJ impact which equates to a 6 kg piston travelling at 90 m/s. The size of the buffer also affects the first stage compression ratio (λ_1). As mentioned previously, the overall performance is sensitive to this ratio and must be kept large enough for an adequate volume of compressed driver gas. The current buffer allows $\lambda_1 = 5.24$. The first stage compression tube is shown in figure 9.

After the pistons separate, the inner piston travels down the second stage compression tube, where it compresses the driver gas to its final conditions and brings itself to rest before diaphragm burst. The second stage is of a multi-wall design, with an 18 mm thick sleeve interference fitted via liquid nitrogen cooling along the bore. The inner bore is 91 mm and the outer diameter is 225 mm. In order to compensate for any misallignment of the first and second stages, a tapered teflon conical entrance is provided for the second stage, allowing the inner piston some protection as it traverses the area transition. Figure 10 shows the second stage compression tube.

A sectioned view of the primary diaphragm station in shown in figure 11. The station can accomodate up to a 5 mm stainless steel diaphragm and is designed to withstand a 100 MPa impulsive load. The diaphragm is held in place with the use of a free-piston clamp. This clamp transmits an initial pre-load to the diaphragm from the tourque developed by tightening the capstan nut. As the pressure increases in front of the piston during operation, a small space allows this pressure to work on a large area of the free-piston clamp, making the axial load on the diaphragm directly proportional to the burst pressure. This ensures a large clamping load on the diaphragm and minimises the risk of slippage during operation.

The two-stage driver will be used to generate flow in 10 metres of shock tubes with an eightyfive millimetre nominal bore. These tubes are machined into seven lengths varying in length from 2.5 metres to 500 millimetres. This array of shock tubes allows study into the interactions of waves, boundary layers and multiple interfaces and their cumulative effect on expansion tube test-time. These tubes are constructed from the barrel of an ex-World War Two 17 pound anti-tank gun. Figure 12 displays the shock tubes installed in the laboratory.

The test section/dump tank has been constructed from the reservoir of an ex-submarine torpedo launcher (figure 13). It has dimensions of 500 mm bore and is 1500 mm long.

In order to achieve the very low pressures required for super-orbital testing (fill pressures approximately 1 Pa), a 13 inch Edwards oil diffusion pump has been fitted to a large flange welded to the dump tunk wall. Four access ports 90 degrees apart are provided at the test section end for instrumentation and optical access.

3 Compound Piston

The compound piston consists of an aluminium outer piston ($\sim$ 5kg) and an AISI 316 stainless steel inner piston ($\sim$ 14 kg). A sketch of the compound piston design is shown in figure 14. The light outer piston uses carbon/graphite filled teflon wear rings as bearing surfaces. A tangible link connection exists at the rear. This is used as a safety device to prevent premature separation of the pistons in the first stage. The tangible link is basically a disposable shaft of steel rated to withstand the maximum reversing force which can be calculated for a given fill pressure using the theory discussed previously. This unsafe condition may occur if the piston is accidentally pre-launched during reservoir fill, or the conditions are improperly set. The reversing force is an order of magnitude below that experienced during normal separation at the area transition so the tangible link has negligible effect on the piston dynamics.

The heavy inner piston also uses filled teflon wear rings. It uses a high pressure chevron seal similar in design to the T4 and T5 pistons. Also shown are provision for piston brakes. It is important that the inner piston is held in position after final conditions are achieved. If brakes were not fitted, and the diaphragm failed to open (or running in blanked off mode), the piston would return to the outer piston with the velocity it left (50-100 m/s). This would cause regular destruction of the outer piston (or worse). In the unlikely eventuality that the brakes did fail, the outer and inner pistons have been designed with matching tapered surfaces at their rear. The energy of impact could be then disspated through a combination of sliding friction and plastic deformation at this tapered interface.

4 Preliminary Commissioning Results and Future Work

The commissioning of the X-2 facility entails a study of the performance envelope of the free piston driver and how well it couples to an expansion tube. Driver studies have commenced with experiments involving a special 17.5 kg steel outer piston only. These tests have qualified the energy absorbing capacity of the rubber buffer located at the end of the first stage. A quasi-one-dimensional Lagrangian code[6] has been used to simulate the operating cycle of X-2. The transient performance of the rubber buffer has been modelled using a simple stress wave/lumped piston mass model. This model assumes the stress in the rubber is proportional to the velocity of the piston, which is in turn decelerated by that stress acting over a small time step.

Figure 15 compares the experimental pressure trace at the 'blanked off' diaphragm station to the quasi-one-dimensional numerical simulation. Agreement is good with both traces showing similar pressure rises and peak pressures matching to within 6%.

There was some uncertainty regarding the impact performance of the rubber buffer prior to the commencement of tests. The rubber has shown to be an excellent impact medium showing no signs of damage. The buffer has been impacted with a maximum energy of 11.5 kJ and it is planned to take it to the full 25 kJ required for 100 MPa diaphragm burst.

Also, different driver gases will be used to study the flow effects of heavier gases (such as argon) through the area transition and their influence on piston dynamics and final conditions.

Tests involving dual pistons driving a shock tube will begin soon, followed by expansion tube tests. An estimate of expected conditions to be achieved in X-2 as an expansion tube are presented in table 1. These results were calculated using an analytical wave tracking code including equilibrium chemistry for air[2] and Mirels[3] boundary layer theory to correct the interface trajectories. Case one and two use the conventional expansion tube configuration of shock and acceleration tube. Case three uses another shock tube immeadiately before the shock tube known as the secondary driver tube, as described by Morgan and Stalker[4]. This arrangement allows the generation of suber-orbital flow, as explored experimentally by Neely and Morgan[5].

Table 1: Calculated X-2 Conditions

Case	Test Gas	Primary Shock Speed (m/s)	Secondary Shock Speed (m/s)	Total Enthalpy (MJ/kg)	P_7/P_4^* (10^{-6})	Test Time (μs)
1	He	4111	6914	27	250	90
2	Air	2800	5500	13.5	500	100
3	Air	12000	16000	180	850	35

*P_7 is the test section static pressure and P_4 is the driver pressure prior to burst.

It is hoped that the knowledge gained from these experiments will allow the design and construction of a much larger expansion tube using the two-stage driver concept.

5 Acknowledgments

The author gratefully acknowledge the financial support given by NASA grant NAGW-674 and the Australian Research Council. The military hardware was most generously supplied by the Australian Defence Science and Technology Organisation and Sydney University, Australia.

6 References

[1]Morgan, R.G., "A compund isentropic free-piston driver for expansion tunnels," *Proc. 11th Australian Fluid Mechanics Conference,* Hobart Australia, 1992.

[2]Rizkalla, O., "EQSTATE: Real Gas Flow calculator," General Applied Science Laboratories Inc., New York, 1990.

[3]Mirels, H., "Shock Tube Test Time Limitation Due to Turbulent-Wall Boundary Layer," *AIAA Journal,* Vol. 2, No. 1, 1964, pp. 84-93.

[4]Morgan, R.G. and Stalker, R.J., "Double diaphragm driven free piston expansion tube," *Proc. 18th Int. Symp. Shock Tubes and Waves,* Springer-Verlag, 1991.

[5]Neely, A.J. and Morgan, R.G., "The Superorbital Expansion Tube Concept, Experiment and Analysis," *The Aeronautical Journal,* March, 1994, pp.97-105.

[6]Jacobs P.A. "Quasi-one-dimensional modeling of a free-piston shock tunnel," *AIAA Journal*, Vol 32, No. 1, 1994, pp.137-145.



Figure 6: Photograph showing X-2 reservoir installed in Laboratory

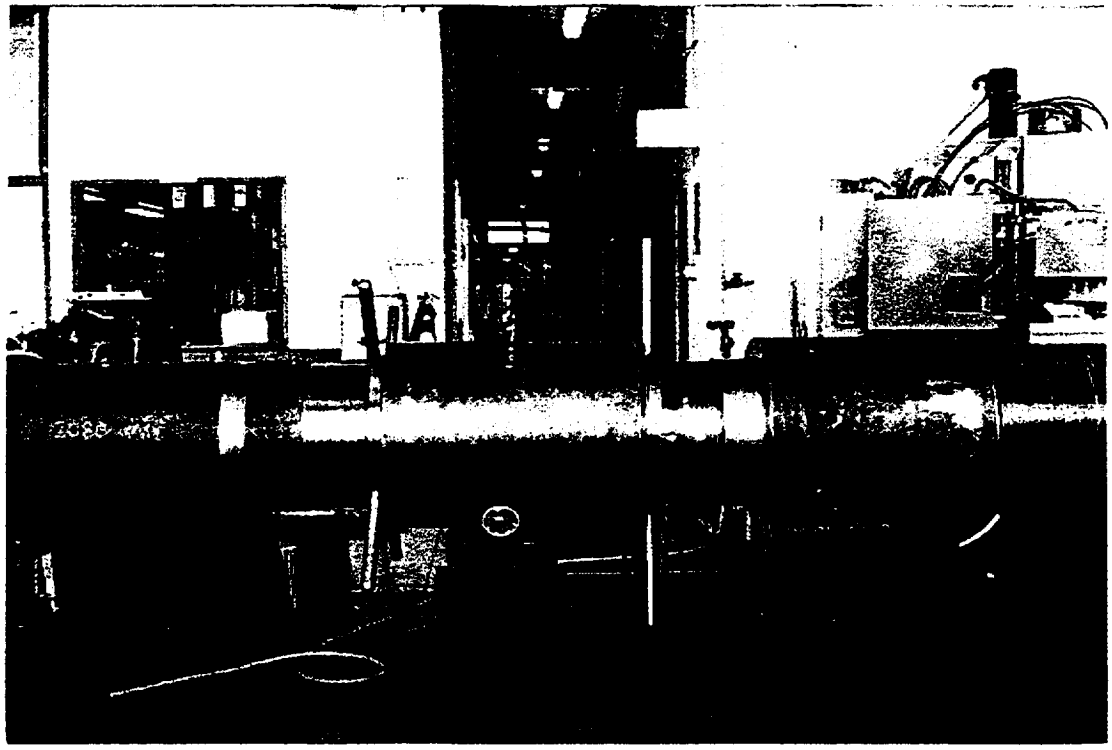


Figure 7: Photograph of double diaphragm launch station



Figure 8: Photgraph of the buffer used to stop the outer piston



Figure 9: Stage one compression tube

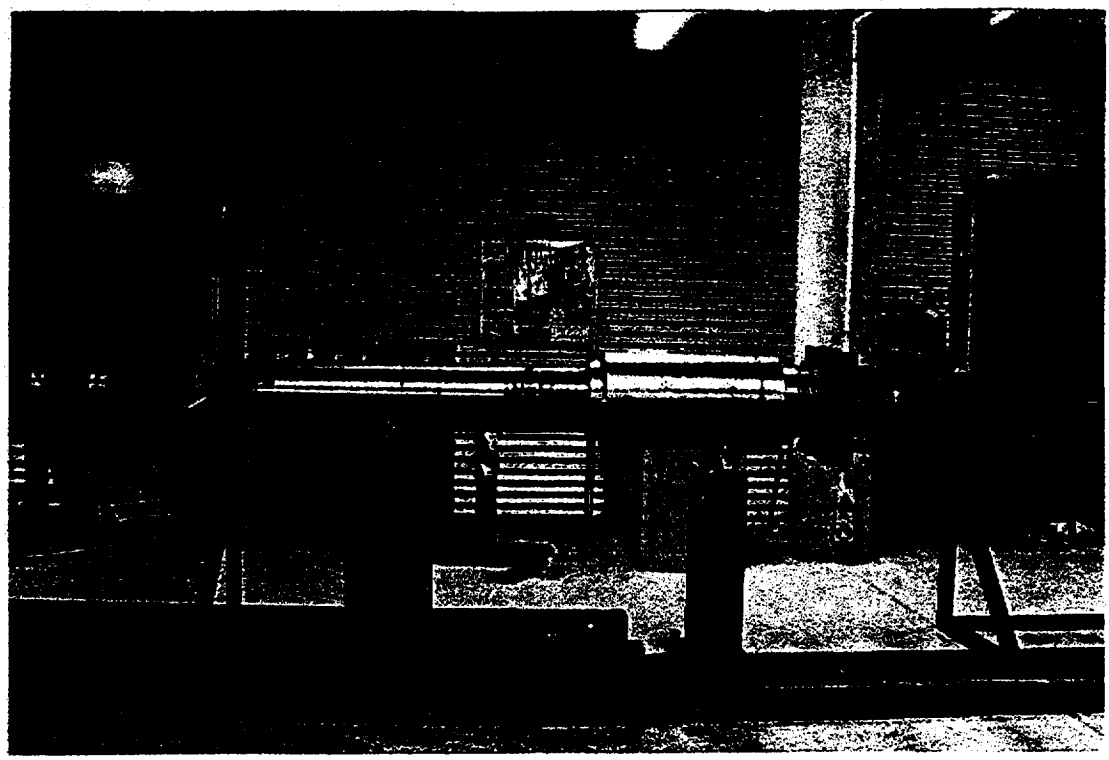


Figure 10: Stage two compression tube

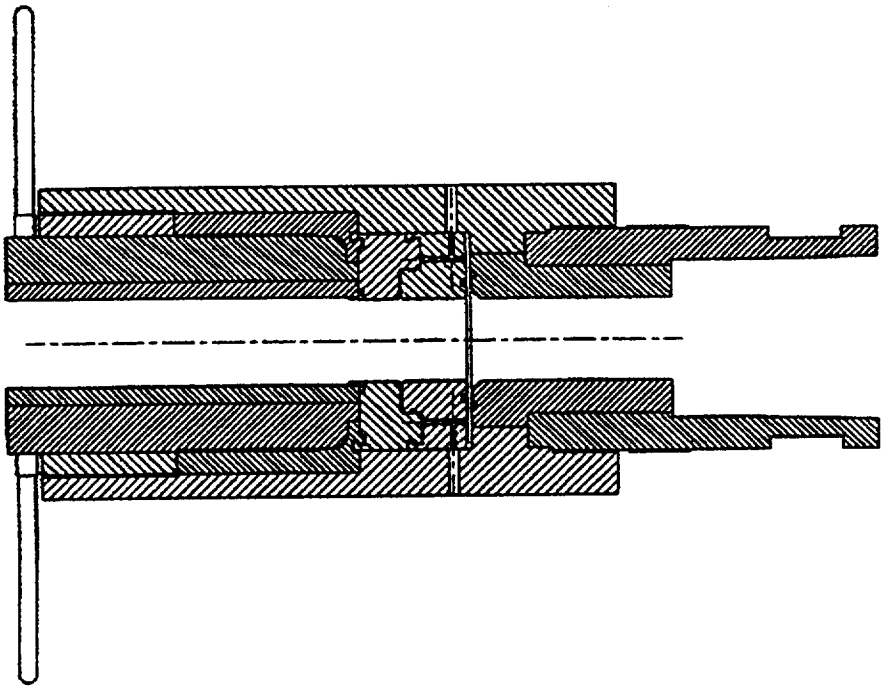


Figure 11: Sectioned view of primary diaphragm station



Figure 12: X-2 shock tubes installed in laboratory

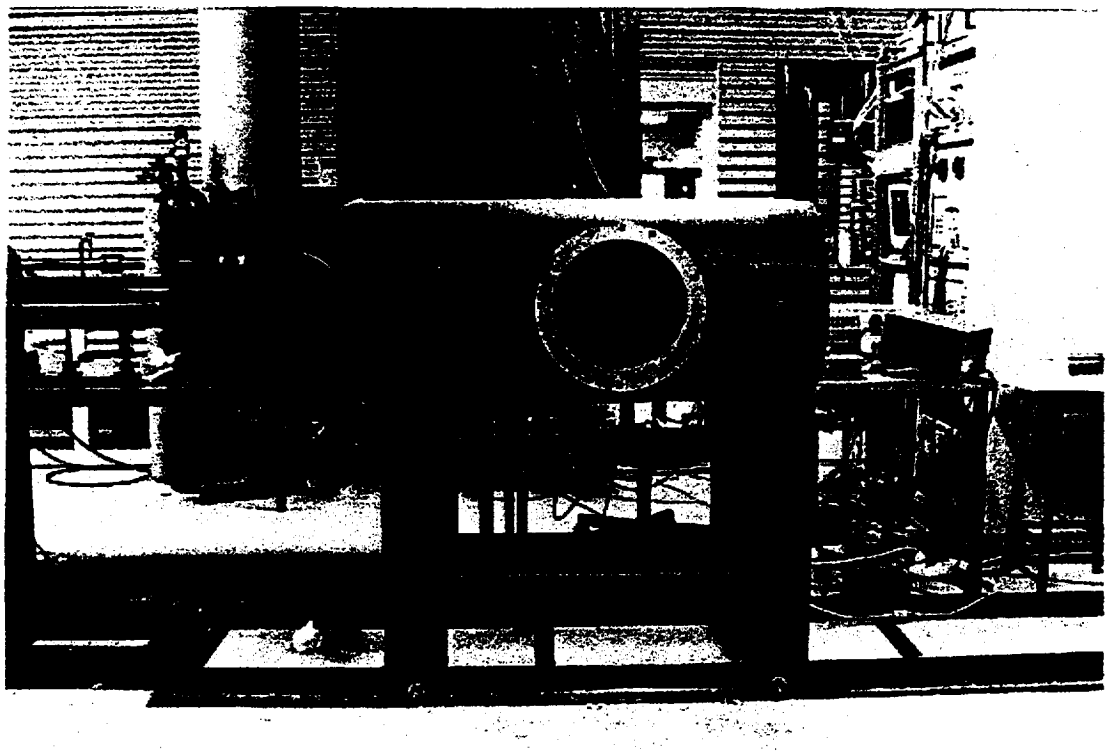


Figure 13: X-2 test section/dump tank installed in laboratory

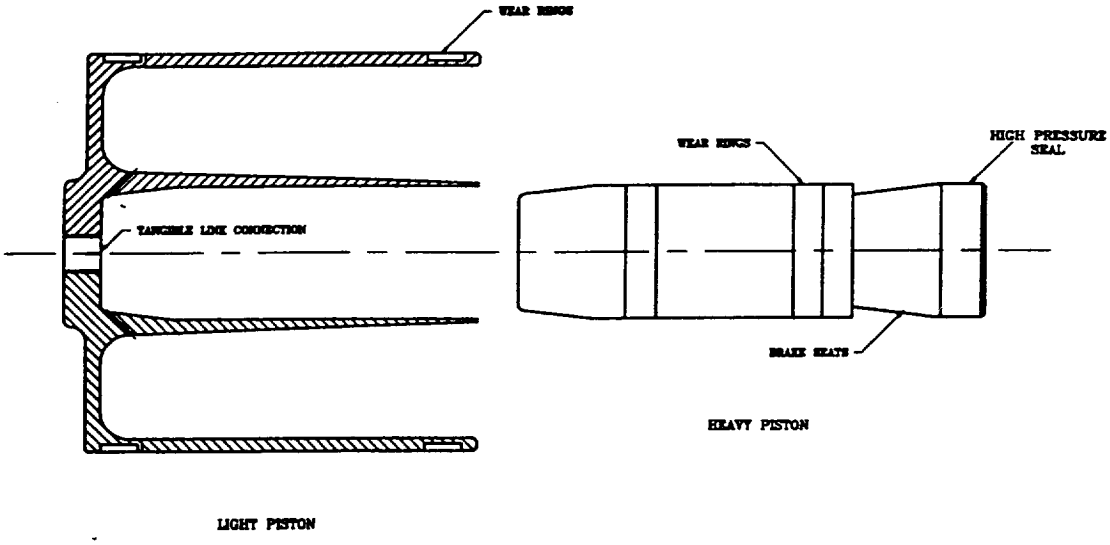


Figure 14: Sketch of X-2 Compound Piston

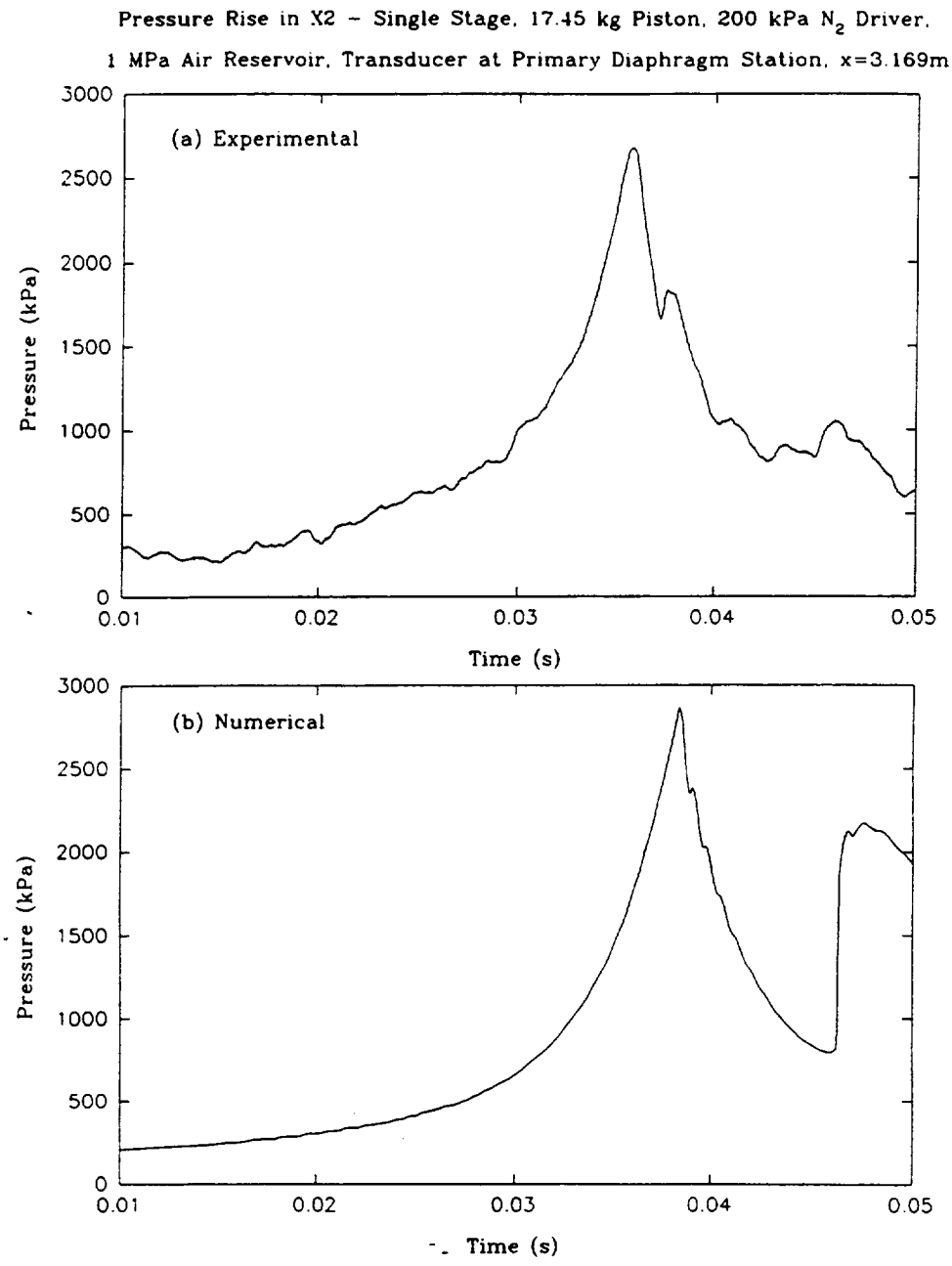


Figure 15: Comparison between experiment and numerical simulation

Boundary Layer Blockage in Expansion Tube Nozzles

O.Sudnitsin and R.G. Morgan
University of Queensland
Brisbane, QLD, 4072, AUSTRALIA

Abstract: The results of a first order perfect gas correction for the effects of the boundary layer formation within expansion tubes with nozzles are presented. The analytical model developed to describe the boundary layer formation within the expansion tube and an expansion nozzle located at the end of the acceleration tube is based on the Kármán integral equations. The results of this analytical model are compared with experimental data from an expansion diffuser. The model provides a useful tool for the preliminary design of nozzles for such facilities.

Key words: Boundary layer formation, Boundary layer blockage, Nozzle flow, Expansion tubes, Hypersonic flows, Kármán integral equations

1. Introduction

Scale modelling of hypersonic flows cannot be achieved with complete matching of all non-dimensional scaling parameters. Laboratory testing generally involves only partial similarity and can be justified if the phenomenon of interest is controlled primarily by matchable parameters. For example, the binary scaling parameter allows accurate modelling of binary finite rate dissociation processes, simultaneously reproducing viscous effects.

However, many processes of interest in hypersonic flow do not follow binary scaling, and exact simulation requires full size models. Combustion, recombination and gas radiation are examples of such processes. The size of the test section, therefore, limits the size of flight vehicle which can be tested in this way. Expansion of laboratory test flows enables larger models to be tested, but the associated drop in pressure limits the range of flight conditions which can be reproduced. Because of their high total pressure simulation capability, expansion tubes can potentially provide improved performance over other existing facilities.

In the superorbital expansion tube it is of interest to model rarefied flow phenomena, for which it will be necessary to reduce gas density by means of a nozzle.

The limited test size of an expansion tube may be increased by means of an expansion nozzle located at an appropriate section of the tube (Sudnitsin & Morgan 1994). The starting process associated with nozzle flows reduces the steady test time available (Leyva 1994), and may provide additional limitation on model size.

A nozzle was tested successfully by Miller & Jones 1983 on an expansion tube. However, for their purpose, the unmodified expansion tube was found to be better and the use of the nozzle was discontinued.
Despite the reduction of the binary scaling parameter associated with the use of nozzles, direct simulation over a useful range of flight conditions may still be obtained.

However, certain problems need to be addressed if such nozzles are to be used. Firstly, reservoir pressure must be sufficient to reproduce real flight conditions. A simple ideal gas analysis (Sudnitsin & Morgan 1994) provides a quick assessment of operational conditions in terms of the important non-dimensional parameters. Using this approach, the characteristics of simulated flow in terms of total pressure, driver noise attenuation (Paull & Stalker 1992) and test gas temperature may be found for three different configurations of an expansion tube with the divergent nozzle placed at A - the end of the driver section, B - the end of the shock tube and C - the end of the acceleration tube. Configurations and conditions which may give superior performance and for which further investigation is justified can thus be easily identified.

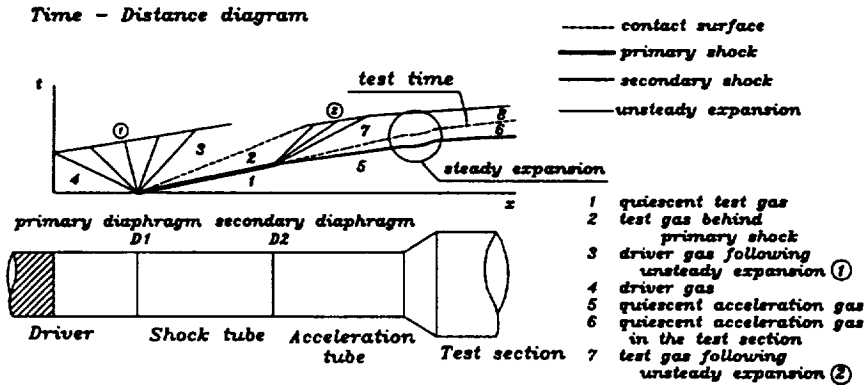


Figure 1. Configuration C

According to the results of the performance comparison in terms of nose-to-tail pressure ratio , configuration C has been chosen for initial investigation (Fig. 1). This configuration is advantageous because it is relatively sim-

ple to modify the existing facility and it can be shown that its performance at some operating conditions is comparable to the configurations A and B (Sudnitsin & Morgan 1994).

One aspect of nozzle design concerns the influence of the boundary layers on the effective test flow area achieved in the core flow. This effect is small for low Mach number flows, and is often not corrected for in the design stage, because direct calibration under operating conditions can be used to determine precisely the expanded flow parameters. However, in superorbital expansion flows significant boundary layer blockage may arise, and the nozzle geometric area ratio may be quite different to that seen by the core flow. Consequently, an analysis is presented which couples the boundary layer displacement thickness to the expansion process, giving an improved indication of the state of the core flow.

The present analysis has been done for a small-scale expansion tube at the University of Queensland (X1), and the nozzle is currently under construction.

Experimental data for a diffuser on an expansion tube obtained by General Applied Science Laboratories, Inc (GASL) (Bakos et al. 1992, Bakos 1994) were used to validate the analytical results prior to designing the nozzle for X1 at the University of Queensland.

2. Boundary layer analysis

The present analysis investigates the growth of the boundary layer on the walls of the expansion tube which will reduce the size of the available test core from A_1 to A_1^* (Fig. 3) and change the area ratio of the nozzle, resulting in a decrease in the pressure ratio associated with it.

Flow is assumed to be compressible, and the formation process has been

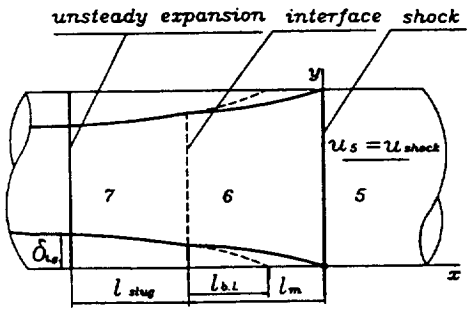


Figure 2. Boundary layer formation in the acceleration tube

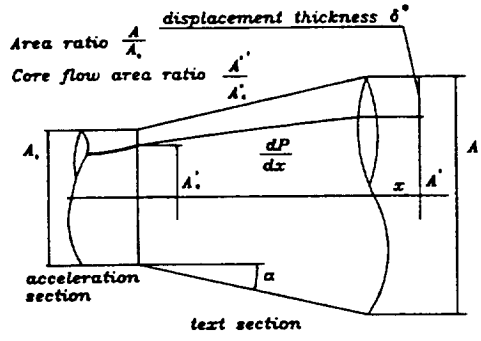


Figure 3. Boundary layer formation in the nozzle

divided into two stages, formation within the tube and growth within the di-

vergent nozzle.

2.1. Boundary layer formation within the acceleration tube

A boundary layer grows between the head of the rarefaction wave and the shock. Fig. 2 schematically demonstrates the different stages of the boundary layer formation and flow for each region.

Boundary layers within the shock tube act as an aerodynamic sink for acceleration gas in region 6 between the shock and interface (Fig. 2). Test gas is also lost by this process in region 7, behind the interface.
The boundary layer at the exit plane of the acceleration tube grows with time. The worst boundary layer thickness occurs with the arrival of the secondary unsteady expansion head (Fig. 2). At this point useful gas flow, in this region is completed.

For the present calculations a worst case approach was adopted, assuming the origin of the test gas boundary layer coincided with the shock location. Therefore, region 6 (Fig. 3) is considered infinitively small and $l_{b.l.} = l_m$, which is a good approximation at high shock speeds. Thus, the test gas boundary layer develops under the influence of conditions behind the interface (region 7 in Fig. 3).

Table 1. Sample predicted condition for X1, targeting supersonic combustion

Regions Fig. 1	Pressure,Pa	Temperature,K	Velocity, m/sec	Speed of sound ,m/sec
4	5E+07	2000	0	1827[a]
7	6E+5	3082	3727	1112[b]
8	25E+3	1250	4200	709

Primary shock speed $U_{sh1} = 3000 m/sec$, secondary shock speed $U_{sh2} = 4500 m/sec$
Speed of sound ratio across the driver gas-test gas interface $\frac{a_3}{a_2} = 0.7$
[a] driver gas is a mixture of He and Ar with $\gamma = 1.67$ and $\mathcal{R} = 1000\, J/(kg\, K)$
[b] test and acceleration gas is air with $\gamma = 1.4$ and $\mathcal{R} = 287\, J/(kg\, K)$

In the sample calculation for X1 (Table 1), it was assumed that the boundary layer behind the interface in the acceleration tube is turbulent. The characteristic thicknesses δ – boundary layer thickness, δ^* – displacement thickness, θ – momentum thickness defining integral deficits were calculated from Hayes & Probstein 1959 and act as starting conditions for the nozzle boundary layer calculation.

2.2. Boundary layer formation within the expansion nozzle

The modelling of the nozzle boundary layer assumed the surface can be represented by a flat plate with a favourable pressure gradient, the flow is compressible, and that the Kármán-Based Method of Walz (1969) may be used to quantify the development of δ^* and θ with x.

The approach used allows the bulk boundary layer properties to be calculated without solving for the internal profiles. These properties can then be used in a one-dimensional approach to calculate nozzle exit conditions.

The physical information required to complete the calculations was incorporated into the differential equation for the velocity, density and area ratio variations along the nozzle. After the initial values of the variable parameters (Walz 1969) were estimated, final bulk properties of the boundary layer were obtained by solving the system of differential equations. A conical nozzle with an area ratio of 9 was used to generate the axial pressure distribution used for the computations. When the effect of the boundary layer displacement thickness was added to the contour, the geometric area ratio needed to expand the core flow to the correct pressure was found to be 20. This illustrates the importance of boundary layer blockage for these flow conditions. The increase of displacement thickness is due to the entrainment of new fluid in the nozzle, and also to the expansion of the boundary layer gas. In this example 66% of the downstream displacement thickness is due to entrainment in the nozzle, illustrating the importance of minimising nozzle length. The experimental validation of this result is yet to be made.

3. Comparison with experimental data

In order to validate the analysis above, it was applied to data from a diffuser placed at the end of the expansion tube at GASL (Bakos et al. 1992). The 0.85 m long diffuser with the initial conditions M17 (Bakos 1994) produced boundary layer with a thickness $\delta_{exit} \approx 6.25\,mm$ (from an exit Mach number profile Bakos et al. 1992). The nozzle starting condition, M17, and the history of the boundary layer were deduced from Bakos et al. 1992 where the boundary layer thickness was measured to be $\delta_0 \approx 25\,mm$ at the acceleration tube exit.

The diffuser was designed to produce a pressure increase of 11.9 (perfect gas approximation) in static pressure relative to the incoming flow. After correction of the contour to account for the displacement thickness, the pressure increase expected is 8. The actual experimental pressure ratio (Table.2) (Bakos et al. 1992) was measured to be 8.8. Therefore it can be seen that the inviscid calculation of a diffuser contour somewhat overestimates pressure ratio, whereas the boundary layer corrected contour can predict the pressure ratio

much more realistically. The fact that the viscously corrected and experimental pressure ratios are not exactly the same may be partly due to the fact that the boundary layer thickness was not precisely known from the data available. Further validation will be provided by the planned experiments.

4. Conclusions

The present work indicates the importance of viscous effects in expansion tubes with nozzles. It demonstrates the significant effect of the displacement thickness correction on the contour and the predicted pressure ratio. As the velocities and Mach numbers of the phenomena of interest increase, it will be important to correct for viscous effects right from the earlier stages of nozzle design, rather than calibrating for viscous effects after construction. The simple correction technique is provided to assist with this type of problem.

Acknowledgement. This work was partially supported by the NASA Langley Research Center (Grant NAGW 674, contract monitor R.C. Rogers).

References

Bakos R(1994) An Investigation of Test Flow Nonequilibruim Effects on Scramjet combustion Ph.D. thesis, University of Queensland

Bakos RJ, Tamago J, Rizkalla O, Pulsonetti MV, Chinitz W, Erdos JI(1992) Hypersonic Mixing and Combustion studies in the Hypulse Facility J. Propulsion and Power 8:900-906

Hayes WD and Probstein RF (1959) Hypersonic Flow Theory Academic Press, New York

Leyva IA (1994) Study of the addition of a divergent nozzle to an expansion tube for increasing test time. Paper No. AIAA 94-2533 In: 18th AIAA Aerospace Ground Testing Conference, Colorado Springs, CO

Miller CG and Jones JJ (1983) Development and Performance of the NASA Langley Research Center Expansion Tube/Tunnel, A Hypersonic-Hypervelocity Real-gas Facility. AIAA 14th International Symposium on Shock Tubes and Waves, Sydney Australia,

Paull A and Stalker R (1992) Test flow disturbances in an expansion tube. J. Fluid Mech. 245:493-521

Sudnitsin O and Morgan RG (1994) Expansion tube area change optimisation. In: at 4th International Workshop on Shock Tube Technology, Brisbane, Australia

Walz A(1969) Boundary Layers of Flow and Temperature The M.I.T. Press

AIAA 94-2596

Lift, Drag and Thrust Measurement in a Hypersonic Impulse Facility

S. L. Tuttle, D. J. Mee and J. M. Simmons
Department of Mechanical Engineering
The University of Queensland
Brisbane, Australia

18th AIAA Aerospace Ground Testing Conference
June 20-23, 1994
Colorado Springs, Colorado

LIFT, DRAG AND THRUST MEASUREMENT IN A HYPERSONIC IMPULSE FACILITY

S.L. Tuttle *, D.J. Mee ** and J.M. Simmons ***

The University of Queensland, Australia

Abstract

This paper reports the extension of the stress wave force balance to the measurement of forces on models which are non-axisymmetric or which have non-axisymmetric load distributions. Recent results are presented which demonstrate the performance of the stress wave force balance for drag measurement, for three-component force measurement and preliminary results for thrust measurement on a two-dimensional scramjet nozzle. In all cases, the balances respond within a few hundred microseconds.

1. Introduction

A new technique has been developed at The University of Queensland for measuring the transient forces experienced by models in the hypersonic flows of the T4 free piston driver shock tunnel. In this facility, where test flow durations of 1 millisecond are typical, there is usually insufficient time for the model to reach a state of force equilibrium with its supports. However, by interpretation of the stress waves which travel through the supports, the aerodynamic loading may be determined. This is achieved by studying the dynamic behaviour of the model on its support using finite element analysis and dynamic calibration. In this paper the capabilities of the stress wave force balance for measurement of drag on an axisymmetric body are first demonstrated using recent measurements on a long (425 mm) 5° semi-vertex angle cone at zero incidence. Results are then presented from tests in which a 15° cone was placed at incidence, producing non-axisymmetric forces on the model. Three components of force were measured. Finally, preliminary results are presented for measurements of the thrust produced on an 11° scramjet thrust nozzle of rectangular cross-section.

2. The Force Measurement Technique

The measurement of forces on vehicles flying at hypervelocity conditions has been restricted by the short durations for which current experimental facilities can sustain a representative flow. Progress has recently been made in designing balances for use in flows of duration as short as a few milliseconds[1,2,3].

Conventional force balances require sufficient test time for the forces on the model and its supports to reach equilibrium. Acceleration compensation has enabled the measurement of forces in test times as short as 10 milliseconds. For the 1 millisecond test flows of hypervelocity impulse devices such as T4, the flexibility of the model becomes significant and these methods do not work. The use of discrete pressure tappings for inferring forces is limited to simple model geometries and does not take account of skin friction.

The configuration of the stress wave force balance is shown in Figure 1. The model is mounted on a long support, or sting, and the two are suspended freely from the test section roof by fine wires. The model is aligned with the flow direction.

The impact of the flow on the model causes stress waves to travel through the model and on into its support. Tension and compression stress waves travel at the speed of sound of the material. An important feature of this force measurement technique is that the sting is made long enough to allow sufficient time for the rise of the stress in the sting to be measured before the reflection of the initial waves returns from the far end of the sting. To this end, strain gauges are mounted on the sting a short distance behind the model.

In the case of drag measurement, the impact of the flow on the model causes compression waves to travel through the model. Upon arrival at the interface with the sting, some of these waves will reflect from this boundary and some will be transmitted into the sting. The stresses continue to reflect within the model while the waves

* Graduate student, Department of Mechanical Engineering

** Lecturer, Department of Mechanical Engineering

*** Dean of Engineering, MAIAA

Copyright © by the American Institute of Aeronautics and Astronautics, Inc. All rights reserved.

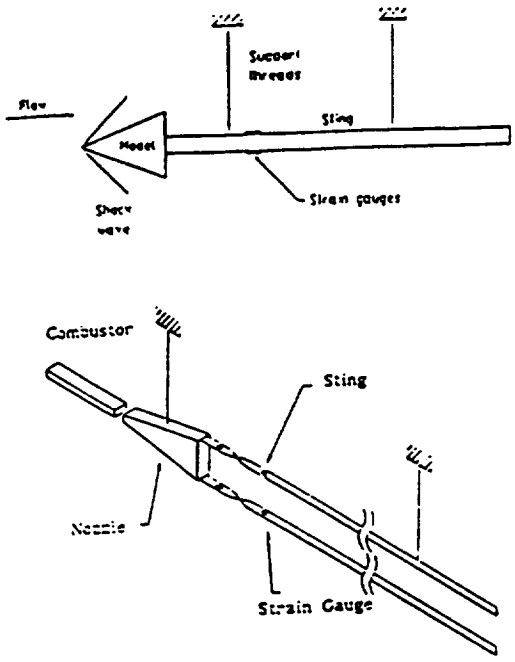


Fig. 1 Stress wave balance configuration for a cone model and a scramjet thrust nozzle.

propagating down the sting will reflect from the free end as tension waves. Materials are chosen so that the stress waves pass through the model as quickly as possible, and are then slowed down in the sting to maximise observation time. Aluminium (stress wave speed = 5000 m/s) is used for the model and brass for the sting (stress wave speed = 3500 m/s). The sting is 2 metres long and so there are approximately 1.1 milliseconds before the reflected stress waves returns.

The joint between the model and sting is important. The impedance of this should be minimised. This entails maximising the contact area between the two and minimising the mass of the model, while still ensuring that the level of strain in the sting is measurable.

The rise of the stress at the strain gauge position due to a step loading on the model may be approximated as exponential[4] with the following time constant, τ

$$\frac{m}{\rho c A}$$

where m is the mass of the model, ρ is the density of the sting material, c is the speed of sound in the sting material and A is the contact area between the model and sting. It is desirable to keep the time constant as small as possible, so the contact area needs to be as large as possible and the model should not be excessively heavy. However, the balance does allow the testing of models of a useful size.

Generally, the level of stress in the sting does not reach the static or steady state level that would be reached if the tunnel loading lasted longer. In order to determine what the actual aerodynamic load was that caused the response measured in the sting, a knowledge of the impulse response of the model is required. This is obtained experimentally by dynamic calibration and is then compared with a finite element prediction. The dynamic calibration involves suspending the model and sting vertically. Weights are hung from the model by a thin wire. Cutting the wire provides a step change in the load on the model.

It is possible to obtain an impulse response which includes the reflections of the stress waves off the model and the ends of the stings. By cutting a support wire and allowing the model and sting to fall freely under their own weight, a free-end condition is achieved for the stings. This allows the deconvolution of the aerodynamic loading over longer times (even though the useable test flow in the tunnel usually finishes at approximately the same time that the first stress wave reflection returns).

The MSC/NASTRAN package is used to compute the response of the model to a step pressure load. The impulse response is then the derivative of the step response. It has been shown that both the 5° semi-vertex angle cone and the thrust nozzle are reasonably insensitive to loading distribution, by comparing the extremes of a point load applied at one end of the model, and a uniformly distributed pressure loading applied to the appropriate model surfaces.

The model on its sting is a linear dynamic system which may be described by the following convolution integral:

$$y(t) = \int_0^t g(t-\tau)\, u(\tau) d\tau$$

where y(t) is the strain measured in the sting, u(t) is the input drag or thrust, and g(t) is the unit impulse response of the system. Once g(t) is known for the system, the unknown loading on the model may be found by deconvolution. An iterative time domain deconvolution algorithm of Prost and Goutte[5] is used.

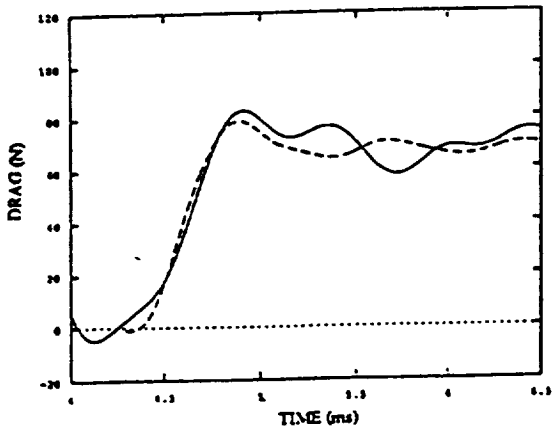
The stress wave force balance was initially demonstrated by Sanderson and Simmons[6] using a 200 mm long 15° semi-vertex angle cone. The 425 mm long 5° cone represents a more demanding test of the technique. The greater length means that stress wave reflections within the model occur over a longer time and the geometry of the cone means that the total drag forces being measured are smaller. Both skin friction and base pressure

become important factors. Early results from this model have been shown by Sanderson et al.[4] More recent results demonstrating the performance of the balance for an axisymmetric loading on an axisymmetric model are shown next.

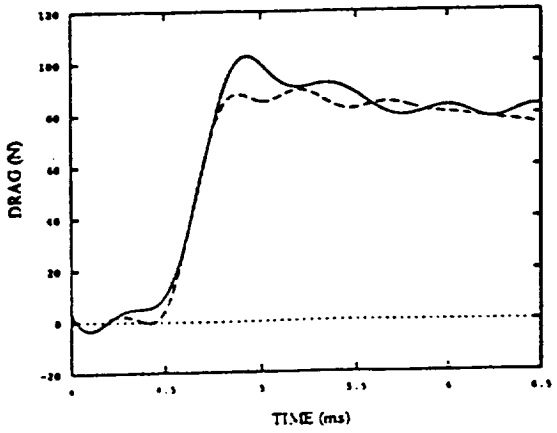
3. Results

(a) Drag on the 5° Semi-Angle Cone

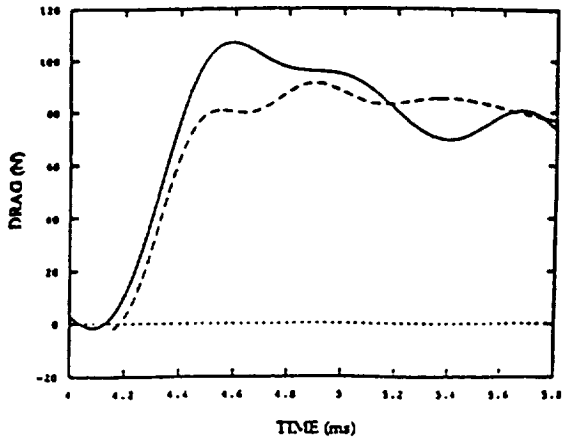
Figure 2 shows the deconvolved, measured drag on the 5° cone compared with a theoretical prediction using Taylor-Maccoll[7] cone flow theory, a skin friction approximation and a base pressure approximation. The skin friction is assessed using a reference temperature method and Sutherland's viscosity law. An entirely laminar boundary layer is assumed. The base flow is complicated by the presence of the sting and a buffer placed within 2 mm of the base of the cone. Base pressure is approximated by assuming the flow between the base and the plastic buffer located just behind the model is choked. The strain time histories measured in the sting were deconvolved using an experimentally obtained impulse response. The deconvolution process amplifies the experimental noise, so the results have been filtered with an 8-pole Butterworth low-pass filter with a cut-off frequency of 2 kHz. The test time in T4 is designated as the period in which the ratio of Pitot to stagnation pressure is constant. The tunnel was operated with a Mach 5 contoured nozzle and near-tailored conditions are attained for approximately one millisecond.



Nozzle supply conditions : enthalpy = 3.4 MJ/kg, pressure = 35.2 MPa; freestream conditions : pressure = 8.94 kPa, temperature = 344 K, velocity = 2390 m/s, density = .04956 kg/m^3, γ = 1.39.



Nozzle supply conditions : enthalpy = 6.8 MJ/kg, pressure = 43.6 MPa; freestream conditions : pressure = 11.5 kPa, temperature = 781 K, velocity = 3446 m/s, density = .0905 kg/m^3, γ = 1.36.



Nozzle supply conditions : enthalpy = 11.3 MJ/kg, pressure = 41.5 MPa; freestream conditions : pressure = 12.2 kPa, temperature = 1410 K, velocity = 4389 m/s, density = .0291 kg/m^3, γ = 1.32.

Fig2. Comparison of experimental and theoretical drag on a 5° cone at zero incidence.
_____ deconvolved measured drag
- - - - - theoretical drag

The test gas is nitrogen. This eliminates dissociation effects. Results were obtained for three different nozzle supply enthalpies. The nozzle supply enthalpy is varied by varying the pressure of the test gas in the shock tube. The nozzle supply pressure is varied by changing the thickness of the steel primary diaphragm between the driver and shock tubes. Results were obtained for nozzle supply enthalpies from 3 to 13 MJ/kg for two primary diaphragm thicknesses (4 and 5 mm). The results are summarised in Figure 3 in terms of drag

coefficient. The reference area for the coefficient is the base area of the cone.

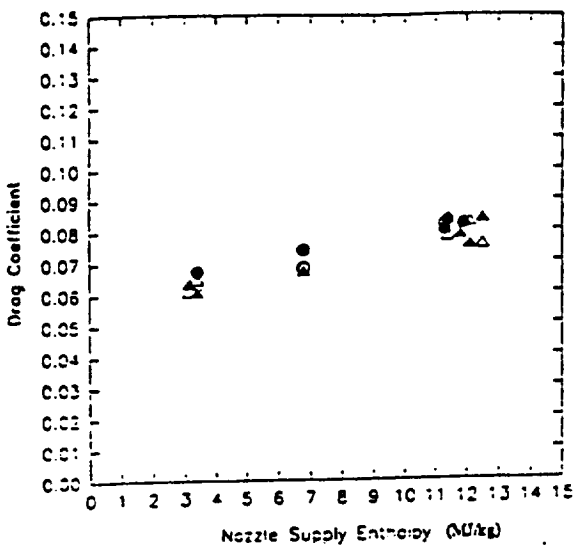


Fig. 3 Variation of drag coefficient with nozzle supply enthalpy for a 5° cone at zero incidence.

A single value of drag is obtained for each shot by averaging the signals over a 300 μs period from the start of the test time. The theoretical levels (open symbols) are compared with the experimental results (closed symbols). The triangles represent the lower pressure 4mm diaphragm condition and the circles are the high pressure 5 mm conditions. Very good agreement is observed (within 10%) and a trend of increasing drag coefficient with increasing supply enthalpy is apparent. This trend can be associated with the performance of the nozzle. The Mach number of the flow exiting the nozzle changes with nozzle supply enthalpy due to differences in the behaviour of the test gas at high temperature (the gas may not expand in chemical equilibrium) and because of possible differences in the growth of the nozzle boundary layers. The exit Mach number decreases with nozzle supply enthalpy over the range of the present experiments. The components of the drag coefficient associated with surface pressure and with skin friction both increase with nozzle supply enthalpy.

(b) Three-Component Force Measurement

The viability of the stress wave balance was demonstrated by the uniaxial drag measurement on the initial 15° cone and the 5° cone described above. The technique has been extended to the simultaneous measurement of several components of force, namely lift, drag and pitching moment.

The major modification here is in the method of attachment of the model to the sting. The aim is to minimise the coupling amongst signals which are used to determine the axial and normal forces and the pitching moment.

The three-component deconvolution force balance consists of a single, 2 m long sting attached to the test model by four short bars (Figure 4). Each of the short bars is instrumented for measurement of axial strain at its mid-point. A strain gauge bridge is also attached to the sting 200 mm from the model/sting junction. Combinations of the strain signals from the four bars are used to produce two output signals - one responding primarily to an axial force input signal and the other responding primarily to a pitching moment input signal. The strain measurement in the sting responds primarily to an axial force input. Inevitably there is some coupling amongst these output signals.

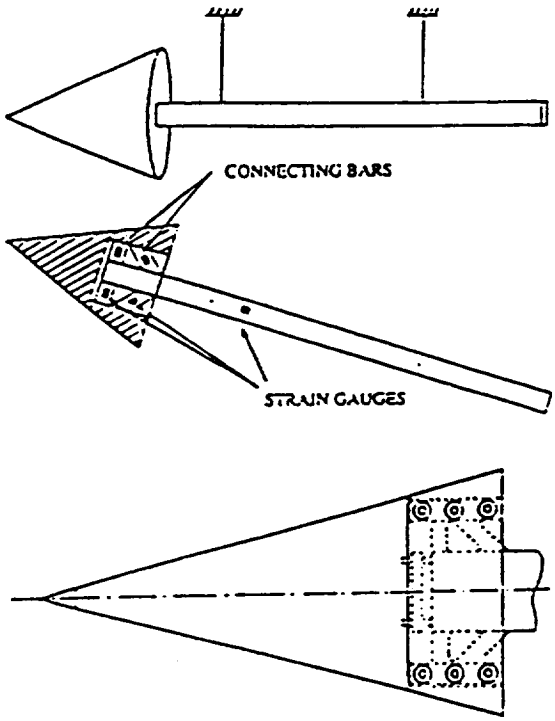


Fig. 4 Three component balance with details of the connection to the sting.

The time histories of the three outputs related to axial and normal forces and moment, $y_A(t)$, $y_N(t)$ and $y_M(t)$, can be related to the time-histories of the axial force, normal force and pitching moment on the model, $u_A(t)$, $u_N(t)$ and $u_M(t)$ via nine impulse response functions. This coupled convolution problem can be written in matrix notation as in Mee et al.[8]

$$\begin{pmatrix} y_A \\ y_N \\ y_M \end{pmatrix} = \begin{pmatrix} G_{AA} & G_{AN} & G_{AM} \\ G_{NA} & G_{NN} & G_{NM} \\ G_{MA} & G_{MN} & G_{MM} \end{pmatrix} \begin{pmatrix} u_A \\ u_N \\ u_M \end{pmatrix}$$

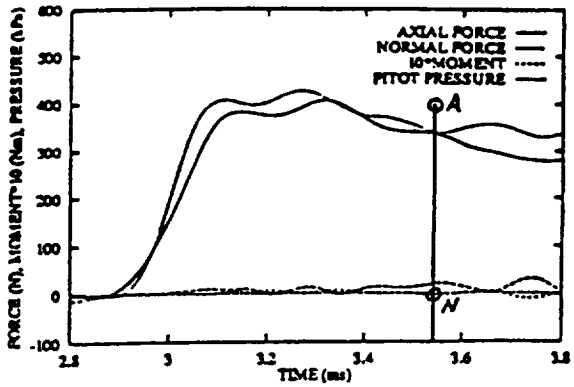
where the y vectors are formed from the discretised output signals and the u vectors are formed form the applied load time histories. The square G matrices are formed from the impulse response functions, G_{ij} being the impulse response for the y_i output to a u_j input. If there is no coupling amongst the outputs then the off-diagonal submatrices in the impulse response matrix will be null.

The nine impulse response matrices are obtained by a series of bench test in which a weight is attached to various points of the model by a fine wire and then quickly released. The output strain signals are processed to produce the impulse responses. The linearity of the system enables the responses to flow-type loading distributions to be determined by superposition of the results of several tests for single loads applied at various locations on the model.

In experiments in the shock tunnel, each of the y_i outputs is measured and time domain, coupled deconvolution techniques are used to determine the time histories of the lift and drag forces and pitching moment on the model. The experimentally determined impulse response functions are used for this deconvolution.

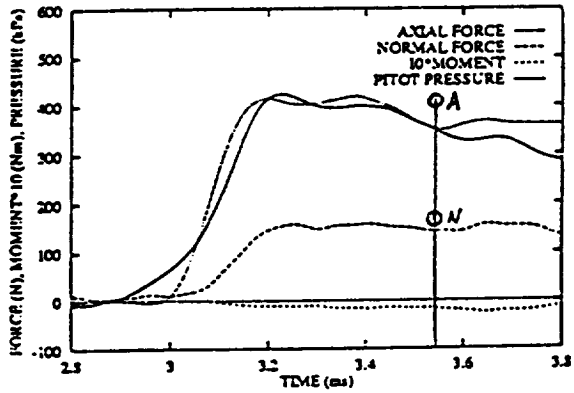
The prototype three-component balance was installed in a 220 mm long, 15° semi-angle, aluminium cone as shown in Figure 4. The cone mass is 1.94 kg. This configuration was also found to be quite insensitive to loading distribution.

Experiments were performed to measure the three components of force on the 15° cone for incidences of 0.0°, 2.5° and 5.0°. Sample results are presented for a nozzle supply enthalpy of 6 MJ/kg in Figure 5. Shown are the deconvolved axial and normal forces and pitching moment as well as the measured Pitot pressure in the test section. The zero for moment has been taken at a point one third of the cone height from the base of the cone, on the axis. (The theoretical line of action of force for a conical, inviscid flow is about 5% of the cone height closer to the base.) A negative moment with a positive normal force indicates the line of action of the net force is closer to the base than the nominal location. All results have been digitally low-pass filtered with a 4-pole Butterworth filter at a cut-frequency of 5 kHz. The vertical line on each plot indicates the time at which nozzle starting is complete and the commencement of steady test flow (based on a constant ratio of Pitot to supply pressures).

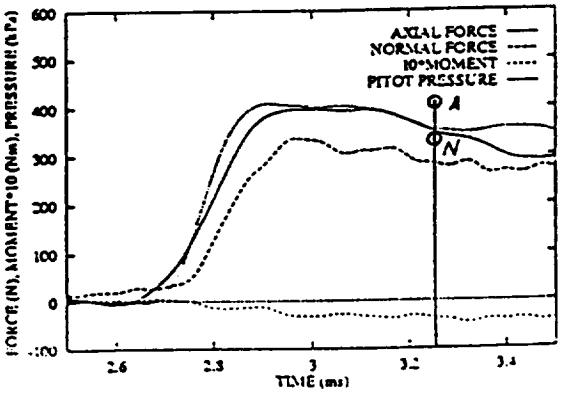


(a) 0.0° incidence

Fig. 5 Deconvolved force and moment time histories. Nozzle supply conditions : enthalpy = 6.5 MJ/kg, pressure = 25 MPa; freestream conditions : temperature = 800 K, velocity = 3400 m/s, density = .033 kg/m^3, γ = 1.36.



(b) 2.5° incidence



(c) 5.0° incidence

The response of the balance is seen to be good with the axial and normal forces showing time histories similar to the Pitot pressure. The current arrangement is such that there are about 800 μs before the waves reflected from the end of the sting return to the locations of strain measurement and interfere with the measurements. This can be seen in the deconvolved axial force signals where the level drops shortly after the measurement time. A longer sting would overcome this limitation on measurement time.

The experimental results are compared with computations of Jones[9]. He presents results of calculations of the axial and normal forces on cones at small angles of attack for various supersonic and hypersonic Mach numbers. The computations are for an inviscid flow of a perfect gas with a ratio of specific heats γ, of 1.4. (γ = 1.36 in the present experiments.) Interpolating on his results, predicted axial and normal forces are compared with the present measurements and are indicated on the plots of Figure 5 with "*A*" for axial force and "*N*" for normal force. There are experimental uncertainties in the conditions of the flow in the test section which may lead, for example, to an uncertainty in axial force of ±12%[10]. While the measured levels of force are about 15% lower than the computations of Jones, the ratios of axial to normal force agree well (to within 5% at this condition). The experimental line of action of force is within 1% of the inviscid, conical flow value for this condition. The overall accuracy of the balance has not yet been quantified.

(c) Scramjet Thrust Measurement

The two-dimensional thrust nozzle presents a challenging problem. The loading is not axisymmetric as in the case of a cone at zero incidence and the internal flow presents some design difficulties. A two-sting system has been chosen to accommodate the internal flow and achieve some symmetry. This can be seen in Figure 1. The nozzle is 300 mm long and together the nozzle and stings weigh 6.55 kg. The angle of the ramp walls is 11° and the area ratio is 4.76.

The situation is complicated by the fact that with the small ramp angle and the internal pressure on the nozzle walls, loading is predominantly transverse. Yet it is the axial thrust which is to be measured through detection of the tensile waves propagating in the stings. Although bending stress waves travel at most at only 60% of the speed of the axial stress waves, the system needs to be stiffened against bending. The second sting is only used to preserve symmetry. Thus, a redundant measurement is also obtained. The expected axial thrust from this nozzle is not large so thin stings are required. In addition to this, the contact area between nozzle and sting needs to be maximised. The result was that it was decided to twist the stings through 90°, without distorting their cross-sectional shape, just aft of the nozzle. This is discussed further in Simmons et al.[11]

Finite element analysis showed that this would not significantly alter the propagation of the axial stress wave in the sting, while the rigidity of the system is greatly increased.

Figure 6 shows the numerically predicted response of the nozzle to a step point load and the experimentally measured step response to a point load. The results indicate that the speed of response of the balance is adequate. The agreement between the computed and experimental responses is quite good. However, the unloading waves arrive approximately 50 μs earlier in the computation. This is possibly due to the material properties for the sting (such as Young's Modulus which determines stress wave speed) not being exactly correct for the particular brass being used for the stings.

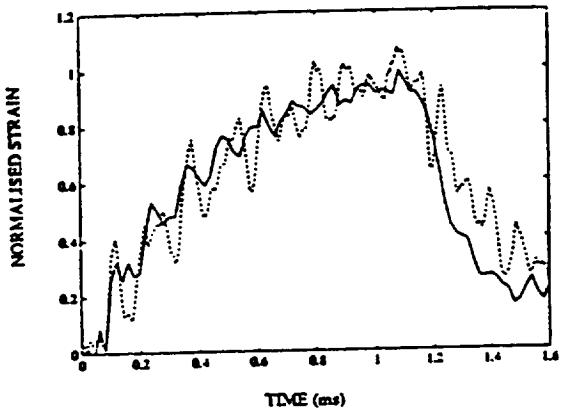


Fig. 6 Comparison of experimental and computational responses of the 11° thrust nozzle to a step point load at the nozzle front.
. experimental
_____ computational

The 300 mm long nozzle is freely suspended behind a fixed scramjet combustor. A Mach 4 contoured nozzle supplies the test gas to the combustion duct. Fuel is injected at the entrance to the duct from a two-dimensional central, planar strut. The combustor duct is 600 mm long. A 3 mm lip at the exit of the combustor will ensure there is no flow leakage, while simultaneously allowing free movement of the nozzle and stings. Around the perimeter of the lip there is approximately 0.5 mm of clearance with the nozzle. This is shown in Figure 7.

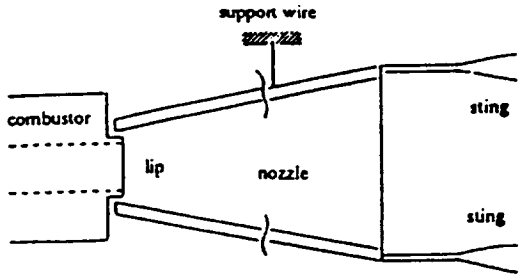


Fig. 7 Details of the join between the thrust nozzle and combustor.

The alignment of the nozzle behind the combustor has been one of the challenges of this experiment. Sufficient free movement is required to measure signals of a useful duration (production of positive thrust will accelerate the nozzle towards the combustor) while flow leakage onto the front face of the nozzle is undesirable.

The stings are mounted into the top surface of the nozzle ramp walls in order to keep them out of the nozzle exit plane (see Figure 7). The nozzle is shielded from the external flow and the two stings are shielded from the nozzle exit flow.

There are static pressure tappings in the ramp walls of the nozzle and a Pitot rake provides a survey of the flow at the exit of the nozzle. Combustor static pressures are also measured, and shots are repeated with the nozzle removed in order to measure the Pitot pressure across the combustor exit.

The thrust measured via the strain gauges will be the net axial load on the nozzle. This should be less than the thrust calculated from static pressure measurements by an amount equal to the skin friction. The skin friction is inferred by using a friction coefficient of .003 taken from the computations of nozzle skin friction by Schetz[12]. The Pitot pressure at ten locations down the nozzle is approximated from the measured exit values assuming isentropic flow through the nozzle. Hence the calculated skin friction will only be approximate.

Figure 8 shows the static pressure distribution down the nozzle ramp wall, while Figure 9 shows the Pitot pressure profile across the nozzle exit plane. These distributions are shown for three cases: hydrogen fuel injected into air (combustion), air with no fuel and hydrogen fuel injected into nitrogen (mixing). The shock tunnel nozzle supply enthalpy is 9 MJ/kg.

At this stage, the deconvolved signals are typically marred by large, oscillations. An example of this is shown in Figure 10, where the inferred net load on the nozzle is compared with the deconvolved strain measurement of the thrust.

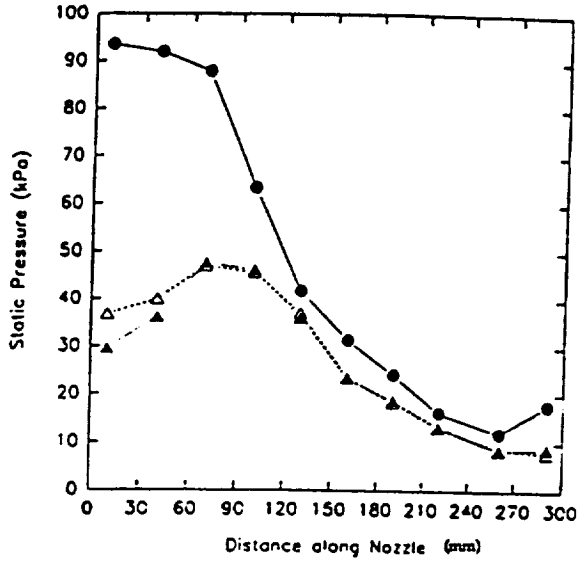


Fig. 8 Static pressures in the thrust nozzle.

● - combustion
△ - mixing
▲ - air only

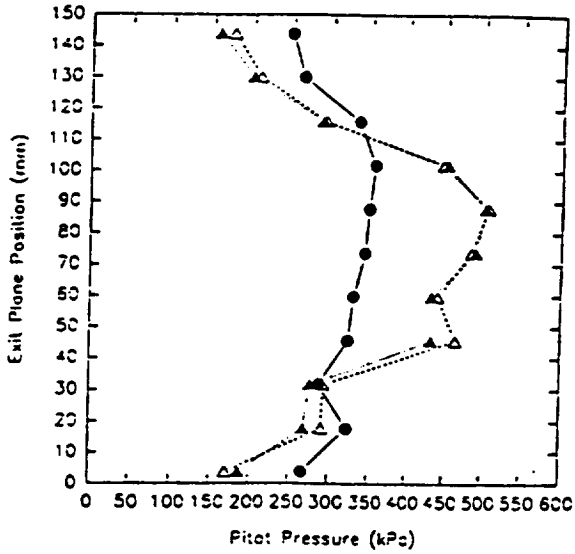


Fig. 9 Pitot pressures across the nozzle exit.

● - combustion
△ - mixing
▲ - air only

When these signals are filtered heavily, it can be seen that the mean level compares favourably with the net load inferred from the pressure

measurements and skin friction approximation. These oscillations are not introduced through the deconvolution and their source is currently being investigated. The general agreement in level is encouraging, but further testing and analysis is required.

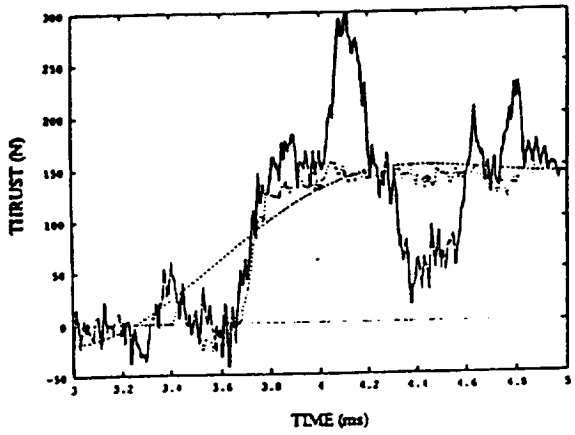


Fig. 10 - Deconvolved thrust signal compared with net thrust inferred from pressure measurements and a skin friction approximation.
____ unfiltered deconvolved thrust signal
- - - - filtered deconvolved thrust signal
. inferred net thrust

4. Conclusions

This paper has presented recent measurements made with single and multi-component stress wave force balances. The single component balance produces results in good agreement with predictions. The extension of the balance to measurement of non-axisymmetric loads has also been achieved with measurements of three components of force on a conical model. A balance is also being developed for measurement of the thrust produced by a scramjet nozzle of rectangular cross section. Preliminary results for this configuration show promise, but further development is required.

References

1. Carbonaro, M. "Aerodynamic Force Measurements in the VKI Longshot Hypersonic Facility", *New Trends in Instrumentation for Hypersonic Research*, (ed. A. Boutier), Kluwer, Dordrecht, pp 317-325, 1993.

2. Jessen, C, Gronig, H, "A Six Component Balance for Short Duration Hypersonic Facilities", *New Trends in Instrumentation for Hypersonic Research*, (ed. A. Boutier), Kluwer, Dordrecht, pp 295-305, 1993.

3. Naumann, K W, Ende, H, Mathieu, G, "Millisecond Aerodynamic Force Measurement Technique for High Enthalpy Test Facilities", *New Trends in Instrumentation for Hypersonic Research*, (ed. A. Boutier), Kluwer, Dordrecht, pp 307-316, 1993.

4. Sanderson, S.R., Simmons, J.M., Tuttle, S.L., "A Drag Measurement Technique for Free Piston Shock Tunnels", AIAA-91-0549, 29th Aerospaces Sciences Meeting, Reno, Nevada, Jan. 7-10, 1991.

5. Prost, R., Goutte, R., "Discrete Constrained Iterative Deconvolution Algorithms with Optimised Rate of Convergence", Signal Processing, 7, 209-230, 1984.

6. Sanderson, S.R., Simmons, J.M., "Drag Balance for Hypervelocity Impulse Facilities", AIAA Journal, Vol. 29, No. 12, pp. 2185-2191, December 1991.

7. Taylor, G.I. and Maccoll, J.W., "The Air Pressure on a Cone Moving at High Speed", Proc. Royal Soc. (London), Ser. A, 139, pp 278-297, 1932.

8. Mee, D.J., Daniel, W.J., Tuttle, S.L., Simmons, J.M., "Balances for the Measurement of Multiple Components of Force in flows of a Millisecond Duration", Proc. 19th International Symposium on Shock Waves, 26-30 July, Marseilles, France, 1993.

9. Jones, D.J.," Tables of Inviscid Supersonic Flow about Circular Cones at Incidence, γ = 1.4", AGARDograph 137, 1969.

10. Mee, D.J., "Uncertainty Analysis of Conditions in the Test Section of the T4 Shock Tunnel", Research Report 4/93, Dept. of Mech. Eng., The University of Queensland, 1993.

11. Simmons, J.M., Daniel, W.J., Mee, D.J., and Tuttle, S.L., "Force Measurement in Hypervelocity Impulse Facilities", *New Trends in Instrumentation for Hypersonic Research*, (ed. A. Boutier), Kluwer, Dordrecht, pp 285-294.

12. Schetz, J.A., Billig, F.S., Favin, S., "Numerical Solutions of Scramjet Nozzle Flows", J. Propulsion, Vol. 3, No. 5, 1986.

AIAA 94-2516

Measurement of Scramjet Thrust in Shock Tunnels

R. J. Stalker, J. M. Simmons, A. Paull, D. J. Mee
Department of Mechanical Engineering
The University of Queensland
Brisbane, Australia

18th AIAA Aerospace Ground Testing Conference
June 20-23, 1994
Colorado Springs, Colorado

MEASUREMENT OF SCRAMJET THRUST IN SHOCK TUNNELS

R.J. Stalker*, J.M. Simmons†, A. Paull‡, D.J. Mee§
Department of Mechanical Engineering, The University of Queensland
Brisbane, Australia

Abstract

By using results obtained in tests on supersonic combustion of hydrogen in air, the conditions governing model size and operating pressure levels for shock tunnel experiments on models of flight vehicles with scramjet propulsion are established. It is seen that large models are required. The development of the stress wave force balance is then described, and its use as a method of measuring thrust/drag on such models is discussed. Test results on a simple, fully integrated scramjet model, with intakes, combustion chambers, thrust surfaces and exterior surfaces, using a 13% silane 87% hydrogen fuel mixture, showed that a steady state with thrust generation could be achieved within the shock tunnel test time, and the thrust could be measured. Results are presented for a range of stagnation enthalpies, and show that the scramjet model produces net positive thrust at velocities up to 2.4 km/sec.

Nomenclature

D	length of combustion chamber
H_0	test section stagnation enthalpy
L	overall length of model
M_c	Mach number of entrance to combustion chamber
P	pressure at entrance to combustion chamber
P_0	shock tunnel nozzle reservoir pressure
T	temperature at entrance to combustion chamber
V	test section velocity
ΔI_{sp}	specific impulse increment
γ	ratio of specific heats in test gas
ϕ	fuel equivalence ratio

1. Introduction

The scramjet offers a method of propulsion which, in principle, is able to operate up to any flight speed and, in fact, seems likely to be effective for flight speeds approaching 5 km/sec. A considerable amount of research has been done on the components of scramjets, with the inlet, the combustion chamber and the thrust nozzle all receiving attention. The components have also been coupled together, to make a complete scramjet engine, and various forms of this type of engine have been subjected to experimental scrutiny[1,2].

However, the ultimate test of a propulsive device is its performance when installed in an appropriate flight vehicle. This is particularly true of the scramjet, where the need to integrate the aerodynamics of the vehicle and the operation of the engine is particularly acute. Where circumstances prevent extensive experimentation with a series of flight vehicles, the next best thing is experimentation in ground facilities with models of the engines installed in models of the vehicles. Notwithstanding the desirability, experimentation of this type has not been reported for the hydrogen fuelled scramjet, at least in the open literature, and the purpose of the present paper is to discuss experiments which indicate that this is possible.

At speeds above about 2.5 km/sec, impulse facilities offer the only means of producing wind tunnel type flows for aerodynamic testing. Chief among these is the shock tunnel which, in its various forms, is able to achieve speeds ranging up to orbital velocity. Therefore, because it covers the range of speeds likely to be associated with scramjet operation, the discussion is centred on experiments in a shock tunnel.

*Professor of Space Engineering

†Professor & Dean of Engineering

‡Research Fellow

§Lecturer

Copyright C1994 by the American Institute of Aeronautics, Inc. All right reserved

The paper begins by considering tests on a scramjet combustor and thrust nozzle combination. These tests are used to define the approximate overall size of a model incorporating a scramjet, and this is seen to make severe demands on conventional techniques of measuring force on the model. The development of a new technique is described, particularly as it applies to the measurement of drag or thrust. This technique is then used to measure the thrust/drag of a non-lifting configuration incorporating scramjets.

2. The Shock Tunnel

The experiments were conducted in the free piston shock tunnel T4 at The University of Queensland, with the exception of some of the early experiments on the combustor/nozzle combination, which were conducted on the free piston shock tunnel T3 at the Australian National University[3]. Since both tunnels are similar in concept, only T4 will be briefly described here.

The layout of T4 is shown in the sketch in Figure 1. The free piston travels along a compression tube 26 m long and 229 mm in diameter to compress and heat the driver gas, before rupturing a diaphragm leading to a shock tube 75 mm in diameter and 10 m long. A shock wave is driven along the shock tube and, upon reaching the end, ruptures a mylar diaphragm and initiates the flow in a contoured, axisymmetric, hypersonic nozzle with a throat diameter of 25 mm and an effective exit diameter of 250 mm. The flow passes through the test section as a free jet.

The reservoir conditions for the nozzle flow are obtained from measurements of the shock speed, the initial pressure in the shock tube and the pressure at the end of the tube following shock reflection. The test section conditions are obtained by computing the expansion of the test gas from the reservoir to the measured value of pitot pressure of the test section.

3. Considerations Regarding Model Size

(a) Combustor/Thrust Nozzle Tests

The experimental configuration used in these tests is shown in Figure 2. Hydrogen fuel was injected into a rectangular duct, with dimensions 25 mm x 50 mm, at the trailing edge of a strut 4.6 mm thick. The strut was mounted to span the 50 mm dimension at the midplane of the duct, and the hydrogen was injected supersonically. Generally, the flow produced by the shock tunnel nozzle passed directly into the duct, so that the combustor effectively operated in the "direct connect" mode. However, in some tests the combustion Mach number was varied by placing a simple intake consisting of a pair of opposing wedges immediately upstream of the duct.

A thrust nozzle was formed by deflecting one of the 50 mm wide walls of the duct as shown. The distance, D, from the point of injection to the beginning of the expansion wave generated by the corner at the beginning of the thrust nozzle was taken as the length of the combustion chamber. This was measured on the centreline of the combustion chamber, and was varied by using inserts in the duct wall immediately upstream of the thrust nozzle. The deflection angle of the thrust surface varied from 15° at a Mach number of 3.5 to 11° at a Mach number of 4.5, so the effective area ratio of the thrust nozzle varied from approximately 12 to 9[4,5]. The thrust was measured by integrating the pressure over the thrust surface and, noting the fuel mass flow through the injector, was converted into a specific impulse.

Using this configuration, the length of combustion chamber required to produce a given specific impulse with a particular combustion chamber inlet pressure, P, could be obtained. It can be argued, of course, that the same specific impulse may be produced with a shorter combustion chamber, and a different fuel injection pattern. However, practical considerations limit the number of injection points, and it seems unlikely that the combustion chamber length would be reduced by more than a factor of two by this approach, even when the combustion is mixing limited. Therefore it is reasonable to take the lengths of the combustion chamber measured in these tests as typical values.

Figure 3 shows the specific impulse increment ΔI_{sp} plotted against combustor inlet temperature for a Mach number of 3.6 ± .1. ΔI_{sp} is obtained by subtracting the thrust with no fuel injection from the thrust with fuel injection to obtain the thrust increment due to fuel injection. Two values of P and of D were chosen, such that the product PD is constant, and can be seen that although P and D individually varied by a factor of three, the thrust increment remained the same over the range of inlet temperatures.

It can be seen that ΔI_{sp} in Figure 3 exhibits a maximum at approximately 1000 K. This was a general feature of the experiments, and it was possible to plot the points at which a given level of maximum specific impulse increment was achieved on a graph of P Vs D, as in Figure 4. The data for this figure was obtained at equivalence ratios of 1.0 ± 0.1. Two levels of maximum specific impulse increment are considered, and it can be seen that there is a factor of two or three difference in the pressures needed to achieve the respective levels. (A question mark adjacent to one point indicates that experimental evidence suggests that the same ΔI_{sp} may have been obtained at a lower value of P). Two curves are shown, which represent an attempt to correlate the results according to the rule PD = constant. It can be seen that this is only partly successful, and that effects appear to be present which modify this rule. For example, the two experimental points at D = 575 mm were obtained at a combustor inlet Mach number of 4.5, whereas the other results were obtained at Mach numbers of 3.5 ± 0.2, indicating that combustor Mach number may be influencing the results. Notwithstanding this, it will be assumed that the rule PD = constant provides an order of magnitude estimate of the required combustion chamber length and pressure to yield a substantial specific impulse increment.

Also, the fact that the peak specific impulse increment occurred at a combustor inlet temperature of approximately 1000 K implies that the combustor inlet Mach number would be approximately one half of the Mach number achieved by a flight vehicle in which the combustor was installed or, in a shock tunnel, where the flight Mach number may not be simulated, the combustion Mach number would be approximately 1.5 times the free stream velocity in km/sec.

(b) Model Size and Shock Tunnel Requirements

From the results above, it is possible to make approximate estimates of the model size and the associated shock tunnel requirements pertaining to test of a scramjet propelled vehicle configuration.

The relation between model size and combustion chamber length depends, of course, on the design of the vehicle. However, the fact that such a vehicle would require a small forebody angle, and a not-so-large afterbody angle making a thrust surface, implies that the overall vehicle length may be expected to be an order of magnitude greater than the combustion chamber length. Therefore it is assumed that

$$L = 10\,D \qquad (1)$$

Now, the combustion chamber inlet pressure is determined by the combustion chamber inlet Mach number M_c and the nozzle reservoir pressure of the shock tunnel, P_0. Assuming isentropic compression in the scramjet intake, and a perfect gas,

$$P = P_0\left(1 + \frac{\gamma-1}{2} M_c^2\right)^{-\gamma/(\gamma-1)} , \qquad (2)$$

where γ is the ratio of specific heats. It is assumed that $\gamma = 1.3$. For a combustion chamber which yields a specific impulse increment of 1500 sec, the upper curve in Figure 4 applies approximately, and so

$$PD = 0.3 \text{ m.atm.} \qquad (3)$$

Thus, eqns (1), (2) and (3) enable the length of the model corresponding to given values of M_c and P_0 to be obtained.

Values so obtained are presented in Figure 5, for three values of the shock tunnel nozzle reservoir pressure. The curves show the extreme difficulty associated with testing at high combustor inlet Mach numbers. If a model length of 5 m and a nozzle reservoir pressure of 2000 atm. is taken as representing the practical limits of modern shock tunnel technology, then it can be seen that testing will be limited to a combustor inlet Mach number of 6, corresponding to a flight velocity of 4 km/sec. Whilst it should be noted that some rather sweeping approximations have been made in obtaining Figure 5, and therefore the values of L may, in practice, vary somewhat from those presented in the figure, the strong dependence on M_c implies that the limit will be close to the predicted value.

Thus, Figure 5 shows that the maximum combustion inlet Mach number in any shock facility depends on the length of the model which can be accommodated. In the absence of extensive regions of separated flow, the working rule for shock tunnels is that the length of the slug of test gas passing through the tests section should be at least 3L. Assuming that the test section size imposes no constraints on the model length, it follows that the maximum value of L is determined by the test time, which therefore determines the maximum combustion inlet Mach number, and hence the maximum flight velocity at which scramjet propulsion of a flight vehicle

can be simulated in the shock tunnel facility under consideration.

4. Force Measurement in Shock Tunnels - The Stress Wave Balance

(a) Background

The conventional method of measuring forces is to regard the model as lumped mass, and the force balance as a spring system, and to allow a sufficient number of oscillations to come to equilibrium before the force is measured. This is suitable for test times in excess of 10 milliseconds, and therefore cannot be used in much shorter test times of high performance facilities. Therefore a number of fast response techniques have been developed (e.g. ref.6) but although these do offer substantial improvements, they continue to be based on the assumption of a rigid model, and as a consequence, they require that the model be small relative to the tunnel size.

It is seen above that the model may be expected to be of a size such that the flow traverses only a few model lengths during the test time. Furthermore, stress waves induced in the model by the aerodynamic forces propagate at a speed ($3 \rightarrow 5$ km/sec for ordinary model materials such as steel or aluminium) which is comparable with the flow speed, and therefore the model is in an unsteady state of stress during the entire flow period. Thus the model cannot be regarded as rigid, and a method of measuring forces which takes this into account is required.

(b) The Stress Wave Force Balance

Fortunately, the stress waves which are the source of this difficulty can themselves be exploited to measure the force on the model[7]. By placing a strain gauge on the model support sting adjacent to the base of the model, the time history of stress waves passing into the sting is recorded, and this recording can be deconvoluted to yield the force on the model. The relation between the force applied to the model, u(t), and the output of the strain gauge, y(t) can be written as

$$y(t) = \int_0^t g(t-\tau)\, u(\tau)\, d\tau \quad , \qquad (4)$$

where g(t) is an impulse response function expressing the relation between the two.

A simple example of this, shown in Figure 6(a), occurs when the "model" is just an extension of the sting, and the force is applied as a step change in time at the upstream end. In this case the strain gauge records the passage of a stress wave which directly represents the applied load and, in eqn (4), g(t) is simply a delta function. If the model is a cylinder aligned with the flow, as shown in Figure 6, then the application of the force causes a stress wave in the model, which is partially reflected and partially transmitted into the sting at the model-sting junction. The reflected portion traverses the model and returns to the junction to transmit a further stress wave into the sting, and so on. The "ringing" of the stress wave in the model therefore produces a series of transmitted stress waves of decreasing amplitude in the sting, to eventually approach a steady state of stress. The time history of the stress waves in the sting is as shown in Figure 6(b), and g(t) is a series of delta functions.

In either of the above two cases, g(t) is of a sufficiently simple form that the integral in eqn (4) can be readily deconvoluted, and u(t) can be deduced from g(t). However, as the models become more complicated, so does the deconvolution, and it is necessary to use computational techniques.

The impulse response function for a particular model-sting combination can be found either experimentally or by using a dynamic finite element analysis. Tests to date have tended to use the experimentally determined impulse response function, with that determined computationally retained for checking. The experimental determination was assisted by the fact that the model sting was a simple stress wave bar 2 m long, manufactured from 32 mm diameter brass tubing of 1.63 mm wall thickness. This could be readily removed from the shock tunnel with the model attached, and suspended by a fine wire attached to the tip of the model. The wire was then out close to the model to produce a sudden removal of tensile load. This is equivalent to a step-like drag load applied at the tip of the model. The output from strain gauges mounted on the stress wave bar 200 mm from the base of the model then gave the step response for the system, and this response was differentiated with respect to time to yield the experimental impulse response function.

When this technique was first proposed[7] it was applied to the measurement of drag on a short cone, with the results shown in Figure 7. It can be seen that the drag followed the pitot pressure in the test section within 0.2 to 0.3 millisec of

initiation of the flow. In this case the internal stress waves were unimportant, but subsequent measurements on a 425 mm long cone[8], where they were important, showed that they could be taken into account satisfactorily, as shown in Figure 8. Once again it can be seen that the drag follows the pitot pressure within approximately 0.3 millisec. Then measurements of drag of a 5° cone, with varying degrees of nose blunting, showed that the method could accommodate peaks in the load distribution, as represented by a blunt nose[9]. Some results of these tests are shown in Figure 9. Computational modelling indicated that the distribution of force had negligible effect, and only the total drag on the model would be recorded. This was confirmed by the experiments.

During the tests on the blunted cones, it was found that the impulse response function g(t) could be extended in time to take account of stress wave reflections at the downstream end of the stress wave bar. Before this, it was thought that the measurement would be terminated by arrival of these reflected waves at the strain gauge. The extension of time that was made possible by accommodating these reflections was important in scramjet model testing, as will be see below.

With completion of these tests, it was thought that the method was sufficiently developed to apply to thrust/drag measurement of a scramjet model.

It will be observed that in all the tests, the stress wave bar was suspended horizontally in the tunnel by two fine wire threads. Attachment of these threads to the bar did not produce an observable effect on stress wave propagation in the bar.

5. Scramjet Model Thrust/Drag Measurement

(a) The Model

A sketch of the scramjet model and fuel tank is shown in Figure 10. The scramjet centrebody, shown in streamwise section in the figure, consisted of a conical forebody with 9° half angle, a cylindrical section of 51 mm diameter, and an afterbody of 10° half angle. It was partly surrounded by a axisymmetric cowl, which had an internal diameter of 67 mm over the parallel section of the centrebody, and was of 71 mm outside diameter. Filler pieces, which are not shown, divided this parallel section into six constant area combustion chambers, each of which subtended an angle of 26° at the centreline. Fuel was injected through six orifices, each 2 mm in diameter and angled at 30° to the centreline. They were located at the upstream end of the combustion chambers. The filler pieces between the combustion chambers extended upstream in the form of intake compression ramps which processed the flow in the forebody shock layer through two shocks, each of 8° deflection. The leading edges of the cowl were shaped to prevent these shocks spilling from the intake, thus forming a convergent duct leading to the combustion chambers. The radial dimension of this duct was 10 mm.

The fuel supply system is also shown in the figure. The fuel tank was filled before a test, and the supply valve remained closed until the test was initiated. The recoil of the shock tunnel closed a switch to operate the solenoid valve, which opens the supply valve. As the fuel flowed to the model and fuel injection orifices, its pressure was monitored by a PCB piezoelectric pressure transducer. The system was designed so that sonic flow occurred at the orifices. As shown, the fuel tank and valve assembly was shielded from the flow by an aerodynamic shroud. In normal operation, the upstream end of this shroud was located 50 mm downstream of the termination of the scramjet afterbody, and to check that this was sufficient for the shroud to have no influence on the forces on the scramjet, a test was run with an insert to increase this distance to 125 mm. No change in the measured force was observed.

The pressure measured by the pressure sensor, together with calibration factors for the injection orifices were used to determine the mass flow rate of the fuel. This was varied by changing the filling pressure of the fuel tank. The stress bar was mounted horizontally, as in the previous tests.

(b) Measurements

The model employed here was larger and more complicated than the cones of the previous studies, so it was necessary to again check that the distribution of forces was not important. This was done numerically. A two dimensional axisymmetric finite element 70 x 6 mesh was made to represent the model and fuel tank, and three point loads were applied which approximately represented the loading on the model during a test. One represented the drag

of the model, and was applied at the nose, one represented thrust due to fuel injection, and was applied at the location of the injection orifices, and one represented the thrust due to mixing and combustion, and was applied at a point halfway along the thrust surface. The variation with time of each of these is shown in Figure 11(a). Together these three produced the strain gauge response shown in Figure 11(b). This was then deconvolved, using only the impulse response function g(t) for the load at the nose, to see if the applied time history of the force on the model could be recovered. The result is shown as the solid line in Figure 11(c), where it is compared with the sum of the three forces acting on the model. It can be seen that, apart from a time delay of about 100 μ sec, the deconvolved signal is in good agreement with the input signal, signifying that the measured value of force was independent of its distribution.

This also confirmed that the experimental method of determining g(t) could be used for this configuration.

A typical strain gauge output obtained when fuel is injected is shown in Figure 12. The operation of the solenoid valve was timed so that the fuel injection pressure began to rise approximately 5 milliseconds before initiation of the test flow, reached its test value approximately 0.5 milliseconds before flow initiation, and remained approximately constant for 3 milliseconds. The thrust due to fuel injection therefore begins some 3 milliseconds before the test flow, and this is evident on the strain gauge output. Then the flow starting processes and the fuel induced combustion produce larger forces, which lead to more rapid variations in the gauge output.

Records such that in Figure 12 were deconvolved using the experimentally determined g(t), leading to force time histories as shown in Figure 13. The test section pitot pressure and static pressure are presented in Figure 13(a), and display approximately steady conditions during the test time. Figure 13(b) shows three force histories. One is obtained when fuel is not injected and the test gas is air. Then the scramjet drag is 150 ± 20 N. Another is obtained when nitrogen is used as test gas and fuel is injected. Then the drag is approximately 50 N less than the fuel off test in air. There is a small difference in flow conditions between air and nitrogen test gases, however the drag reduction is due primarily to the injection of fuel. It can be seen that, prior to arrival of the test flow, fuel injection induces a thrust of approximately 30 N. The remaining 20 N reduction in drag possibly results from fuel/test gas flow interactions.

Finally, Figure 13(c) displays the result of injecting fuel with air test gas. Prior to the test flow fuel injection again induces a net thrust of 30 N. Then, as the flow over the model is established the drag increases, closely following the result obtained with nitrogen test gas. However, ignition of the fuel then causes thrust, which increases until it becomes quasi-steady at a net thrust of 60 ± 15 N. This, in conjunction with the other two time histories, clearly demonstrates that a steady state of thrust can be generated by a scramjet model in the test time of a shock tunnel, and that it can be measured.

(c) Results and Discussion

Measurements of the thrust/drag obtained over a range of stagnation enthalpies are presented in Figure 14. Because the stress wave balance was still under development, the model was conservatively sized, and so the dimensions were not sufficient to produce combustion of pure hydrogen at the chosen shock tunnel operating pressures (measurements showed P = 1 atm. which according to Figure 4, is too small to yield vigorous combustion). This was confirmed experimentally. Therefore Silane (SiH_4) was used as an ignition promoter, and the experiments were conducted with a fuel mixture of 13% SiH_4 and 87% H_2, injected at an equivalence ratio of 0.8.

The variation of the thrust with tunnel stagnation enthalpy, or with the computed test section velocity, is shown in Figure 14. It can be seen that although the net thrust is positive around stagnation enthalpies of 3 MJ/kg, it falls off rapidly with increasing stagnation enthalpy. This is largely due to the increase in pre-combustion temperature as the stagnation enthalpy is increased. An attempt was made to increase the maximum thrust measured by either increasing the amount of fuel injected, or by lowering the tunnel stagnation enthalpy. In both cases unsteadiness in the flow resulted, suggesting the onset of thermal choking.

In order to confirm that the flow in the combustors was supersonic when combustion was taking place, pitot and static pressures were measured at the downstream end of one of the ducts just upstream of the expansion caused by the upstream corner of the afterbody. At a

stagnation enthalpy of 3.3 MK/kg the ratio of the two was 4.1, yielding a Mach number of 1.75 ± 0.1.

The variation of the drag of the model in the absence of fuel injection is also shown, and it can be seen that this dominates the overall performance of the model. This is not surprising, as little attention was given to optimising the aerodynamics, both internal and external, of the model. With attention given to this aspect, a considerably improved overall performance may be expected.

6. Conclusion

The discussion centred on Figure 5 emphasised the importance of maximising the model size if scramjet propulsion of vehicles at flight velocities of 3 to 4 km/sec is to be studied experimentally. The model used in these studies was designed with the primary aim of testing the use of the stress wave force balance, so was less than the maximum size possible in the tunnel. In fact, the length of the portion on which force was measured was approximately 0.3 m, while the length of the model assembly which governed the operation of the stress wave balance included the fuel tank, and therefore was 0.7 m, It is therefore clear that scope exists for use of a larger model, in which the fuel tank is integrated into the model, and this may be expected to allow combustion of pure hydrogen fuel.

The results of the tests performed to date are encouraging. The fact that it was possible to produce a quasi-steady state involving positive net thrust on an integrated configuration, and that the thrust could be measured, implies that the prospects for development and testing of scramjet propulsion at high flight speeds are considerably enhanced by the use of shock tunnels.

Acknowledgments

The authors would like to express their appreciation of the support provided by the Australian Research Council, and through NASA grant NAGW-674.

References

1. Billig, F.S. "Research on Supersonic Combustion" J. Prop & Power, V9 pp499-514, Jul-Aug 1993.
2. Anderson, G.Y., Bencze, D.P. & Sanders, B.W. "Ground tests confirm the promise of hypersonic propulsion" Aerospace America V25, No.9, pp38-42. Sept. 1987.
3. Stalker, R.J. "Development of a Hypervelocity Wind Tunnel" Aeron. J. of Royal Aero Soc. V76, pp374-384. June 1972.
4. Stalker, R.J. & Morgan, R.G. "Supersonic Hydrogen Combustion with a Short Thrust Nozzle" Comb. and Flame V57, pp55-70 July 1984.
5. Paull, A. "Hypersonic Ignition and Thrust Production in a Scramjet" AIAA paper 93-2444. Presented at AIAA/SAE/ASME/ASEE 29th Joint Propulsion Conference. Monterey, CA. June 28-30. 1993.
6. Naumann, K.W., Ende, H., Mathieu, G. & George, A. "Millisecond Aerodynamic Force Measurement with Side-Jet Model in the ISL Shock Tunnel" AIAA Journal, V31, pp1068-1074, June 1993.
7. Sanderson, S.R. & Simmons, J.M. "Drag Balance for Hypervelocity Impulse Facilities" AIAA Journal, V29, pp2185-2191. Dec 1991.
8. Simmons, J.M., Daniel, W.J., Mee, D.J. & Tuttle, S.L. "Force Measurement in Hypervelocity Impulse Facilities" in New Trends in Instrumentation for Hypersonic Research (ed. A. Boutier), Kluwer Academic Publishers, Amsterdam 1993, pp285-294.
9. Porter, L.M., Mee, D.J. & Simmons, J.M. "Measuring the effect on Drag Produced by Nose Bluntness on a Cone in Hypervelocity Flow" Proc. 11th Australasian Fluid Mechanics Conference(ed. M. Davis and G. Walker), Univ. of Tasmania, Hobart, Australia, 14-18 Dec, 1992, pp287-290.

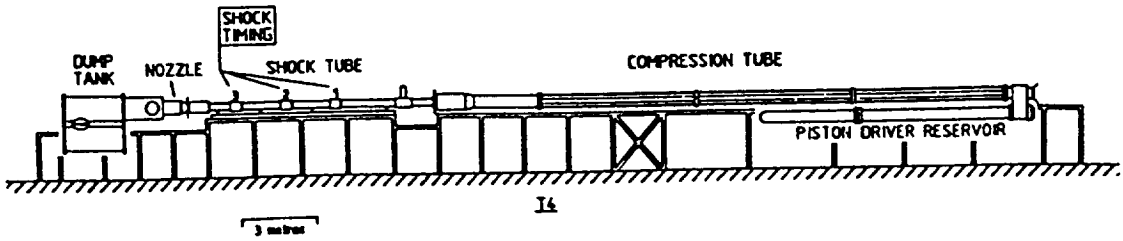


Fig. 1. Shock Tunnel T4

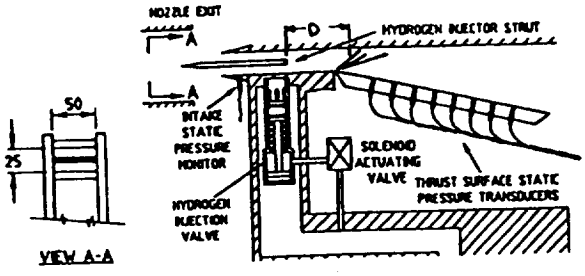


Fig. 2. Combustion Scaling Model

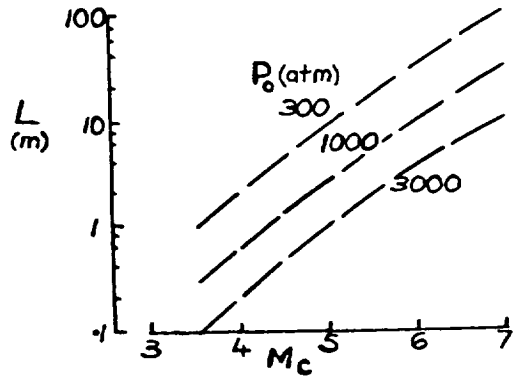


Fig. 5. Model Length

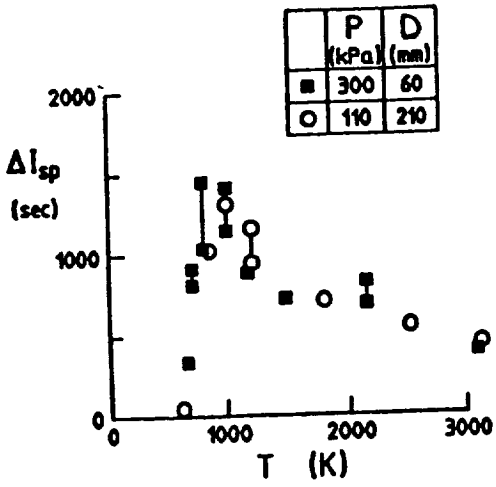


Fig. 3. Scaling of Combustion

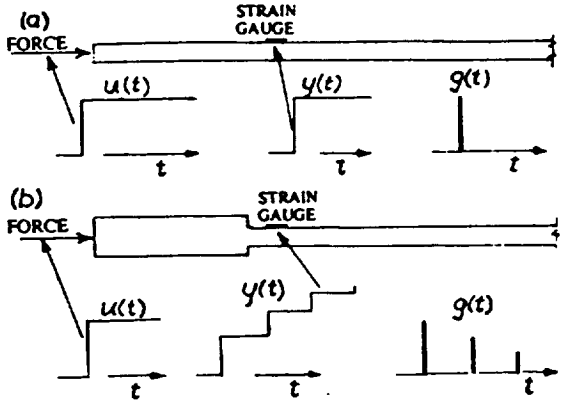


Fig. 6. Stress Wave Transmission

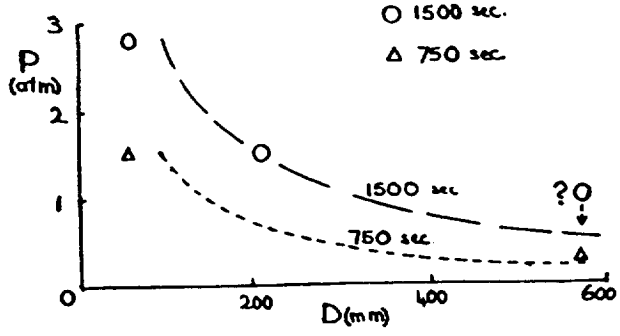


Fig. 4. Combustion Length for Thrust Generation

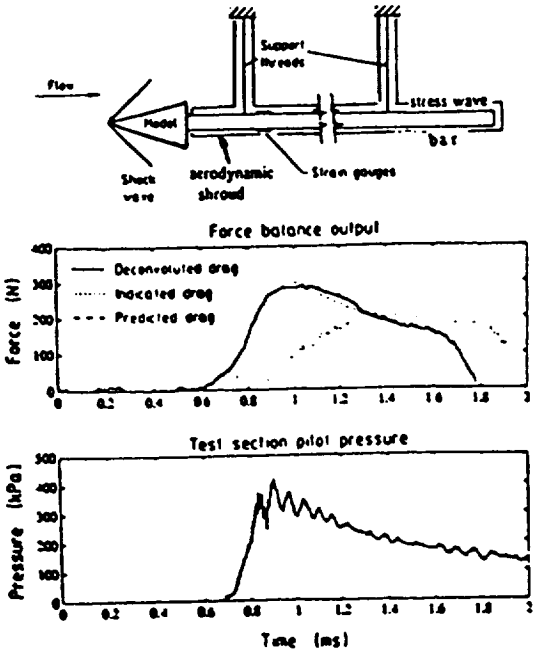


Fig. 7 Drag on 15° semi-vertex angle Cone H_0 = 4.0 MJ/kg, P_0 = 24 MPa

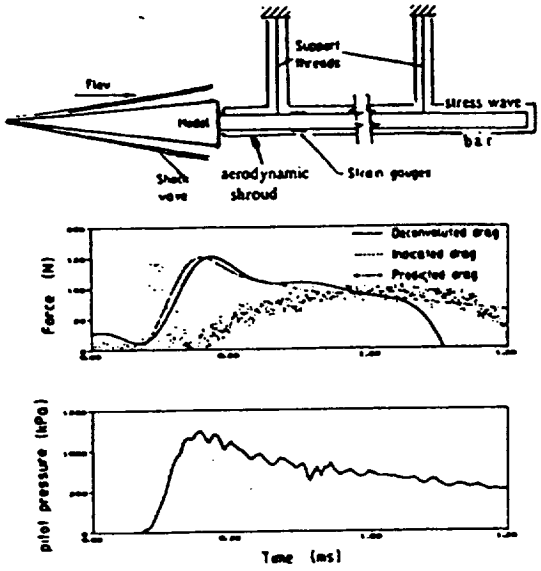
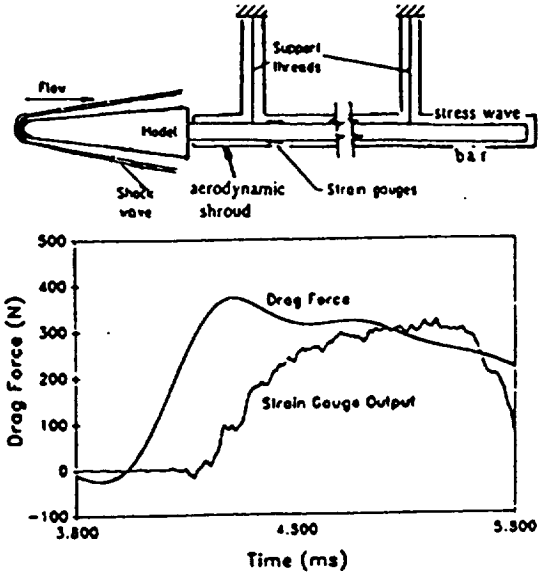


Fig. 8 Drag on 5° semi-vertex angle Cone H_0 = 7.8 MJ/kg, P_0 = 60 MPa



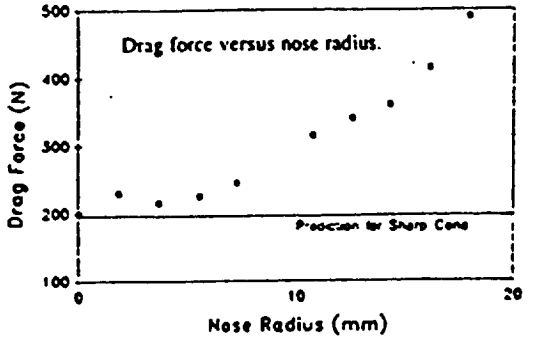


Fig. 9 Effect of nose blunting on drag of 5° semi-vertex angle Cone H_0 = 14.4 MJ/kg, P_0 = 38 MPa.

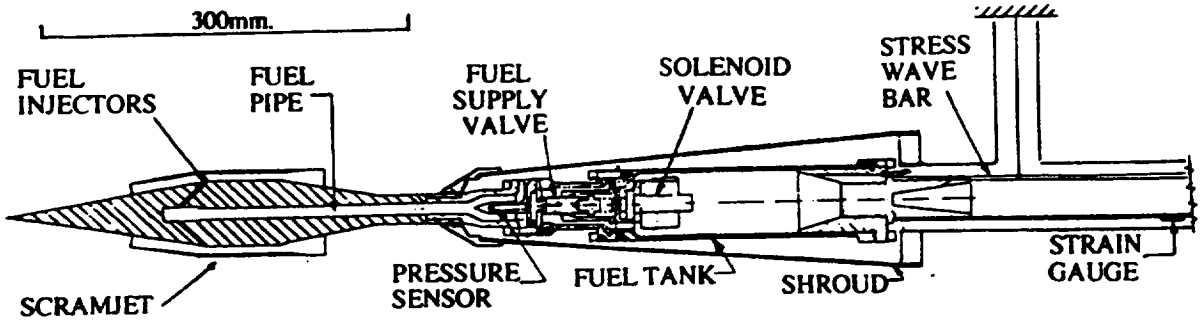


Fig. 10. Scramjet model and Fuel Tank Mounted on Stress Wave Bar

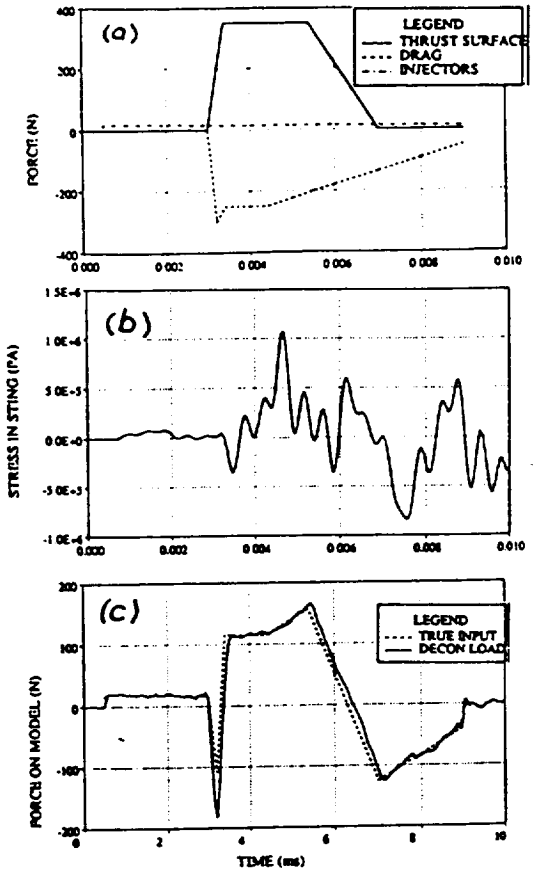


Fig. 11 Simulation of Distributed Load

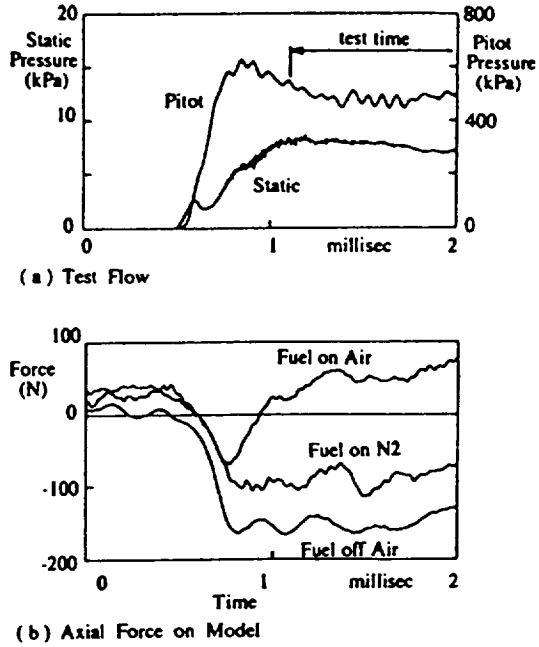


Fig. 13 Test Records showing generation of Net Thrust. H_0 = 3.2 MJ/kg; P_0 = 37 MPa.

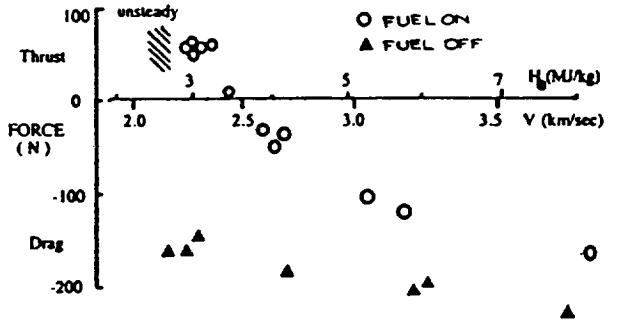


Fig. 14 Scramjet Thrust Measurements. P_0 = 37 ± 2.5 MPa, ϕ = 0.8.

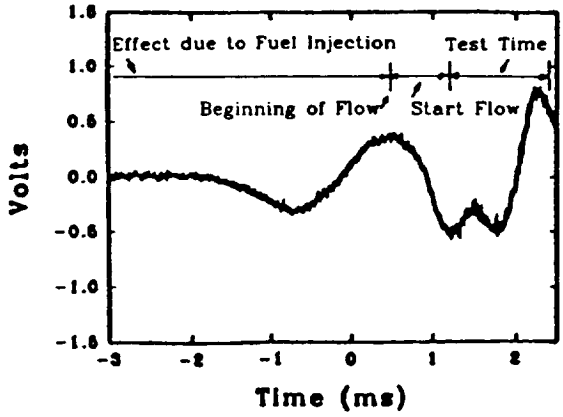


Fig. 12 Typical strain gauge output for Scramjet Tests.

[*Reprinted from* THE AERONAUTICAL JOURNAL OF THE ROYAL AERONAUTICAL SOCIETY, *May 1995*]

Scramjet thrust measurement in a shock tunnel

A. PAULL, R. J. STALKER and D. J. MEE
Department of Mechanical Engineering,
The University of Queensland,
Brisbane, Australia

PRINTED BY MANOR PARK PRESS LIMITED, EDISON ROAD, HAMPDEN PARK, EASTBOURNE, SUSSEX, ENGLAND
AND PUBLISHED BY THE ROYAL AERONAUTICAL SOCIETY, 4 HAMILTON PLACE, LONDON W1V 0BQ, ENGLAND

Scramjet thrust measurement in a shock tunnel

A. PAULL, R. J. STALKER and D. J. MEE
Department of Mechanical Engineering,
The University of Queensland,
Brisbane, Australia

INTRODUCTION

This note reports tests in a shock tunnel in which a fully integrated scramjet configuration produced net thrust. The experiments not only showed that impulse facilities can be used for assessing thrust performance, but also were a demonstration of the application of a new technique[1] to the measurement of thrust on scramjet configurations in shock tunnels. These two developments are of significance because scramjets are expected to operate at speeds well in excess of 2 km/s, and shock tunnels offer a means of generating high Mach number flows at such speeds.

THE MODEL AND TEST FACILITY

A sketch of the scramjet model and fuel tank is shown in Fig. 1 and a photograph of the model during a test is displayed in Fig. 2. The scramjet centrebody, shown in streamwise section in Fig. 1, consisted of a conical forebody with 9° half angle, a cylindrical section of 51 mm diameter, and an afterbody of 10° half angle. It was partly surrounded by an axisymmetric cowl, which had an internal diameter of 67 mm over the parallel section of the centrebody, and was of 71 mm outside diameter. Filler pieces, the trailing edges of which can be seen in Fig. 2, divided this parallel section into six constant area combustion chambers, each of which subtended an angle of 26° at the centreline. Fuel was injected through six orifices, each 2 mm in diameter and angled at 30° to the centreline. They were located at the upstream end of the combustion chambers. The filler pieces between the combustion chambers extended upstream in the form of intake compression ramps which processed the flow in the forebody shock layer through two shocks, each of 8° deflection. The leading edges of the cowl were shaped to prevent these shocks spilling from the intake, thus forming a convergent duct leading to the combustion chambers. The radial dimension of this duct was 10 mm.

The fuel supply system is also shown in Fig. 1. The fuel tank was filled before a test, and the supply valve remained closed until the test was initiated. The recoil of the shock tunnel closed a switch to operate the solenoid valve, which opened the supply valve. As the fuel flowed to the model and fuel injection orifices, its pressure was monitored by a PCB piezoelectric pressure transducer. The system was designed so that sonic flow occurred at the orifices. As shown, the fuel tank and valve assembly was shielded from the flow by an aerodynamic shroud. In normal operation, the upstream end of this shroud was located 50 mm downstream of the termination of the scramjet afterbody, and to check that this was sufficient for the shroud to have no influence on the forces on the scramjet, a test was run with an insert to increase this distance to 125 mm. No change in the measured force was observed.

The experiments were done in the free piston shock tunnel T4 at the University of Queensland which had a shock tube 10 m long and 76 mm in diameter. A mixture of argon and helium was used as the driver gas, and the ratio of the two was varied as the stagnation enthalpy was varied to ensure that a sufficient period of approximately constant nozzle stagnation pressure was maintained throughout the tests. The contoured hypersonic nozzle used for the tests had a throat diameter of 25 mm and a test section diameter of 250 mm, and was operated with a reservoir pressure of $37{\cdot}5 \pm 2{\cdot}5$ MPa.

A time integrated photograph of the scramjet during a test is displayed in Fig. 2. The main features of the scramjet, including three of the intakes and corresponding exhaust, can be seen. The luminosity results from the combustion of the fuel, and was absent when fuel was not injected. As might be expected it is most intense in the exhaust region, but light also originates from the intakes and around the cowl. However, this may have been generated during the processes of initiation or breakdown of the flow, so it should not be used to interpret flow behaviour during the test time.

THE STRESS WAVE FORCE BALANCE

A stress wave force balance, as originally outlined by Sanderson and Simmons[1], was used to measure the axial force on the model. They employed the method to measure the drag on a short cone, but it has since been developed for longer cones[2], and for long cones with the load distribution imparted by a blunt nose[3]. Essentially, it involves measurement by a strain gauge of the time variation of stress induced in a stress wave bar by the forces on the model, and deconvolution of the resultant record to obtain the net force on the model. As shown in Fig. 1, the stress wave bar was attached to the downstream end of the fuel tank, and the

Manuscript received 5 April 1994, revised version received 20 January 1995, accepted 27 January 1995.
Paper No. 2023.

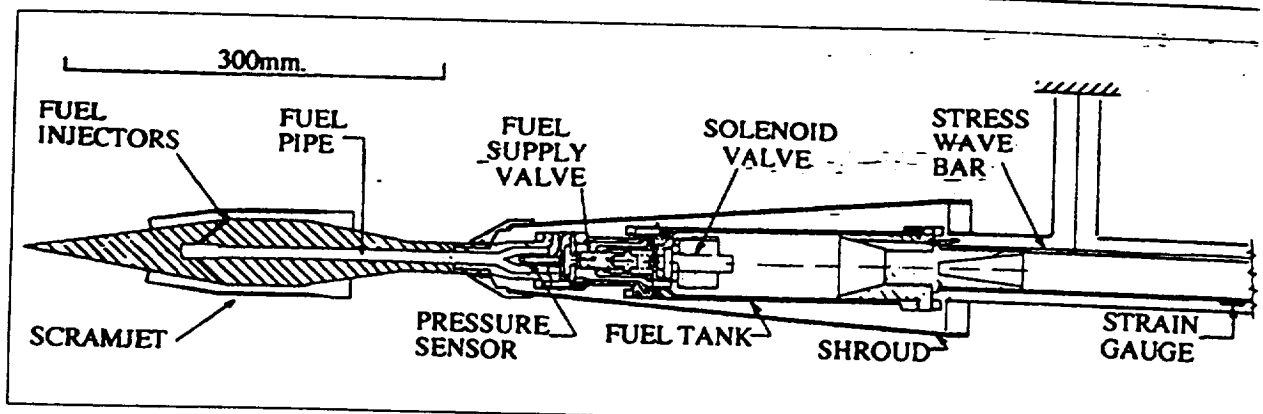


Figure 1. Scramjet model and fuel tank assembly.

strain gauge was mounted some 250 mm from the junction. The stress bar was free at the downstream end and was suspended by wires, which did not influence the propagation of stress waves.

The relation between the force input $u(t)$ and the strain gauge output $y(t)$ can be written by using the impulse response $g(t)$ relating the two, as

$$y(t) = \int_0^t g(t-\tau)u(\tau)d\tau$$

Dynamic finite element computer simulations showed that the sum of the forces distributed along the length of the model could be accurately represented by a single force applied at the nose, so the required $g(t)$ was obtained experimentally by vertically suspending the model and stress wave bar by a fine wire from the tip of the forebody, and suddenly severing the wire. The resulting strain gauge response was then differentiated with respect to time to find $g(t)$. It was necessary to establish $g(t)$ for a period of several milliseconds, in order to accommodate the generation of thrust by fuel injection before the initiation of the test flow. As the stress wave bar was only 2 m long, and was made of brass, this implied that the impulse response included stress wave reflections in the bar.

A computer program was prepared to deconvolute the above integral with this $g(t)$ and applied to yield the axial force for each test.

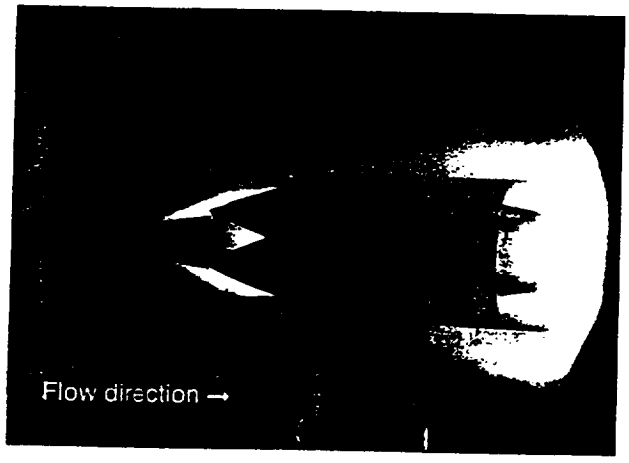


Figure 2. A time integrated photograph of the scramjet during a test with stagnation enthalpy of 3·0 MJ/kg, freestream Mach number, pressure and temperature of 6·6, 9 kPa and 300K, respectively, and a fuel of 13% silane and 87% hydrogen by volume.

EXPERIMENTS AND RESULTS

The experiments were conducted with a fuel consisting of 13% silane (SiH_4) and 87% hydrogen by volume, yielding typical results as displayed in Fig. 3[4]. Figure 3(a) displays the Pitot pressure and static pressure of the freestream measured during a test, showing that the flow reaches an approximately quasi-steady state about 0·5 ms after first arrival at the test section, and that state subsequently persists for approximately 1 ms. Records of the axial force experienced by the scramjet are displayed in Fig. 3(b). It can be seen that with no fuel injection, the scramjet experiences a drag force of 140 ± 25 N. When nitrogen is used as the test gas, and fuel is added, the drag on the scramjet is reduced substantial-

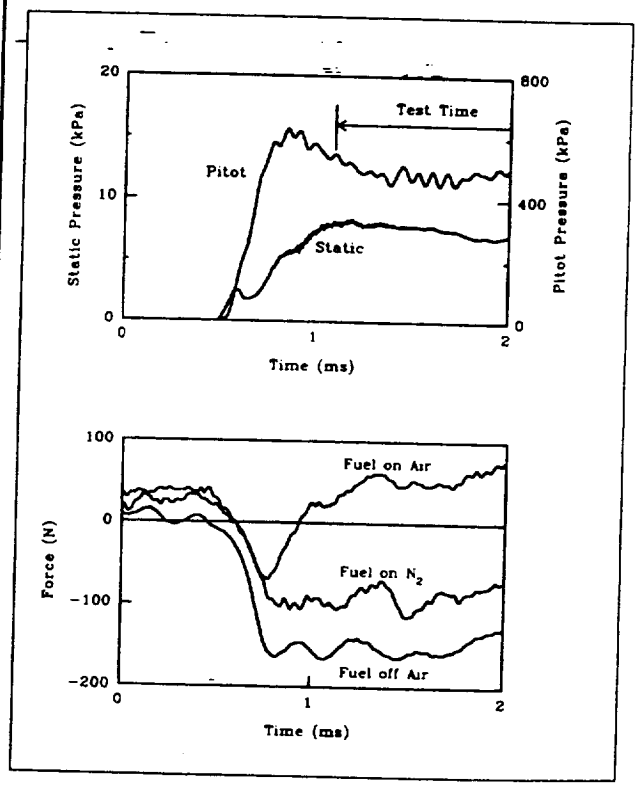


Figure 3. Test records showing generation of net thrust (stagnation enthalpy = 3·2 MJ/kg, fuel/air equivalence ratio = 0·90).

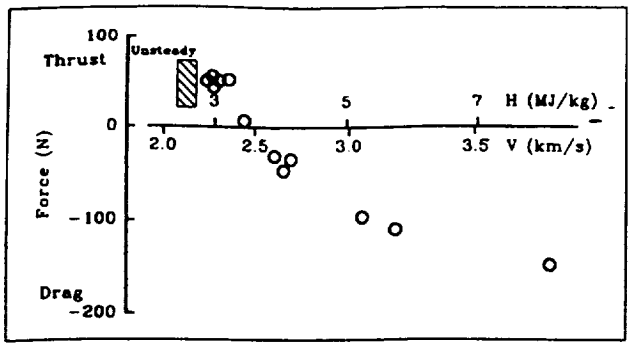


Figure. 4 Measured axial force on scramjet model with fuel injection (H = stagnation enthalpy, V = test section velocity, fuel 87% H_2 13% SiH_4, equivalence ratio = 0·83 ± 0·07, Mach number = 6·6 to 5·6).

ly. The test conditions with nitrogen differ only slightly from those with air, so most of the difference is attributed to the thrust due to fuel injection alone. When the fuel is injected into air, it can be seen that, prior to arrival of the test flow, the fuel produces a thrust of approximately 40 N, and as the flow about the model establishes itself the drag increases, closely following the nitrogen result. However, once air flow through the combustion chambers allows ignition of the fuel, the thrust due to combustion increases until, during the test time, it is sufficient to produce a net thrust on the scramjet of more than 50 N.

The variation of the thrust with tunnel stagnation enthalpy, or with the computed test section velocity[5], is shown in Fig. 4. It can be seen that although the net thrust is positive around stagnation enthalpies of 3 MJ/kg, it falls off rapidly with increasing stagnation enthalpy. This is due to an increasing pre-combustion temperature in the combustion chamber. An attempt was made to increase the maximum thrust measured by either increasing the amount of fuel injected, or by lowering the tunnel stagnation enthalpy. In both cases unsteadiness in the flow resulted, suggesting the onset of thermal choking.

To confirm that the flow in the combustors was supersonic when combustion was taking place, Pitot and static pressures were measured at the downstream end of one of the ducts just upstream of the expansion caused by the upstream corner of the afterbody. At the stagnation enthalpy of 3·3 MJ/kg, the ratio of the two was 4·1, yielding a Mach number of 1·75 + 0·1.

The performance of the scramjet configuration tested was not impressive, as the maximum observed net thrust of 60 N corresponded to a fuel specific impulse of only 200 s. However, no serious attempt was made to optimise the configuration for net thrust, as is witnessed by a fuel-off drag co-efficient of 0·13 at a stagnation enthalpy of 3 MJ/kg. Substantial improvements may be expected from proper attention to aerodynamic design.

ACKNOWLEDGMENT

The authors would like to express their appreciation of the support provided by the Australian Research Council, and through NASA grant NAGW-674.

REFERENCES

1. SANDERSON, S.R. and SIMMONS, J.M. Drag Balance for Hypervelocity Impulse Facilities. *AIAA J*, Dec 1991, 29, pp 2185-2191.
2. SIMMONS, J.M., DANIEL, W.D., MEE, D.J., and TUTTLE, S.L. Force Measurement in Hypervelocity Impulse Facilities, In: *New Trends in Instrumentation for Hypersonic Research* (Ed. BOUTIER, A.), Kluwer Academic Publishers, Amsterdam, 1993, pp 285-294.
3. PORTER, L.M., MEE, D.J., and SIMMONS, J.M. Measuring the Effect on Drag Produced by Nose Bluntness on a Cone in Hypervelocity Flow, In: Proc. 11th Australasian Fluid Mechanics Conference (Eds DAVIS, M. and WALKER, G.), University of Tasmania, Hobart, Australia, 14-18 December, 1992, pp 287-290.
4. PAULL, A., STALKER, R.J. and MEE, D.J. Thrust Measurements of a Complete Axisymmetric Scramjet in an Impulse Facility, AIAA paper no. 93-5168. AIAA/DGLR Fifth International Aerospace Planes and Hypersonics Technologies Conference, Munich, Germany, 30 Nov-3 Dec 1993.
5. LORDI, J.A., MATES, R.E. and MOSELLE, J.R. Computer Program for Numerical Solution of Non-equilibrium Expansion of Reacting Gas Mixtures, NASA CR-472, 1966.

SUPERSONIC COMBUSTION RAMJET PROPULSION EXPERIMENTS IN A SHOCK TUNNEL

A. Paull, R.J. Stalker and D.J. Mee

Department of Mechanical Engineering

The University of Queensland

Brisbane, 4072 Queensland Australia

ABSTRACT

Measurements have been made of the propulsive effect of supersonic combustion ramjets incorporated into a simple axisymmetric model in a free piston shock tunnel. The nominal Mach number was 6, and the stagnation enthalpy varied from 2.8 MJ kg^{-1} to 8.5 MJ kg^{-1}. A mixture of 13% silane and 87% hydrogen was used as fuel, and experiments were conducted at equivalence ratios up to approximately 0.8. The measurements involved the axial force on the model, and were made using a stress wave force balance, which is a recently developed technique for measuring forces in shock tunnels. A net thrust was experienced up to a stagnation enthalpy of 3.7 MJ kg^{-1}, but as the stagnation enthalpy increased, an increasing net drag was recorded. Pitot and static pressure measurements showed that the combustion was supersonic.

The results were found to compare satisfactorily with predictions based on established theoretical models, used with some simplifying approximations. The rapid reduction of net thrust with increasing stagnation enthalpy was seen to arise from increasing precombustion temperature, showing the need to control this variable if thrust

performance was to be maintained over a range of stagnation enthalpies. Both the inviscid and viscous drag were seen to be relatively insensitive to stagnation enthalpy, with the combustion chambers making a particularly significant contribution to drag. The maximum fuel specific impulse achieved in the experiments was only 175 sec., but the theory indicates that there is considerable scope for improvement on this through aerodynamic design.

1. INTRODUCTION

The supersonic combustion ramjet, or "scramjet", has existed as a concept for some decades (e.g. Ferri 1964, Swithenbank 1967, Jones and Huber 1978, Billig 1993). Essentially, it generates a propulsive effect through heat addition, by combustion, at supersonic speeds. In principle, it is able to operate at any flight speed, but a practical limit seems to exist at 4 or 5 km s^{-1}. To explore the potential of the scramjet, the ability to conduct routine experimentation at such speeds is essential.

For speeds in excess of 2 km s^{-1}, power and materials limitations have forced ground facilities to adopt the principle of impulse operation, with test times of only a few milliseconds. The most successful facility of this type has proven to be the shock tunnel, and indeed, substantial scramjet experimentation has been done in shock tunnels (e.g. Stalker and Morgan 1984).

However, the scramjet is a propulsive device, and the ultimate test of a propulsive device is its ability to generate thrust when installed in a flight vehicle. Therefore experimentation in which thrust or drag is measured on vehicle models in a shock tunnel

can be expected to be an important part of scramjet research.,

Methods of measuring forces on a shock tunnel model have been reported by previous investigators (Bernstein 1982, Jessen and Grönig, 1989, Naumann et al 1993), but these are only effective with test models which are relatively small with respect to the tunnel size. For a scramjet model to produce thrust, vigorous combustion in the combustion chambers is required and, with the combinations of pressure and Mach number which can be achieved in a shock tunnel, a not insubstantial length is required for the combustion chambers. Since the combustion chambers must be integrated into a complete model it is, therefore, very difficult to retain a model size which is small in relation to the tunnel size.

This paper reports measurements of the effect of stagnation enthalpy on the thrust and drag of a quasi-axisymmetric scramjet model. It is of particular relevance to the possible use of scramjets to propel acceleration vehicles, where one of the effects of the continually changing flight velocity will be a changing stagnation enthalpy. The model incorporated intakes, combustion chambers and thrust nozzles, and was therefore aerodynamically complete. Having regard to the difficulty noted in the previous paragraph, the measurements were accomplished by employing a stress wave force balance (Sanderson and Simmons 1991), which will be explained in more detail below, and which does not require a model which is small in relation to the tunnel size. A positive resultant thrust was measured - i.e. the total thrust generated was greater than the drag of the complete configuration - though only over a limited range of test section velocities.

The measurements are also compared with theoretical predictions. Though intakes, combustion chambers and thrust nozzles have all been the subject of research separately, an experimental study involving all three elements combined into an integrated configuration has not been reported, at least, in the open literature. Therefore the comparison between theory and experiment is of considerable interest. The model was designed to facilitate this comparison, and so an outstanding propulsive performance was neither expected nor achieved.

The shock tunnel in which the experiments were conducted is briefly described first, paying attention to limits on the test time and the test section flow produced. Then the main features of the model are described, followed by a short discussion of the principle of the stress wave force balance. The application of the balance to this problem is outlined, and some typical data recordings are presented. Following this, theoretical predictions of the effect of stagnation enthalpy on the thrust are developed. These predictions are then compared with measurements of the thrust, the comparison being assisted by some pressure measurements in one of the combustion ducts of the model.

2. THE SHOCK TUNNEL

The experiments were done in the free piston shock tunnel T4 at The University of Queensland, as shown in fig. 1. This consisted of a compression tube, 27 m long and 228 mm in diameter, in which the temperature and pressure of the driver gas was raised by a free piston compression process immediately prior to diaphragm rupture. The shock tube was 10 m long and 76 mm in diameter, and for these tests, supplied test gas to a contoured hypersonic nozzle which expanded from a throat diameter of 25 mm to a

diameter of 263 mm at the test section.

The nozzle stagnation pressure was monitored during each test by a PCB quartz piezoelectric pressure transducer located 60 mm upstream of the downstream end of the shock tube, and a typical record is shown in fig. 2(a). It can be seen that after the initial peak at shock reflection, the pressure remained constant within 20% for approximately 2 millisec. A mixture of Argon with Helium was used as the driver gas, and the ratio of the two was varied as the stagnation enthalpy was varied to ensure that a similar period of approximately constant nozzle stagnation pressure was maintained throughout the tests.

Measurements with a time-of-flight mass spectrometer on the nozzle axis were used to determine when the test section become contaminated by driver gas, and results are shown in fig. 2(b)*. It can be seen that, although the time to contamination exhibits substantial shot to shot variation at a given stagnation enthalpy, a period of 1 millisecond or more of flow with a contamination level of less than 10% exists up to stagnation enthalpies of 10 MJ kg^{-1}. This is in excess of the stagnation enthalpies used in the experiments.

The test section conditions were calculated using a non-equilibrium nozzle code (Lordi et al 1966) for a steady expansion in a hypersonic nozzle from known reservoir conditions to a given Pitot pressure level. The reservoir conditions were determined by first obtaining the pressure and stagnation enthalpy after shock reflection from measurements of the shock speed and shock tube filling pressure. It is then assumed that an isentropic

*The authors would like to thank K. Skinner for the use of this data.

expansion to the measured nozzle reservoir pressure occurs. This pressure varied from 34 MPa to 40 MPa, with an underlying trend to increase with increasing stagnation enthalpy superimposed on a random shot to shot variation. This is reflected in the Pitot pressure measurements shown in fig. 3(a). The ratio of Pitot pressure to nozzle reservoir pressure was $(14.1 \pm 0.6) \times 10^{-3}$, and showed no variation with stagnation enthalpy so the scatter in Pitot pressure is due largely to variation in nozzle reservoir pressure. Using the value of 14.1×10^{-3} for the nozzle calculations, the test section conditions shown in fig. 3(b) were obtained.

The test section flow was calibrated for uniformity and flow divergence by traversing with a Pitot rake. A typical result is shown in fig. 4.**. Two traverses, taken at 100 mm and 300 mm from the nozzle exit respectively, are shown in the upper half of the figure. The position of the model is shown in the lower half. The cone of uniform flow starts well upstream of the model, and the traverses show that a reasonably uniform test core, without observable flow divergence, persists to a distance well downstream of the model. The location of a Pitot probe, which was used to monitor the Pitot pressure during tests on the model, is also shown in the bottom half of the figure and yielded the results of fig 3(a).

3. THE MODEL

The scramjet model is shown in fig. 5 with half of the cowl removed. It consists of an axisymmetric centrebody, with six combustion chambers and associated intakes symmetrically arranged about its periphery, and separated from each other by six

**The authors would like to thank S. Overton for the use of this data.

splitters. The centrebody has a conical forebody with an 9° half angle, and a conical afterbody of 10° half angle. The combustion chamber intakes consist of compression ramps formed by the splitters which deflect the flow in the shock layer on the conical forebody through an angle of 8° parallel to its surface, with the leading edge of the cowl swept at an angle chosen to trap the nearly two-dimensional shocks so formed, and prevent them spilling into the freestream. The internal surface of the cowl is parallel to the forebody surface, and the external chamfer on the cowl leading edges makes an included angle of 8.5° in the freestream direction. The leading edge of the compression ramps is 10 mm wide, measured in the radial direction.

After the flow in the forebody shock layer has passed through the shock formed by one of the compression ramps, and its reflection, it is then turned to become parallel to the freestream, and enters one of the combustion chambers. These are 59 mm long, and each has a cross-section which is an arc of an annulus of major diameter 67 mm and minor diameter 51 mm, subtending an angle of 23° at the centreline. The fuel injection orifices were located at the beginning of the cylindrical part of the centrebody, and were therefore at the upstream end of the combustion chambers. There was one orifice to each combustion chamber. They were 2 mm in diameter, angled at 30° to the centreline, and injected in the downstream direction.

At the downstream end of the combustion chambers, the sidewalls deflect through an angle of 12°, and the conical afterbody begins, to make an array of thrust generating surfaces. These are terminated when the 12° surfaces meet, and when the afterbody diameter becomes 25 mm, at which point the centrebody becomes cylindrical again. The

trailing edge of the cowl also makes an internal angle of 7° with the freestream direction, and this is expected to add a small increment of thrust.

The model as it is mounted in the test section is shown in fig. 6 . The model is attached via the valve system to the fuel tank, which is itself attached to the stress wave bar of the stress wave balance. The stress wave bar is suspended from ports in the tunnel dump tank by two fine wires. The valve assembly, the fuel tank and the stress wave bar are surrounded by an aerodynamic shroud, and the only contact of the model assembly with the shroud is through a flexible "O" ring seal on the parallel section downstream of the conical afterbody of the model. A streamwise section of the model assembly is shown in fig. 6 . It can be seen that a 10 mm hole is drilled along the model axis to carry the fuel, which is distributed to the injectors as shown.

A schematic depicting the operation of the valve is shown in fig. 6 . The solenoid valve, S, is normally closed, and the fuel tank is filled before a test. The cavity G is maintained at the fuel pressure, so the fuel valve F is closed. When the tunnel is fired, its recoil closes a switch which activates the solenoid valve, causing it to open, and allow the fuel to flow out of cavity G to vacuum. The pressure in cavity G falls, the fuel valve F opens, and fuel flows through it to the fuel pipe. As it does so, its pressure is monitored by a PCB type 111A quartz piezoelectric pressure transducer. When the pulse of test gas has passed, the solenoid valve closes again, the fuel continues to flow into cavity G through the bleed orifice O, the pressure in the cavity builds up, and valve F closes.

The centrebody and splitters of the model are made of aluminium alloy, while the cowl

was made of stainless steel. The fuel tank and valve assembly is made of stainless steel.

4. THE STRESS WAVE FORCE BALANCE

It will be observed that the length of the model is not small with respect to the tunnel size. Also it is noted by Sanderson & Simmons (1991) that stress waves, induced in the model by the flow starting process, propagate along the model with speeds of the order of 3000 to 5000 m s^{-1}, which is of the same magnitude as the flow speed. Therefore, the many stress wave reflections which must occur before the model can be said to behave as a rigid one will correspond to a large number of flow passes over the model, requiring a time which normally exceeds the test time.

Fortunately, the stress waves which are the source of this difficulty can themselves be exploited to measure the force on the model. If strain gauges are placed on the model support sting adjacent to the base of the model, and the time history of stress waves passing into the sting is recorded, this recording can be deconvoluted to yield the force on the model. The simplest case of deconvolution occurs when the model is simply an extension of the stress bar and the force is applied as a step change in time at its upstream end, in which case the strain gauges record the passage of a stress wave which directly represents the applied load. This, in fact, is identical to the bar gauge which is used for measuring transient pressures. However as the models become more complicated, so does the deconvolution.

When Sanderson and Simmons first proposed this technique, they applied it to measurement of drag on a short cone. In that case the internal stress wave effects were

unimportant, but subsequent measurements on a 425 mm long cone, (Tuttle, 1990) where they were important, showed that they could be taken into account satisfactorily. Measurements on a long blunt cone (Porter, 1993) then showed that non-uniformity in the axial load distribution was no impediment to use of the method.

Now, for the purposes of stress wave analysis, the relatively slender models which are of interest here may be treated as one-dimensional, with cross-sectional area varying in the axial direction. Strictly, each axial element of the model produces a particular signal at the strain gauges, which therefore give an output which depends on the force distribution on the model, as well as the total force. Fortunately, numerical analysis (Simmons et al 1993), and the experiments noted in the previous paragraph, indicate that for these conical models and the times of interest here, the distribution of force is unimportant. When this is so, the relation between the output of the strain gauges, y(t), and the force applied to the model, u(t), may be written as

$$y(t) = \int_0^t g(t-\tau)\, u(\tau)\, d\tau ,$$

where g(t) is an impulse response function which relates y(t) and u(t). With g(t) determined, either numerically or by calibration, this expression allows numerical deconvolution procedures to be applied to y(t) to yield u(t).

The model employed here was larger and more complicated than the cones of the previous studies, so it was necessary to again check the distribution of force was not important. This was done numerically. A two-dimensional axisymmetric finite element 70 x 6 mesh was made to represent the model and fuel tank, and three loading

distributions were applied independently to approximately represent the loading on the model during a test. One represented the drag of the model, and was applied as a load distributed over the surface of the model. One represented the thrust due to injection of the fuel, and was applied as a point load at the location of the injection orifices. The third one represented the thrust due to mixing and combustion, and was applied as a distributed load on the thrust surface. The variation with time of each of these is shown in fig. 7(a). Together these three inputs produced a simulated strain gauge response. This was then deconvolved, using an impulse response function g(t) which was determined for a single point load applied at the nose, to see if the applied time history of the force on the model could be recovered. The result is shown as the solid line in fig. 7(b), where it is compared with the sum of the three forces acting on the model. It can be seen that the deconvolved signal is in good agreement with the input signal, signifying that the measured force was indeed independent of its distribution.

Having thus established that no significant error was involved in taking the force as applied at the nose, the impulse response function for such a force was determined experimentally. This was done by vertically suspending the model and fuel tank, attached to the stress bar, by a fine wire attached to the nose. The wire was cut close to the nose tip to effect a sudden removal of the tensile load, thereby producing the equivalent of a step increase in drag. The resulting strain gauge output shown in fig. 8(a), gave the step response for the system, and the impulse response was found by differentiating this with respect to time. This approach had the benefit that any effects of stress wave damping, though small, would be captured in the impulse response function. With a suitable g(t) thus defined in eqn (1), the deconvolution could then proceed numerically, by the time-

domain iterative method of Prost & Goutte (1984), to yield the axial force. This process yielded a random error of $\pm 10\%$ in the axial force, but no detectable systematic error.

5. FORCE MEASUREMENTS

A strain gauge output obtained during a test is shown in fig. 8(b). Fuel injection is timed so that a nearly constant fuel mass flow is maintained during the test time, and this has the consequence that the thrust due to fuel injection grows before the test time begins. This is evident in the lower frequency oscillation in the strain gauge output, before the initiation of test flow. As the test flow begins, the frequency increases.

Using the impulse response function derived from fig. 8(a), the output of the strain gauge in fig 8(b) is deconvolved numerical to yield axial force records, as shown in fig. 9(b). There are some spurious low amplitude oscillations on these records, which are ascribed partly to non-axial vibrations transmitted to the stress wave bar from the surroundings, and partly to imperfections in the deconvolution process, but these have only a small effect on the accuracy of the records. The test section Pitot pressure, as well as the fuel supply pressure for the fuel-on cases, are shown in fig. 9(a), and both are seen to be nearly constant during the test time.

It can be seen in fig. 9(b) that, for the fuel-off case, a drag of approximately 150 N is experienced by the model during the test time. When fuel is injected with nitrogen as the test gas, the drag is reduced and, before the test flow arrives, a thrust due to the reaction of the fuel jets is evident. This thrust increment appears to increase when the flow arrives but this is a spurious effect, due to the change in drag associated with the change

in test gas. When fuel is injected with air as the test gas, the axial force variation follows that of fuel injected into nitrogen, until the fuel ignites in the combustion chambers, when the axial force increases in the thrust direction, reaching a plateau at approximately 50 N of thrust.

Measurements of the axial force with and without fuel injection were taken for a range of stagnation enthalpies. However, before considering the results of these measurements, a theoretical treatment of the effects giving rise to this force is required, and this will be done after an analysis of the mode of metering the fuel injection.

6. FUEL INJECTION

Initially, it was intended that hydrogen be used as the fuel, as previous experiments (Stalker & Morgan, 1984) had suggested that at a combustion chamber length of 60 mm, and the pressures of approximately 1 atm, which it was thought would be achieved, would be adequate for combustion. However, hydrogen did not burn, due probably to the occurrence of expansion waves in the combustor, and a mode of fuel injection which was different to the original experiments. Therefore silane was added to the hydrogen to promote combustion.

A system for mixing silane and hydrogen was available, but required excessive time to produce a uniform mixture. Therefore the concentration of silane was monitored for each test by using the pressure transducer in the fuel supply duct and the pressure in the fuel tank, measured before and after a test, together with the following analysis.

Assuming the flow through the fuel injection orifices is sonic, the fuel mass flow rate at any instant may be written as

$$\dot{m}_F = \{F(\gamma) A_c / R_0 T\} \sqrt{M}\, P_F = B \sqrt{M}\, P_F$$

where $B = F(\gamma)\, A_c/R_0T$, $F(\gamma)$ is a function of the ratio of specific heats, A_c is the effective area of the orifices, R_0 is the universal gas constant, T is the temperature in the fuel injection system, which is taken as being constant, M is the molecular weight of the fuel, and P_F is the pressure measured in the fuel supply duct. From this, the mass Δm leaving the fuel tank in time t is

$$\Delta m = B \sqrt{M} \int_0^t P_F\, dt \quad .$$

Using the change in pressure in the fuel tank, ΔP_r, Δm may also be written as

$$\Delta m = M . \Delta P_r \; V / R_o T \quad ,$$

where V is the volume of the fuel tank. Equating the expressions for Δm leads to

$$M = \left\{ B (R_0 T / V) \int_0^t P_F\, dt / \Delta P_r \right\}^2 \quad .$$

The fuel supply valve opened in approximately 6 millisec, and closed approximately 100 millisec later. By monitoring P_F during this time, the value of the integral in the above equation could be obtained, and ΔP_r could be measured by observing the pressure in the fuel tank before and after a test. A previous calibration for B, obtained by operating the fuel system with various known amounts of silane in the gas mixture, then allowed M to be determined, and hence the silane concentration as well as the mass flow through the fuel orifices is also known. This was finally corrected for adiabatic expansion in the fuel tank by multiplying the mass flow by 1.08. The equivalence ratio was then calculated as the ratio of this mass flow to the mass flow of fuel required to consume all the oxygen in the air passing through the duct.

7. ANALYSIS OF PROPULSIVE PERFORMANCE

The installed propulsive perform ance of engines in an aerodynamic vehicle is commonly assessed in terms of the thrust generated versus the drag to be overcome. When the function of the engine is largely independent of the vehicle aerodynamics, it is possible to adopt a simple view, taking thrust as an engine property, and drag as a property of the vehicle. However, for scramjets, which are integrated into the flow field about the body, such an approach is not possible. In this case it is more suitable to relate the performance to fuel injection, estimating the change in axial force on the configuration produced by injecting the fuel.

Therefore the analysis proceeds by first considering the drag in the absence of fuel injection, before going on to treat the effect of the combustion of the fuel. It should be noted that, not withstanding the attempt to use a simple model configuration, the details of the flow are so complicated that a rigorous analysis would be extremely difficult. Thus, some simplifying approximations are made but, as will be seen below, the analysis which results adequately predicts the experimental results.

8. INVISCID FUEL-OFF DRAG

Intake Assembly. The flow over the conical forebody and the intakes is shown schematically in fig. 10. The conical shock originating at the tip of the cone causes a uniform pressure over the region a of the cone surface. The splitters are machined so that the inlet ramp surface is always normal to the cone surface, as shown in section AA. It is assumed that this leads to shocks which are also normal to the cone surface, and that the pressure in the regions b is uniform and is given by the pressure downstream of a

two-dimensional oblique shock formed by the leading edge of the inlet ramp. The effect of shock-boundary layer interactions is ignored, since they do not affect the overall pressure rise, and the dispersion of the pressure rise at the foot of the shock which they do cause is likely to raise the force on the surface upstream of the shock by as much as it reduces it downstream. As shown in section AA, the outer surface area of the inlet duct is greater than the inner area, and this effect is taken into account.

Calculations indicate that the conical shock from the tip of the cone should pass inside the cowl, as shown in figure 10(a). Further calculations showed that if it passed outside of the cowl, the leading edge bevel would induce shock detachment. Detachment was not evident in luminosity photographs of the flow, and so the drag could be estimated by taking the free stream to be directly incident on the exterior surfaces of the cowl. The pressure on the bevel was obtained by treating it as part of an infinite, swept, leading edge.

The maximum temperature in the inlet was less than 2200 K, implying that no dissociation took place. Thus the flow model outlined was used, with a ratio of specific heats of 1.4. The inviscid drag of the intake assembly, comprising the conical forebody, the inlets and the cowl exterior, expressed in Newtons, was calculated to be

$$25 \times 10^{-5} P_p$$

with the Pitot pressure P_p in units of N m^{-2}. This was independent of the expected variation in the freestream Mach number. The major contributions were the drag on the inlet ramps, or splitters, at 50%, the drag on the forecone, at 20%, and the drag on the cowl leading edge bevel, at 25%.

Combustion Chambers. The inviscid drag of the combustion chambers is zero, since their cross-sectional area is constant. However, the pressure and Mach number in the combustion chambers is required in order to calculate the level of thrust produced in the expansion nozzle. These may be obtained from the relations for adiabatic flow in a streamtube (e.g. Hall 1951) which can be written as

$$\frac{A_f}{A_\infty} \exp(-\Delta S/R) = \frac{M_\infty}{M_f}\left(\frac{1+\frac{\gamma-1}{2}M_f^2}{1+\frac{\gamma-1}{2}M_\infty^2}\right)^{(\gamma+1)/2(\gamma-1)},$$

and

$$\frac{P_f}{P_\infty} = \frac{A_\infty}{A_f}\frac{M_\infty}{M_f}\left(\frac{1+\frac{\gamma-1}{2}M_\infty^2}{1+\frac{\gamma-1}{2}M_f^2}\right)^{1/2},$$

where A_∞ is the cross-sectional area in the freestream of the streamtube captured by the intake, M_∞ and P_∞ are the freestream Mach number and pressure, A_f is the total cross-sectional area of the combustion chambers, and M_f and P_f are the Mach number and pressure there. Since the conical shock from the cone passes inside the cowl leading edges, no "spilling" of the flow from the intake takes place, and A_∞ can be taken as the area defined by the projection of the cowl leading edges onto a plane normal to the flow direction. The entropy rise per unit mass of gas associated with the three shocks through which the flow is compressed is ΔS, and R is the gas constant per unit mass. When these relations are combined with the dimensions of the model, it is found that, with $\gamma = 1.4$, $M_f = 4.0$ at $M_\infty = 6.1$ and increases by 10% for each 10% increase in M_∞. P_f may be written as

$$P_f = (0.56 - 0.059\, M_\infty)\, P_p \qquad (1)$$

which is a form convenient for later use. Estimates indicate that the effect of the displacement thickness of the boundary layer on the combustion chamber cross-section is

small enough to be ignored.

Predicted values of P_f are compared with measurements in fig. 15. The measurements are corrupted by the persistence of waves in the flow, due to intake-combustion chamber mismatch, but it can be seen that the predictions are not inconsistent with the mean level.

Expansion Nozzles. The surfaces of the expansion nozzles are formed by the conical afterbody and adjacent splitters, and the pressures experienced on these surfaces determine all but a few per cent of the thrust acting on the model. To calculate these pressures, it is assumed that the transverse curvature of the conical afterbody may be neglected, and the flow field at the corner between the afterbody and the splitters is that produced by double expansion of a streamwise corner, as shown in fig. 11.

The trace of the wave pattern in two cross flow planes, X and Y, is shown in the figure, demonstrating the conical nature of the flow. Taking the plane X, region f corresponds to uniform flow which is outside of the zone of influence of the two surfaces. Outside the zone of influence of the streamwise corner, the flow passes through one of two centred Prandtl-Meyer expansions to produce the two uniform flow regions f_1 and f_2. For the part of the flow field which is within the zone of influence of the streamwise corner, an analytic solution is not known, but numerical solutions (Anderson and Nangia 1977) indicate that each of the flow regions f_1 and f_2 passes through one of two further Prandtl-Meyer expansions to produce another region of uniform flow f_{12}. The total deflection angle experienced in passing from f to f_{12} is the same, irrespective of whether the passage is accomplished through f_1 or f_2. Since the properties of the flow produced by a Prandtl-

Meyer expansion are uniquely related to the deflection angle, the properties in f_{12} are uniquely determined. Thus the flow over each of the two adjacent surfaces can be analysed as a uniform flow, produced by the deflection of the surface itself, with the deflection of the adjacent surface producing a simple Prandtl-Meyer expansion of that uniform flow.

This model was used to obtain the pressure distribution on the conical afterbody and adjacent splitter surfaces, taking account of the expansion wave from the cowl trailing edge, and reflection from the plane of symmetry between two splitters, in the same way. A simple graphical procedure allowed the pressure distribution to be established with sufficient accuracy. The thrust was then obtained by integration of this pressure distribution, taking account of the reduction of area with downstream distance of the conical afterbody. The calculations were performed for a perfect gas with a ratio of specific heats of 1.4.

Results are presented in fig. 12 for a range of combustion chamber Mach numbers. For comparison, the thrust which would be obtained with one-dimensional flow through a nozzle of the same area ratio also is shown, and it is seen that the difference between the two increases with Mach number, the thrust of the three-dimensional nozzle falling as the one-dimensional one increases. Clearly, the three-dimensional flow makes better use of the thrust surfaces at lower Mach numbers than at the higher ones.

9. VISCOUS FUEL-OFF DRAG

To assess the viscous drag of a surface, it is first necessary to determine whether the

boundary layer is laminar or turbulent. Previous experiments (He and Morgan 1994) have shown that transition occurs on a flat plate in the shock tunnel at a Reynolds' number, based on distance from the leading edge, of approximately 2 x 10^6. Applying this to the model used in the experiments, the boundary layer flow on the inlet splitter face, the internal inlet, surfaces of the cowl, and the exterior surface of the cowl, along its full length, is expected to be laminar. The Reynolds' number on the conical forebody may reach 4 x 10^6 but, allowing for the higher transition Reynolds' numbers on a cone, this too is expected to exhibit predominantly laminar flow.

Thus for these surfaces, the local skin friction coefficient is given by (e.g. Hayes and Probstein 1959)

$$\begin{aligned} c_f &= 2\tau_w/\rho_e u_e^2 \\ &= 0.664\, n\left(\rho^* u^* / \rho_e \mu_e\right)^{0.5}/R_{ex}^{0.5} \end{aligned}$$

where ρ_e, u_e and μ_e are the density, velocity and coefficient of viscosity in the external stream adjacent to the boundary layer, τ_w is the skin friction per unit area, R_{ex} is the Reynold's number based on the external stream properties and the distance from the leading edge, n = 1 and $\sqrt{3}$ for a flat plate and a cone respectively, and ρ^* and μ^* are the density and viscosity at a reference temperature T^*, given by

$$T^*/T_e = 0.5\left(1 + T_w/T_e\right) + 0.0384\, M_e^2$$

where T_e and T_w are temperature in the external stream and at the wall respectively, and M_e is the external stream Mach number. Due to the reduction in Reynolds's number as the stagnation enthalpy increases, the skin friction increases with stagnation enthalpy, H_s, and the total drag, in Newtons, for the surfaces noted in the paragraph above is

$$(3.09 + 0.55\, H_s) \times 10^{-5}\, P_p$$

where H_s is in MJ/kg. Of this the forecone, the inlet splitter faces, the interior inlet surface of the cowl, and the exterior surface of the cowl all contributed approximately equal portions.

The Reynolds' number of the flow in the combustion chambers is such that, taking account of the shock-boundary interactions in the inlets, the boundary layer flow is expected to be turbulent. A review of turbulent skin friction by Hopkins and Inouye (1971) indicates that the theory of Spalding and Chi is most suited to the low values of T_w/T_e experienced here. This theory obtains the skin friction in compressible flow from incompressible values by using the transformations

$$\bar{c}_f = F_c\, c_f ,$$
$$\text{and } \bar{R}_{ex} = F_x\, R_{ex} ,$$

where the bar denotes the incompressible values. F_c and F_x are given here by

$$F_c = 0.18\, M_e^2\, (\sin^{-1}\alpha + \sin^{-1}\beta)^{-2} ,$$
$$\text{and } F_x = (\sin^{-1}\alpha + \sin^{-1}\beta)^2 \left\{0.18\, M_e^2\, (T_w/T_e)^{0.702}\ (T_w/T_{aw})^{0.772}\right\}^{-1}$$
$$\text{where } \alpha = (2A^2 - B)\,(4A^2 + B^2)^{-0.5} ,$$
$$\text{and } \beta = B(4A^2 + B^2)^{-0.5} ,$$
$$\text{with } A^2 = 0.18\, M_e^2\, T_e/T_w ,$$
$$\text{and } B = \left(1 + 0.18\, M_e^2 - T_w/T_e\right) T_e/T_w .$$

T_{aw} is the stagnation temperature in the external stream. The incompressible values of skin friction were taken from the relation

$$\bar{c}_f = 0.060\, \bar{R}_{ex}^{-0.2} .$$

The effective origin of the turbulent boundary layer was obtained by estimating the laminar boundary layer thickness at the entrance to the combustion chambers after

compression to the combustion chamber pressure, using this to indicate the effective origin of a laminar boundary layer, and assuming that the turbulent boundary layer originated at half that distance upstream. Using this theory, the skin friction drag in the combustion chambers, expressed in Newtons, was calculated to be

$$(35.1 + 0.82\ H_s) \times 10^{-5}\ P_f$$

where P_f is in units of N m^{-2}. There is negligible variation over the range of Mach numbers experienced without fuel injection.

The boundary layer flow in the expansion nozzles was also taken to be turbulent, as the favourable pressure associated with the expansion corner was estimated as insufficient to cause relaminarisation (Narasimha and Viswanath 1975). Noting that the skin friction coefficient varies slowly with Reynold's number it is assumed to be unchanged across the expansions and therefore, by also assuming that the velocity is unchanged, the skin friction at any point on the surface of the expansion nozzles can be obtained by knowing the local density in the inviscid flow. This can be derived from the pressure distribution on those surfaces. Integration over the surfaces then yields the drag due to skin friction on the expansion nozzles, in Newtons, as

$$4.8 \times 10^{5}\ P_f\ .$$

The skin friction on the part of the model support sting exposed to the flow was estimated to be negligible.

10. RESULTANT FUEL-OFF DRAG

Fig. 13 displays the results of the above calculations, with eq(1) used to relate P_f to P_p. Fig. 13(a) shows the inviscid drag, as the drag due to the intake and the cowl, minus the

thrust due to the expansion nozzle. Ideally, it should be possible to design a model such that one largely cancels the other, apart from a relatively small effect due to entropy rise in the intake, and to the reduction in expansion nozzle area ratio occasioned by the need to support the model on the sting. The fact that the residual drag is not small is largely due to two effects. The first is the drag due to the cowl leading edge bevel, which was incorporated solely for ease of manufacture of the model, and the second is the limited thrust performance of the expansion nozzle. This is due partly because it is operating at combustor flow Mach numbers about 4, which, as shown by fig.12, is considerably in excess of the optimum value, and this entails a considerable reduction in thrust. It is also due to the fact that even at lower Mach numbers, its thrust performance could be improved, as shown by the comparison with a one-dimensional nozzle in fig. 12.

Fig. 13(b) shows the viscous drag. It can be seen that the drag divides approximately evenly between the combustion chambers, where the boundary layer is turbulent, and the intake plus the cowl exterior surface, where the boundary layer is laminar. The expansion nozzle makes a small contribution only. The total viscous drag is comparable with the inviscid drag which, as already mentioned, can be substantially reduced by good design to leave viscous drag as the dominant contribution. This illustrates the point that successful operation of scramjet vehicles will be heavily dependent on control of these viscous losses.

The inviscid drag and the viscous drag are combined to yield the resultant drag in fig. 13(c), where it is compared with measurements. The possible error in the measurements is about equally due to uncertainty in the measured drag and uncertainty in the measured

Pitot pressure. Within the limits of error, it is clear that theory and experiment agree, except for a tendency for the drag to increase somewhat more rapidly with stagnation enthalpy than is indicated by the theory. This could be due to the theoretical model used for turbulent skin friction.

11. INVISCID FUEL-ON THRUST

Combustion chamber pressure rise. The propulsive effect of a scramjet derives from the pressure rise experienced in the combustion chambers due to mixing and burning of the fuel there. If either, or both, of these processes are not completed in the combustion chamber the pressure rise is reduced, and therefore so is the thrust.

Shock tube data (Jackimowski & McLain 1983) indicates that, regardless of the presence of silane, the fuel should not burn in the combustion chambers. However shock tunnel experiments (Morris 1988) exhibit much shorter reaction lengths, due possibly to high boundary layer temperatures and "frozen" oxygen radicals in the freestream. Under the conditions of the present tests, reaction lengths of the order of 10 mm are likely, and as this is much less than the length of the combustion chambers it is assumed that complete combustion of all the fuel that is mixed takes place.

An indication that essentially complete mixing occurred was obtained by plotting the thrust obtained against the fuel equivalence ratio, as in fig. 14(a). It can be seen that the thrust varied approximately as the fuel mass flow, suggesting that the proportion of fuel burnt was approximately independent of the mass flow. Since the proportion of a fuel jet which is mixed in the length of combustion chamber will only be invariant with the jet

mass flow if all of the jet is mixed, it is reasonable to assume that complete mixing occurred.

Thus, an analysis was conducted of pre-mixed, equilibrium combustion in a constant area duct of the silane-hydrogen fuel. It was assumed that the silane burned according to the reaction

$$SiH_4 + 2O_2 \rightarrow SiO_2 + 2H_2O \ ,$$

and the hydrogen according to the reaction

$$2H_2 + O_2 \rightarrow 2H_2O \ .$$

Dissociation of H_2O in the combustion products was taken into account (e.g. Beniot 1968) and, since post combustion temperatures were above the condensation temperature of SiO_2, it was assumed to remain in the vapour state. The analysis was conducted in a conventional manner, using the energy equation, with the heats of formation included in the enthalpy, together with the momentum equation and the equation of state, applied across a shock-like discontinuity. The change in molecular weight due to addition of the fuel, and due to its chemical reaction with air, were taken into account. For each set of precombustion conditions, a solution was obtained iteratively, yielding the results shown in fig. 14(b). They show that the combustion heat release has a reducing effect as the stagnation enthalpy, and therefore the pre-combustion temperature, is increased. The combustion pressure rise is reduced, and the post-combustion Mach number increases, to come closer to pre-combustion values. A curve for the temperature ratio across the combustion zone is also presented, showing that the pressure rise is almost entirely due to the combustion temperature rise.

The effect of dissociation of H_2O in the combustion products on the temperature rise increased with stagnation enthalpy, reducing T_c by 6% at 3 MJ kg^{-1}, and 25% at 8.5 MJ kg^{-1}. Thus, at the higher stagnation enthalpy, dissociation reduced P_c/P_f from 1.5 to 1.2, which is not a large effect when compared with that of pre-combustion temperature. Hence, for the conditions of this paper, dissociation is not considered to be important.

The effect of combustion was measured by making a series of pressure tappings in one of the combustion chambers, as shown in fig. 15. Although the non-uniformity of the flow makes an exact comparison with the theory impossible, it can be seen that if the average of the two downstream data points is taken, the pressure level is predicted reasonably well. The upstream data points may be taken to indicate that mixing and/or combustion is not complete at those stations. As shown, Pitot pressure was also measured at a point which was just upstream of the expansion wave from the corner of the centrebody. Taking the mean of the static pressure at the two downstream stations when combustion occurred, and the ratio of specific heats for the combustion products, and combining these with the Pitot pressure, it was possible to obtain the Mach number of the flow after combustion. This varied from 1.5 to 2.2 as the stagnation enthalpy increased from 3.2 MJ kg^{-1} to 5.8 MJ kg^{-1}, signifying that supersonic combustion had indeed taken place.

Expansion Nozzles. The thrust due to the expansion nozzles is obtained as before with P_c replacing P_f as the pressure before expansion. The frozen ratio of specific heats for the combustion products differed from 1.4 by only 3%, so fig. 12 could be used again to predict the thrust. However, it should be noted that combustion reduces the Mach

number at the entrance to the nozzles, an effect which was taken into account by using the theoretically calculated Mach numbers presented in fig. 14.

Fuel Injection Thrust. There is a substantial amount of thrust associated with fuel injection, and to take account of this it was noted that the fuel supply duct pressure, P_F, was an order of magnitude greater than the pre-combustion pressures in the combustion chambers. Thus it was assumed that after injection, the fuel expanded to very low pressures. The velocity of the fuel could thus be obtained as $\sqrt{2/(\gamma-1)}\ a_F$, where a_F is the speed of sound in the fuel before injection, and by combining this with the fuel mass flow, and allowing for the injection angle, the thrust could be determined. A discharge coefficient of 0.9 was used for the fuel orifices, and for fuel mass flows corresponding to an equivalence ratio of 0.77, the thrust in Newtons was

$$(60 - 4.2\ H_J) \times 10^{-5}\ P_f.$$

where eq(1) can again be used to express P_f in terms of P_p. While this was not inconsistent with measurements of thrust before the test flow arrived, as seen in fig. 9, the accuracy of those measurements prevented a more definitive comparison.

The results of these calculations are presented in fig. 16(a), for an equivalence ratio corresponding to the mean value used in the experiments. The inviscid drag of the intake and cowl remains as before, but the pressure rise due to combustion allows the expansion nozzle to produce much greater thrust. When this is added to the fuel injection thrust it is sufficient to outweigh the inviscid drag over most of the range of enthalpies studied.

12. VISCOUS FUEL-ON DRAG

The injection of fuel does not, of course, influence the skin friction drag on the intake and cowl, but it does affect the skin friction in the combustion chambers and the expansion nozzles, through the effect of combustion on the temperature of the flow external to the boundary layer. The theory of Spalding and Chi is used once again to yield

$$(70 - 3.0\ H_J) \times 10^5\ P_f$$

for the skin friction drag, in Newtons, on the combustion chambers under the calculated flow conditions. The skin friction drag on the expansion nozzles is also estimated according to the same approximation as in the fuel-off case, to yield, in Newtons,

$$6.3 \times 10^5\ P_f\ .$$

These results are presented in fig.16(b) in terms of P_p. Comparison with fig. 13(b) reveals that the major change in skin friction drag associated with fuel injection is the increase in drag of the combustion chambers. This amounts to a 90% increase at a stagnation enthalpy of 3 MJ kg^{-1}, where the combustion has the largest proportional effect on the temperature. However, at 8 MJ kg^{-1}, where the proportional increase in temperature is greatly reduced, the increase in combustion chamber skin friction is only 14%.

The skin friction in the expansion nozzles is also increased, but this is such a small contribution to the overall skin friction drag that the magnitude of the increase can barely be noticed on the scale of fig. 16(b).

13. RESULTANT FUEL-ON AXIAL FORCE

The curves in fig. 16 for total inviscid axial force, and total viscous drag, are combined into one curve for the resultant axial force in fig. 17. In order to finally emphasise the propulsive performance, the curve is presented with thrust as the positive ordinate. Measurements of thrust are also presented, for fuel equivalence ratios near the value used in the theoretical calculations, and are seen to follow the theoretical predictions reasonably closely, with a tendency to fall below the theoretical curve at the higher values of stagnation enthalpy. This follows the same trend as for the fuel-off case, and to facilitate the comparison, the resultant drag curve and the measurements of fig. 13(c) are presented again in fig. 17. It seems likely that the cause of the discrepancy is the same in both areas.

It will be noted that the maximum thrust is obtained at the lowest stagnation enthalpy. Attempts to increase the maximum value achieved, either by lowering the stagnation enthalpy or by increasing the fuel equivalence ratio, produced unsteadiness in the force measurement and then "choking" of the flow through the model. In view of the low value ($\sim$ 1.5) measured for the post combustion Mach number at a stagnation enthalpy of 3.2 MJ kg^{-1}, it seems reasonable to conclude that this was due to thermal choking of the flow in the combustion chambers.

The propulsive performance of the model used in these experiments was not outstanding. For example, if the maximum value of thrust obtained is taken as $10 \times 10^{-5} P_p$ Newtons, the corresponding specific impulse is 175 sec. If the silane in the fuel were replaced by an amount of hydrogen sufficient to consume the same amount of oxygen, and the same

thrust were obtained, the fuel specific impulse would be 370 sec. However, it is worthwhile reiterating that the model was designed for ease of manufacture and analysis, and not for optimum performance.

Inspection of figs. 13 and 16 suggest ways in which the performance might be improved. Fig. 13(a) indicates that the inviscid drag of the configuration could be reduced; for example, by removing the external bevel on the cowl leading edges. The thrust delivered by the expansion nozzles could be improved by better design, although it must be remembered that combustion lowers the Mach number of the flow entering the expansion nozzles, and as shown in fig. 12 this improves the efficiency of the nozzles. Also expansion nozzles of larger area ratio would deliver more thrust, though provision of a larger expansion area ratio would impact other aspects of the overall design.

The viscous drag, as shown in figs. 13(b) and 16(b), represents a substantial portion of the overall drag, and one which offers less opportunity for reduction. However, there is a clear benefit in this respect in reducing the length of the combustion chambers, provided this can be done without reducing the benefits of combustion.

The relatively large size of the viscous drag points to one of the major difficulties associated with air breathing propulsion at very high speeds. It is likely to be an intractable form of drag, difficult to design against, and its importance here confirms the widely held view that it may be a major impediment to effective propulsion at such speeds.

Figs. 16 and 17 display the rapid decrease in net thrust which is occasioned by increasing stagnation enthalpy. This is, of course, due to the increasing combustor temperature before combustion, which reduces the combustion pressure rise. For application to an acceleration vehicle, a scramjet must operate near its optimum over a range of stagnation enthalpies, and therefore a means of maintaining the temperature before combustion reasonably constant would need to be found.

14. CONCLUSION

Thrust and drag measurements have been made in a shock tunnel on a supersonic combustion ramjet model. The effect of stagnation enthalpy on the propulsive performance of the model was measured for a range of stagnation enthalpies corresponding to flight velocities up to approximately 4 km/sec. A stress wave force balance was used, which involved monitoring the stress waves produced by the forces on this model as they passed into the model sting support. This, in combination with a pulsed fuel injection system, made the measurements possible.

The results were compared with theoretical predictions, and were found to be in generally good agreement, with a tendency to slightly underestimate the drag at high enthalpies. The analysis leading to the predictions involved the use of established theories which, together with some reasonable simplifying assumptions, provided estimates of the relative importance of the factors affecting the thrust and drag. Except for the combustion process itself, the analysis assumed a perfect gas with a ratio of specific heats of 1.4.

The experimental validation of this relatively simple theoretical analysis may be expected

to have a number of consequences. As well as indicating the significance of factors such as expansion nozzle performance and skin friction drag, it allows the benefits of concepts for improving the propulsive performance to be quantified, and thereby assists in improving the performance. Also, as with any flight vehicle, a simple analysis based on results of model experiments in a wind tunnel is useful for preliminary estimates of performance. Thus, with proper attention to factors such as the location of transition, estimates may be made of the performance of a scramjet powered vehicle in flight.

Using the theory, it was possible to identify areas where improvement may be expected to yield a gain in the overall thrust. For acceleration vehicles, it is clearly of primary importance that a means should be found of maintaining the precombustion temperature constant as the flight velocity changes. For cruise propulsion, this is less important. In general the inviscid drag of the configuration could be reduced by attention to design details and the performance of the expansion nozzles could be enhanced by matching them to the Mach number at which they are expected to operate. The theory also revealed the importance of viscous drag, and drew attention to the value of reducing viscous drag by reducing combustion chamber length.

However, perhaps the most important result is that the investigation has established a method for experimental testing of scramjet powered models at high velocities, together with the theoretical understanding which attends the approximate analysis. These two factors together may be expected to assist in the development of scramjet research.

ACKNOWLEDGMENTS

This work was supported by the Australian Research Council and by the National Aeronautics and Space Administration, U.S.A. under grant NAGW-674.

REFERENCES

Anderson, D.A. & Nangia, R.K. 1977 "Comparison of Numerical and Experimental "Conical" Flow Fields in Supersonic Corners with Compression and/or Expansion" Aeronautical Quarterly, 28, 293.

Benoit, A. 1968 "Equilibrium Thermodynamic Data for the H_2-O_2-He System" Univ. of Toronto, Institute for Aerospace Studies. Tech. Note. No. 128.

Bernstein, L. & Stott, G.T. 1982 "A Laser-Interferometer Method for Determining the Forces on a Freely Flying Model in a Shock Tunnel" Aero. Quarterly, 23, 237.

Billig, F.S. 1993 "Research on Supersonic Combustion" J. of Propulsion & Power, 9, 449.

Ferri, A. 1964. "Review of Problems in Application of Supersonic Combustion" J. of Royal Aero. Soc., 68, 575.

Hall. N.A. 1951 "Thermodynamics of Fluid Flow" pp. 112-114 New York: Prentice-Hall.

Hayes, W.D. & Probstein, R.F., 1959 "Hypersonic Flow Theory" p.296. New York: Academic Press.

He, Y. & Morgan, R.G. 1994 "Transition of Compressible High Enthalpy Boundary Layer Flow over a Flat Plate" The Aero. Journal, 98, 25.

Hopkins, E.J. & Inouye, M. 1971 "An Evaluation of Theories for Predicting Turbulent Skin Friction and Heat Transfer on Flat Plates at Supersonic and Hypersonic Mach Numbers" AIAA J. 9, 933.

Jackimowski, C.J. & McLain, A.G. 1983. "A Chemical Kinetic Mechanism for the Ignition of Silane/Hydrogen Mixtures" NASA TP2129.

Jessen, C. & Grönig, H. 1989 "A New Principle for a Short-Duration Six Component Balance" Experiments in Fluids, 8, 231.

Jones, R.A. & Huber, P.W. 1978 "Towards Scramjet Aircraft" Astronautics & Aeronautics, 16, 38.

Lordi, J.A., Mates, R.E. & Moselle, J.R. 1966 "Computer Program for Numerical Solution of Non-equilibrium Expansion of Reacting Gas Mixtures" NASA CR-472.

Morris, N.A. 1988 "Silane as an Ignition Aid in Scramjets" M.Eng.Sc. Thesis, Dept. of Mechanical Engineering, The Univ. of Queensland.

Narashima, R. & Viswandth, P.R. 1975 "Reverse Transition of an Expansion Corner in Supersonic Flow" AIAA J, 13, 693.

Naumann, K.W., Ende, H., Mathiew, G. and George, A. 1993 "Millisecond Aerodynamic Force Measurement with Side-Jet Model in the ISL Shock Tunnel" AIAA J. 31, 1068.

Porter, L.M., Paull, A., Mee, D.J. & Simmons, J.M. 1994 "Shock tunnel measurements of hypervelocity blunted cone drag" Accepted for publication AIAA J, April, 1994.

Prost, R. & Goutte, R. 1984 "Discrete constrained iterative deconvolution algorithms with optimised rate of convergence", Sig. Proc. 7, 209-230.

Sanderson, S.R. & Simmons, J.M. 1991 "Drag Balance for Hypervelocity Impulse Facilities, AIAA J. 29, 2185.

Simmons, J.M., Daniel, W.J., Mee, D.J. & Tuttle, S.L. 1993 "Force Measurement in

Hypervelocity Impulse Facilities" New Trends in Instrumentation for Hypersonic Research (ed A. Boutier) p.285. Kluwer Academic Publishers, Dordrecht.

Stalker, R.J. & Morgan, R.M. 1984 "Supersonic Hydrogen Combustion with a Short Thrust Nozzle" Combustion & Flame, 57, 55.

Swithenbank, J. 1967 "Hypersonic Air-breathing Propulsion" Progress in the Aeronautical Sciences, (ed. D. Küchemann). Pergamon, Oxford, 2, 229.

Tuttle, S.L. 1990 "A Drag Measurement Technique for Hypervelocity Impulse Facilities" M.Eng.Sc. thesis, Dept. of Mechanical Engineering, The Univ. of Queensland.

LIST OF FIGURES

Fig 1. Free Piston Shock Tunnel T4

Fig 2. Shock tunnel test time
(a) Typical nozzle reservoir pressure record, H_s = 7.7 MJ kg^{-1}
(b) Mass spectrometer measurement of driver gas contamination.
t_c = time after start of flow in test section until 10% driver gas contamination
H_s = stagnation enthalpy.

Fig 3. Test Section Flow Conditions
(a) Measured Pitot pressure
(b) Calculated Conditions.
P_p = Pitot pressure, M_∞ = Mach number, T_∞ = static temperature, u_∞ = velocity.

Fig 4. Test Section Flow Calibration and Location of Model. Stagnation enthalpy = 8 MJ kg^{-1}
• Pitot survey measurements
d = downstream distance from nozzle exit, r = distance from centreline.

Fig 5. The Scramjet Model

Fig 6. Model, Fuel Supply System and Model Mount.

Fig 7. Simulation of Distributed Load
(a) Input loads. —— fuel injection ——— Drag ------- Thrust.
(b) Output. ——— deconvolved load ----- true input.

Fig 8. Strain Gauge Outputs
(a) Response to step load
(b) Response during test.

Fig 9. Axial Force Measurements. Stagnation enthalpy = 3.2 MJ kg^{-1}, Fuel-on Air equivalence ratio = 0.83
(a) Test flow and fuel monitoring
(b) Force on model.

Fig 10. Intake Flow (i) Forecone and inlet cowl.
(ii) Shock pattern between splitters.

Fig 11. Expansion Nozzle Flow

Fig 12. Thrust Nozzle Performance. Area ratio = 5.84, γ = 1.4
P_f = combustion chamber pressure, M_f = combustion chamber Mach number.

Fig 13. Drag Without Fuel Injection. ——— theory, ⊡ experiment.

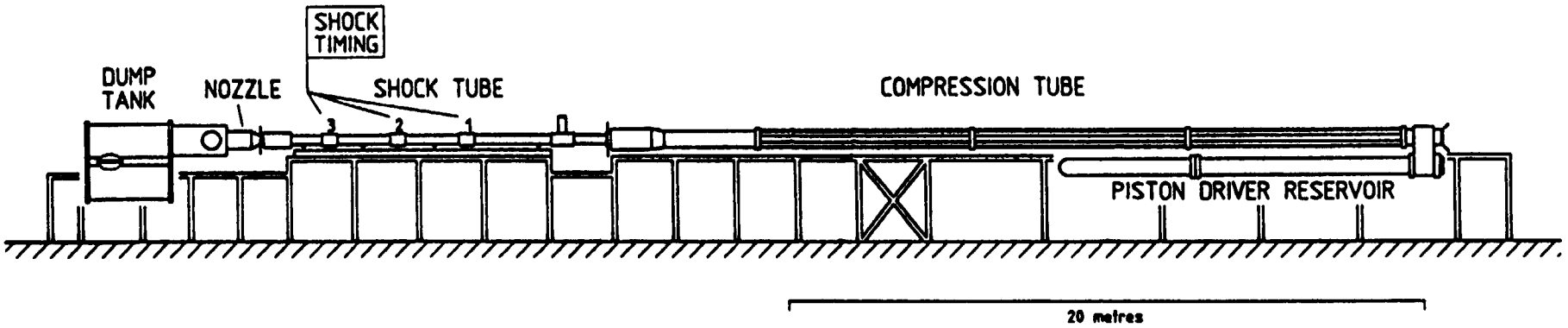
H_s = stagnation enthalpy
(a) Inviscid Drag
(b) Viscous Drag
(c) Resultant Drag.

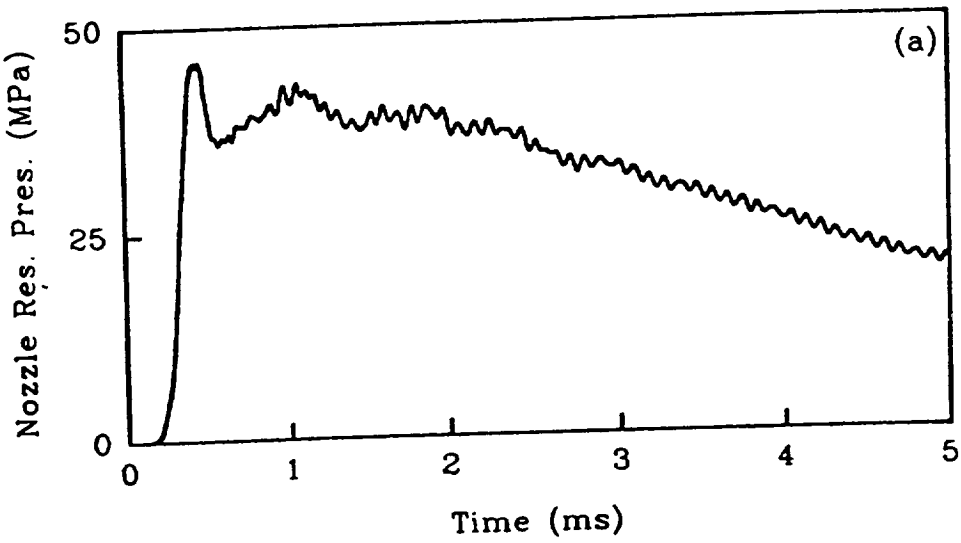
Fig 14. Combustion Features
(a) Experimental effect of fuel mass flow.
(b) Theoretical effect of combustion.
ΔF = thrust increment due to fuel injection, ϕ = equivalence ratio, P_c = post combustion pressure, T_c = post combustion temperature, M_c = post combustion Mach number, H_s = stagnation enthalpy.

Fig 15. Combustion Chamber Pressures
Fuel-off: O Experiment, – – – – – theory.
Fuel-on: △ Experiment, —— theory (ϕ = 0.77)
H_s = stagnation enthalpy.

Fig 16. Axial Force with Fuel Injection and Combustion
Equivalence ratio ϕ = 0.77, F_A = axial force (+ve for thrust),
H_s = stagnation enthalpy
(a) Inviscid axial force
(b) Viscous Drag

Fig 17. Resultant Axial Force
Fuel-on: Equivalence ratio ϕ - 0.77 ± 0.10
▽ Experiment, —— theory.
Fuel-off: □ Experiment, — theory.
F_A = axial force, P_p = Pitot pressure, H_s = stagnation theory.


SHOCK
TIMING
DUMP
TANK
NOZZLE
SHOCK TUBE
3
2
1
COMPRESSION TUBE
PISTON DRIVER RESERVOIR
20 metres


(a)
Nozzle Res. Pres. (MPa)
50
25
0
0
1
2
3
4
5
Time (ms)

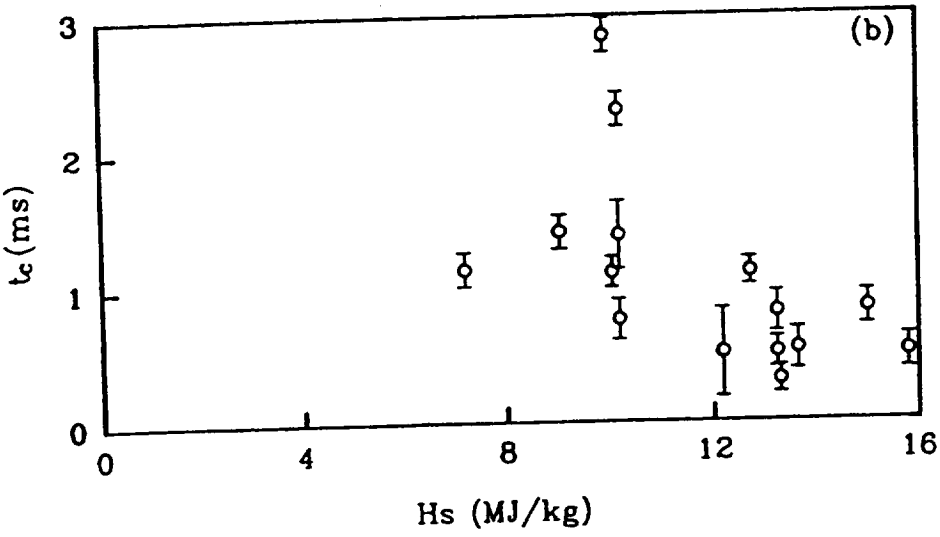
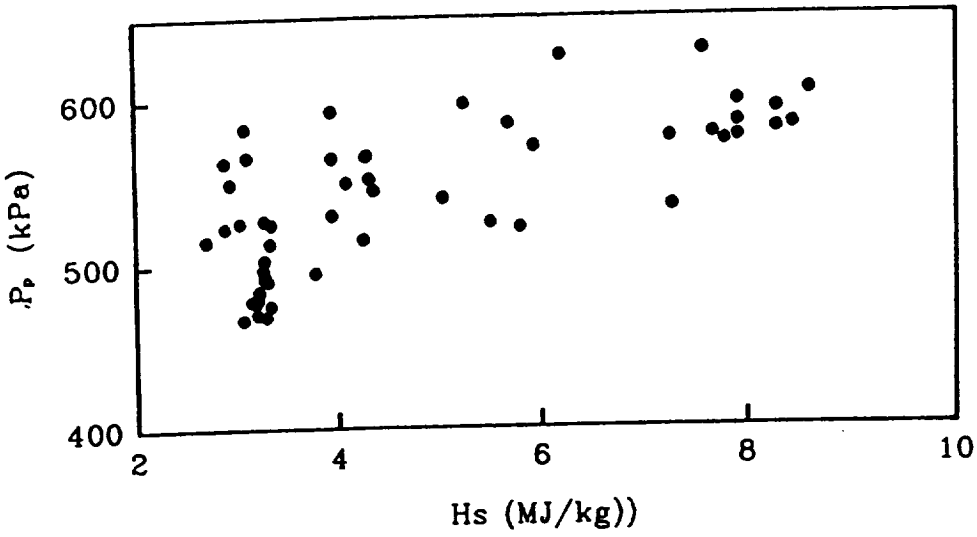
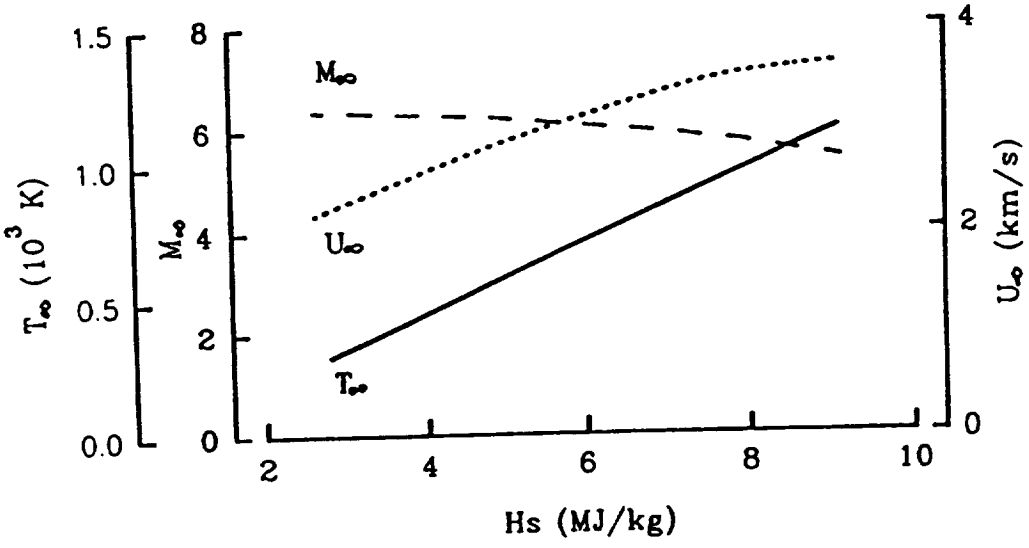

(b)
t_c (ms)
3
2
1
0
0
4
8
12
16
Hs (MJ/kg)

Fig 2



(a) Measured Pitot Pressure



(b) Calculated Conditions

Fig 3

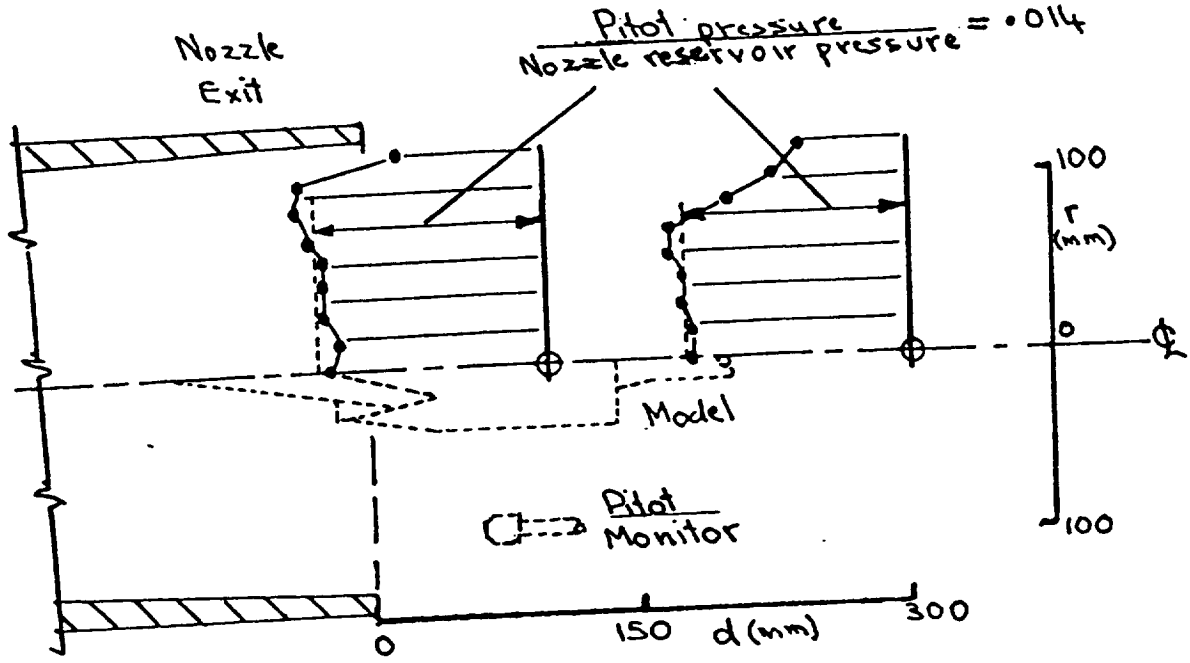


Fig 4. Test Section Flow Calibration and Location of Model. Stagnation enthalpy 8 $MJ.kg^{-1}$.

• Pitot survey measurements, d = downstream distance from nozzle exit, r = distance from centreline

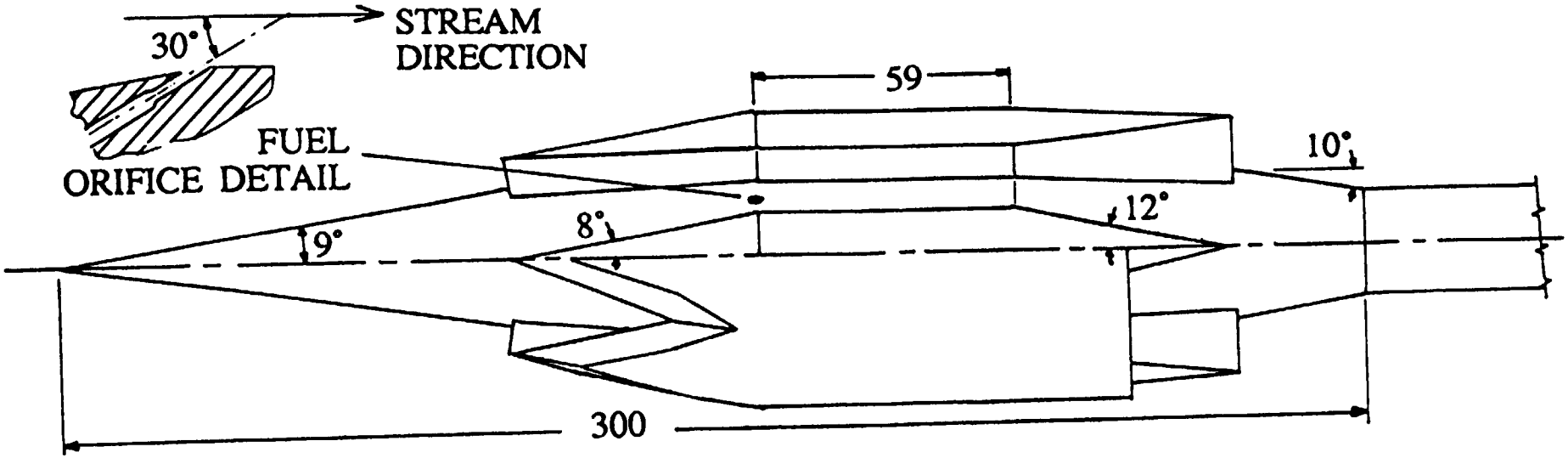


Fig 5. The scramjet model

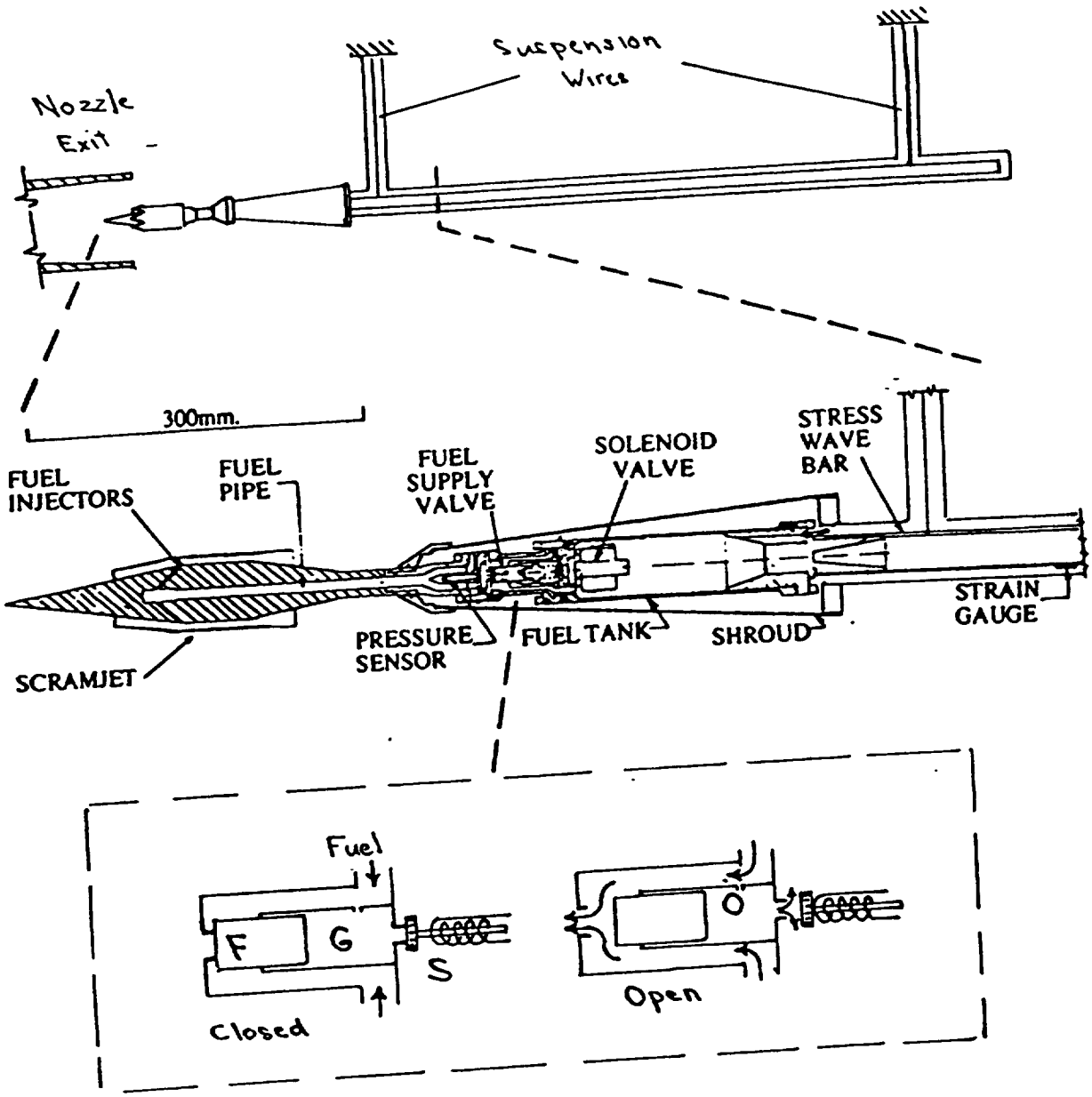


Fig 6. Model, Fuel Supply System and Model Mount

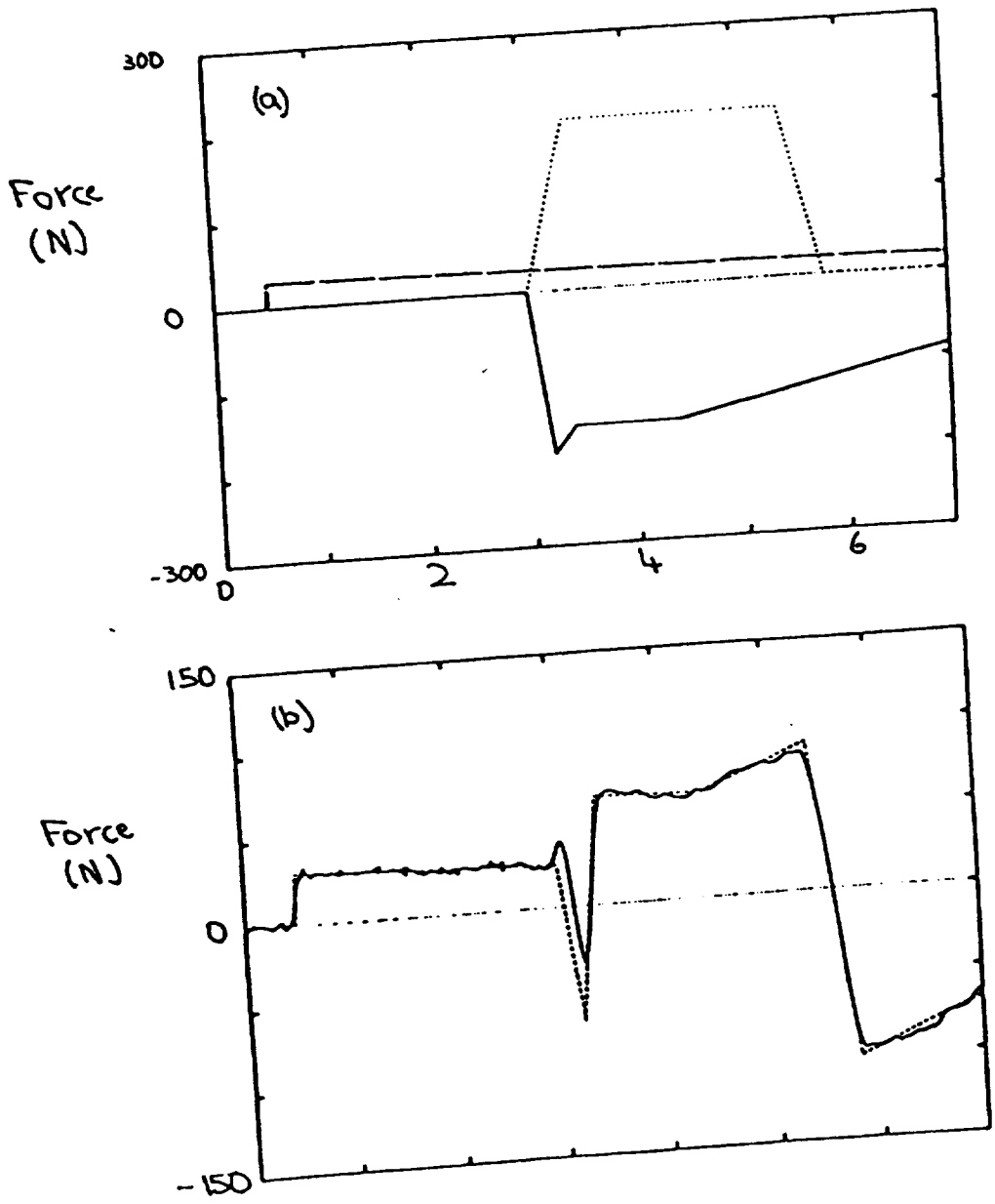


Fig 7. Simulation of Distributed Load (a) Input loads
—— fuel injection —— Drag ------ Thrust.
(b) Output. —— deconvolved load ---- true input.

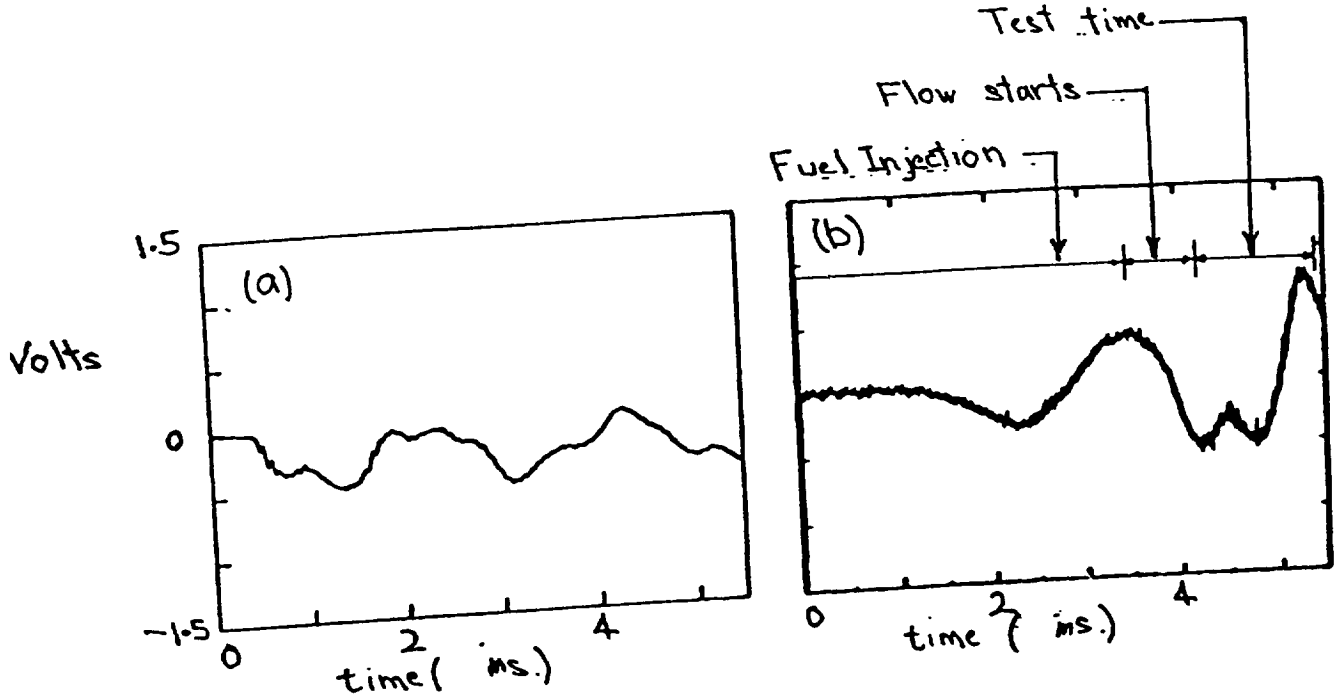
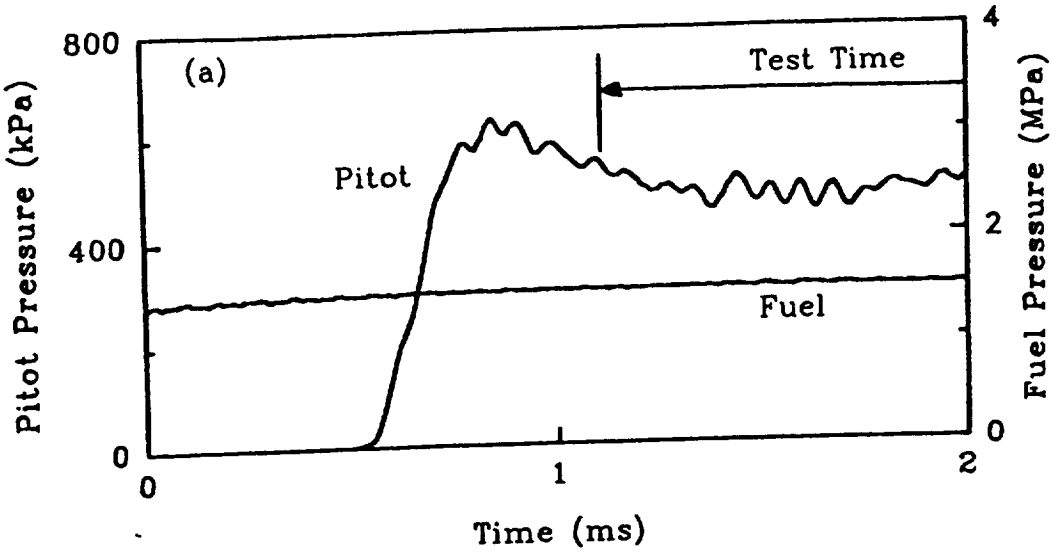


Fig 8 Strain Gauge Outputs (a) Response to step load
(b) Response during test


(a)
Test Time
Pitot
Fuel
800
400
0
4
2
0
0
1
2
Pitot Pressure (kPa)
Fuel Pressure (MPa)
Time (ms)

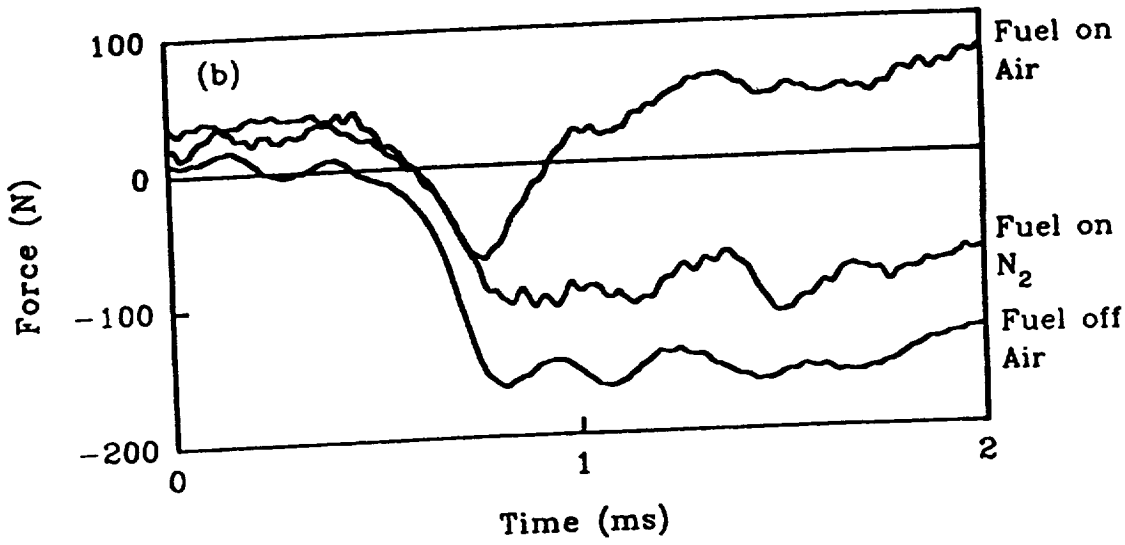

(b)
100
0
−100
−200
0
1
2
Force (N)
Time (ms)
Fuel on Air
Fuel on N_2
Fuel off Air

Fig 9 a/b

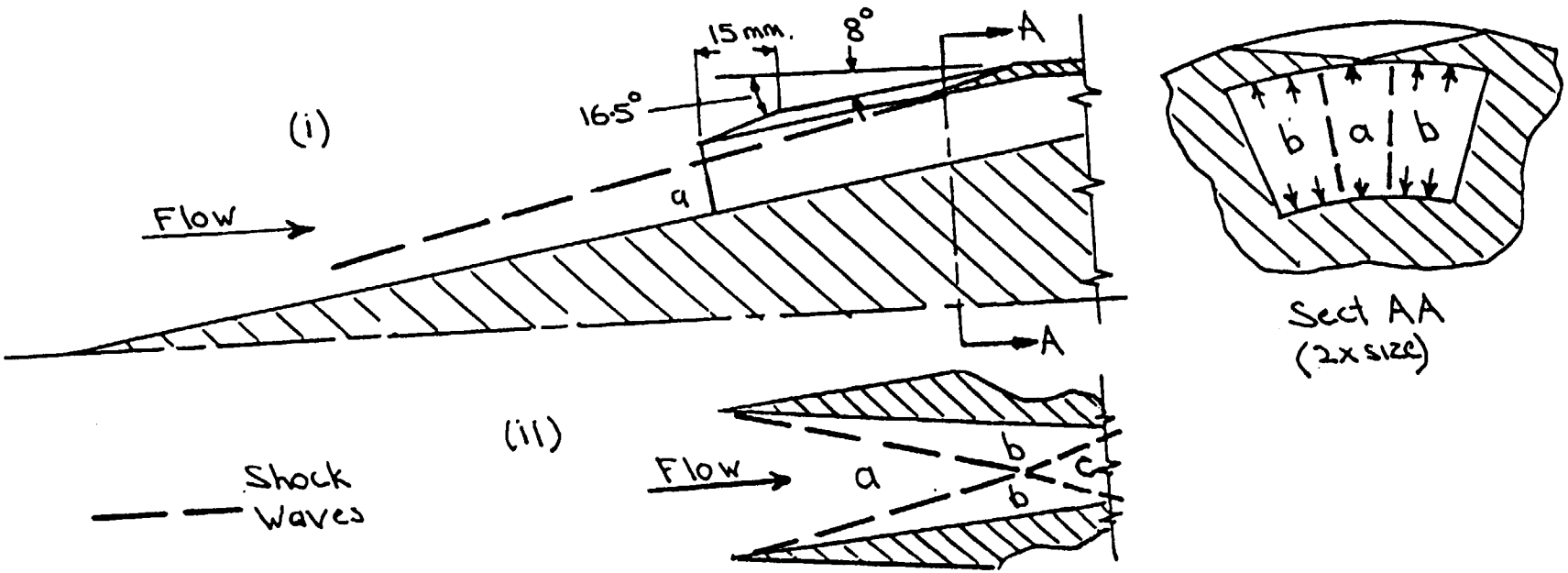


Fig 10. Intake Flow (i) Forecone and Inlet Cowl
(ii) Shock pattern between Splitters.

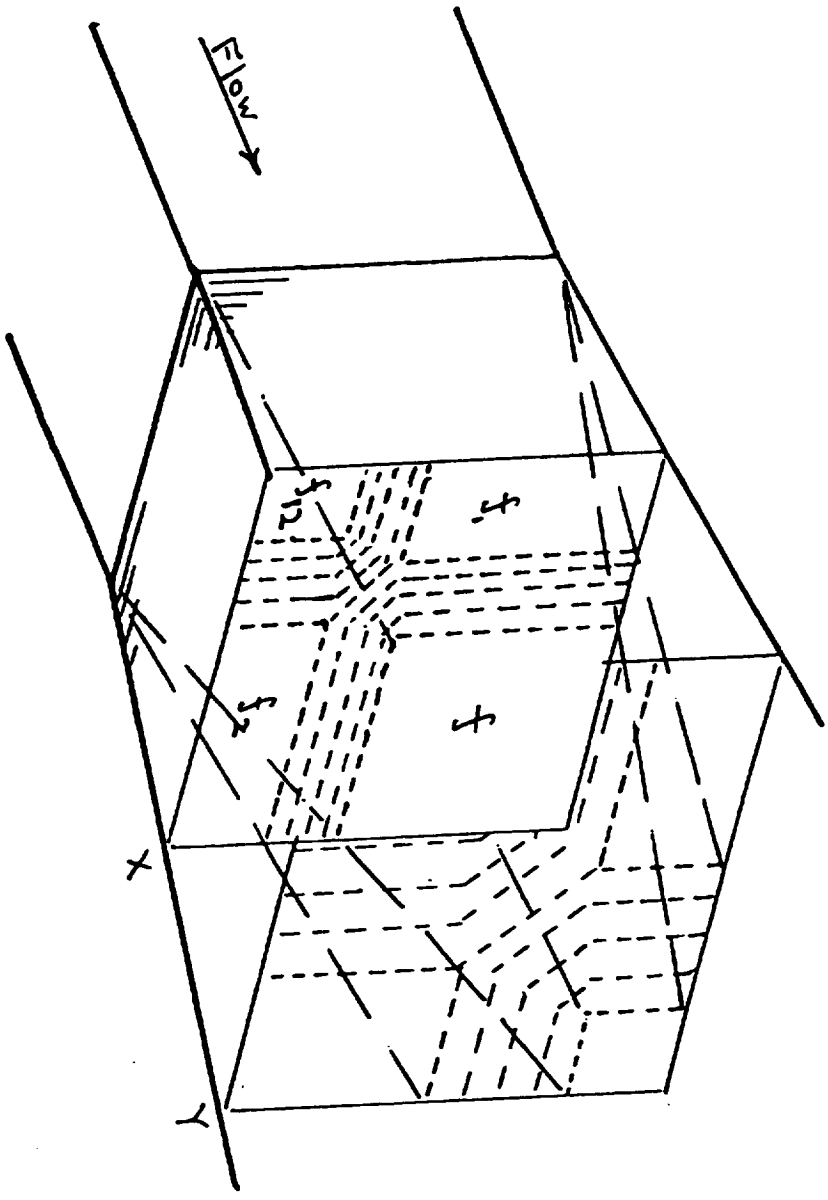


Fig 11. Expansion Nozzle Flow

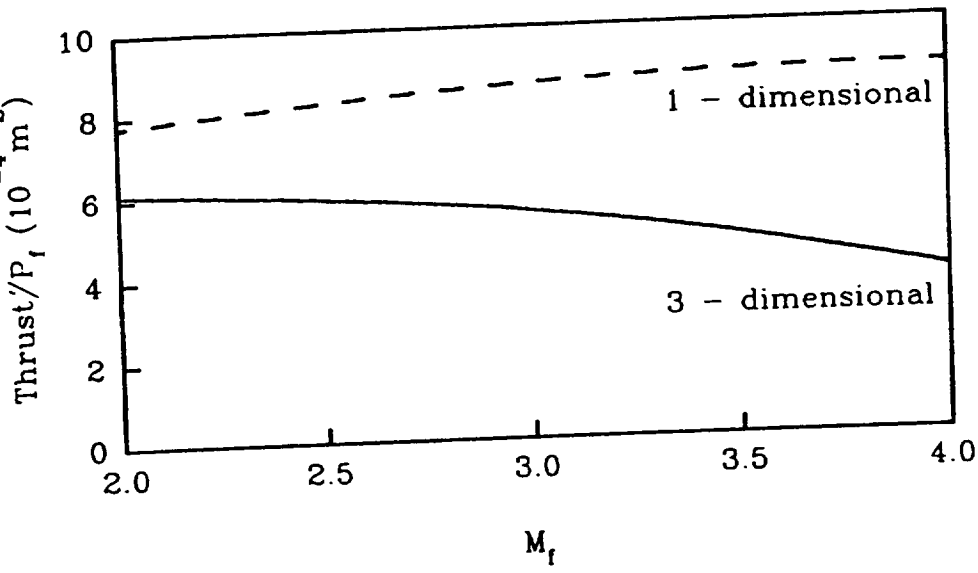
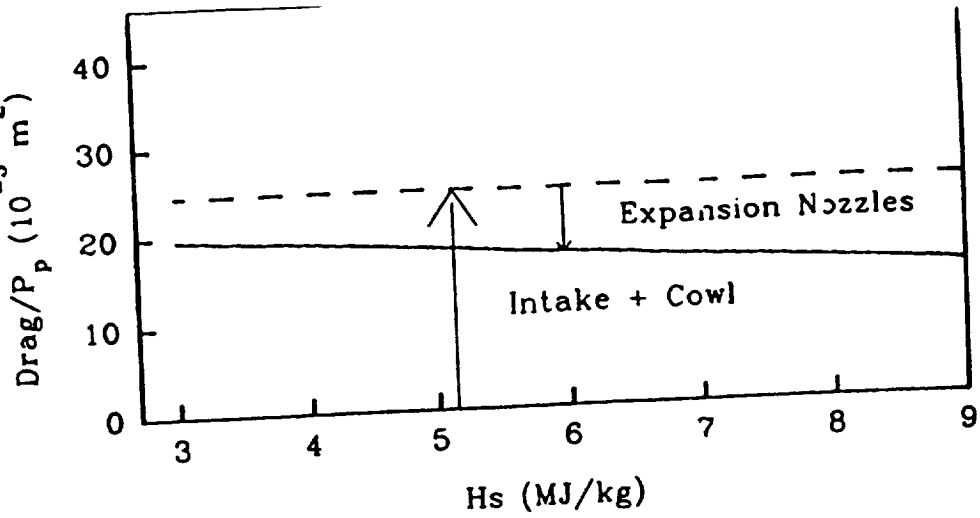
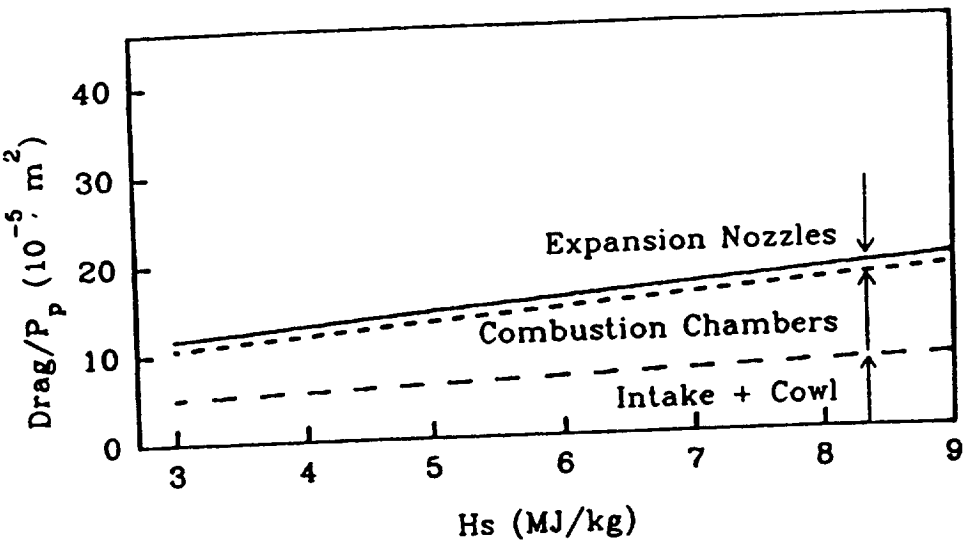

10
8
6
4
2
0
2.0
2.5
3.0
3.5
4.0
Thrust/P_t (10^{-4} m^2)
M_f
1 – dimensional
3 – dimensional

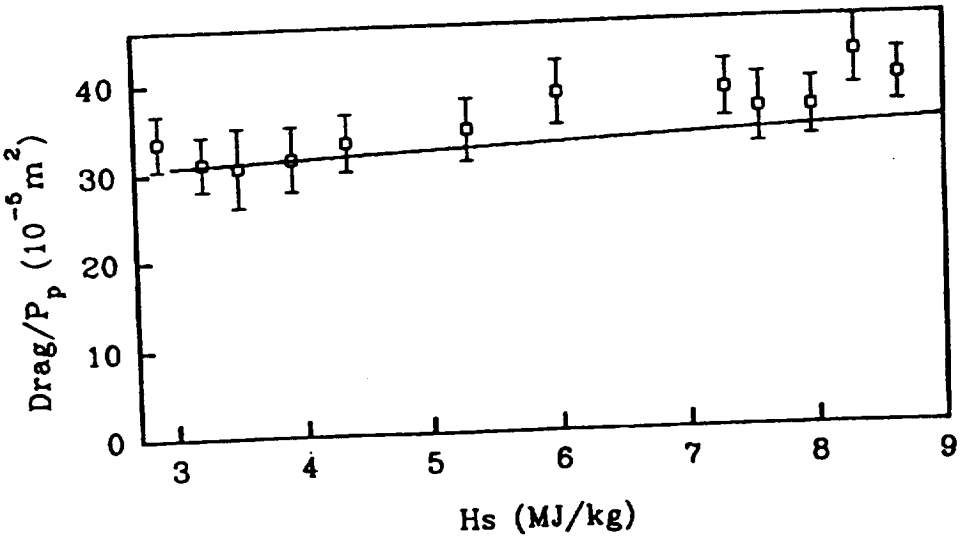
Fig 12



(a) Inviscid Drag



(b) Viscous Drag



(c) Resultant Drag

Fig 13.

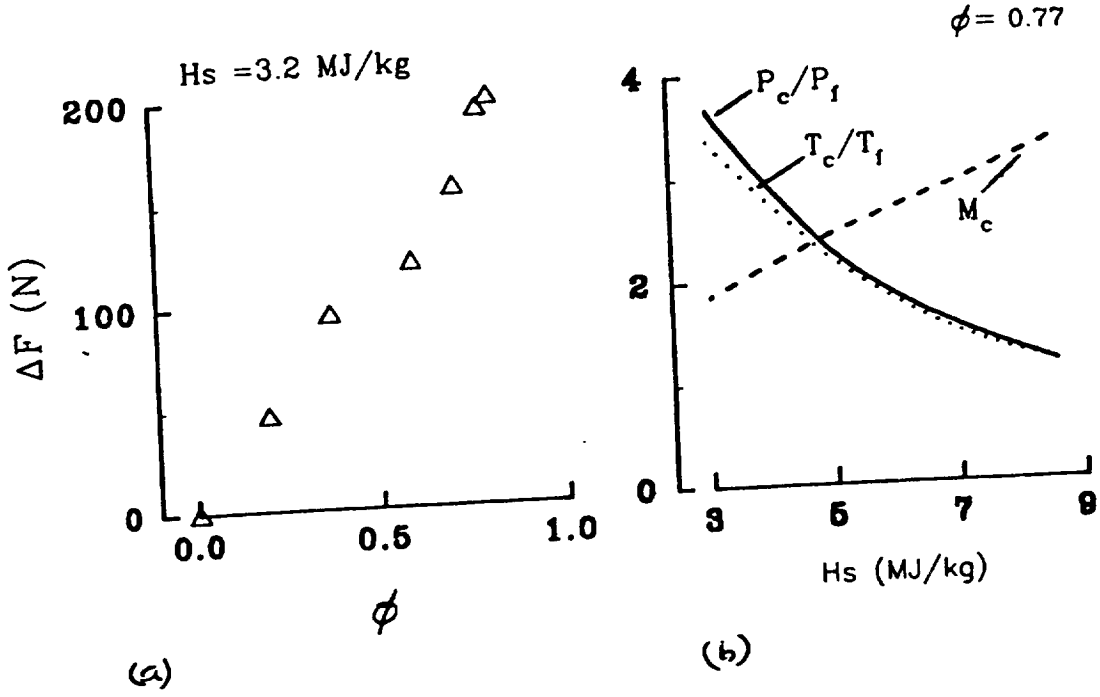
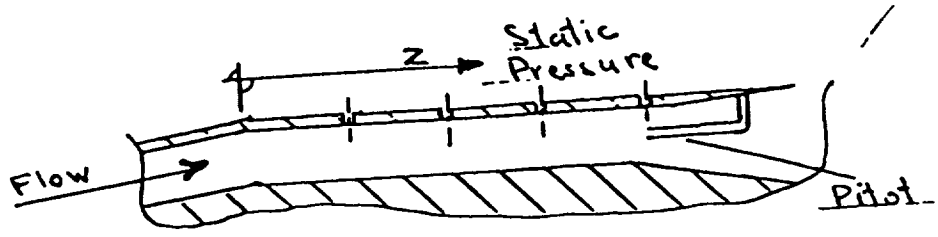
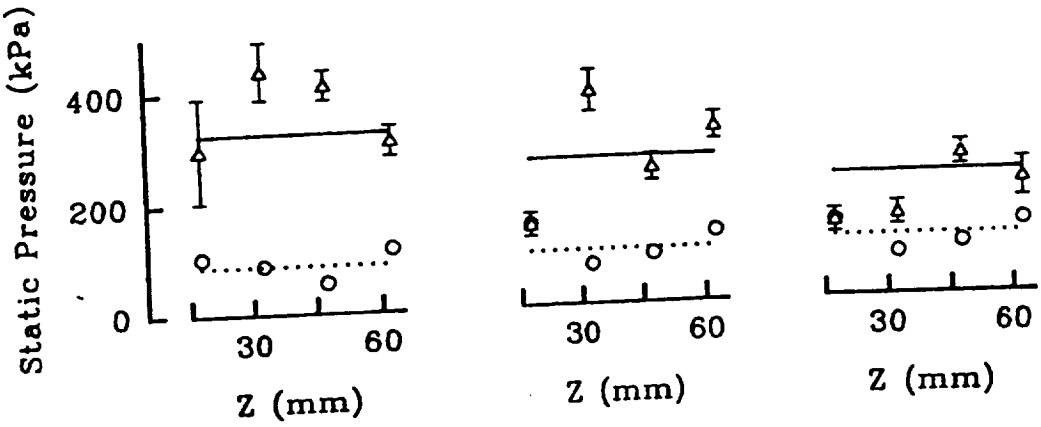

Hs =3.2 MJ/kg
200
100
0
ΔF (N)
0.0
0.5
1.0
ϕ
(a)
ϕ= 0.77
4
2
0
P_c/P_f
T_c/T_f
M_c
3
5
7
9
Hs (MJ/kg)
(b)

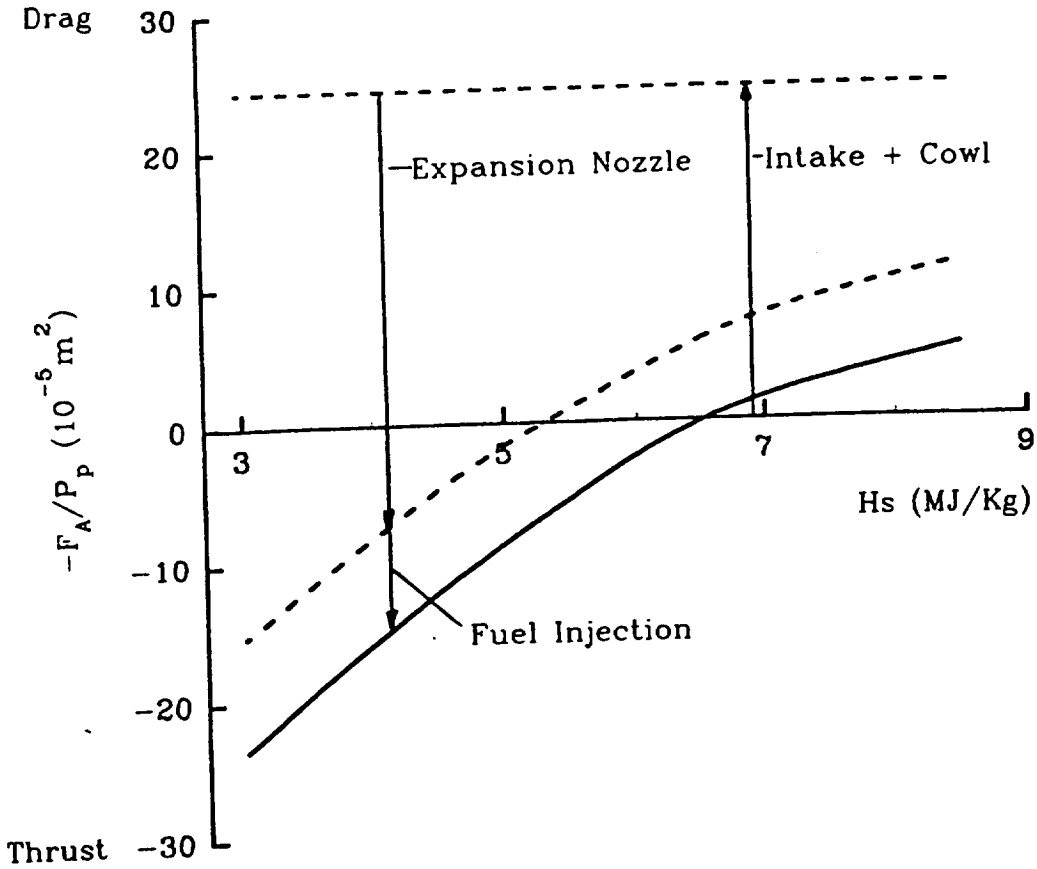
Fig 14



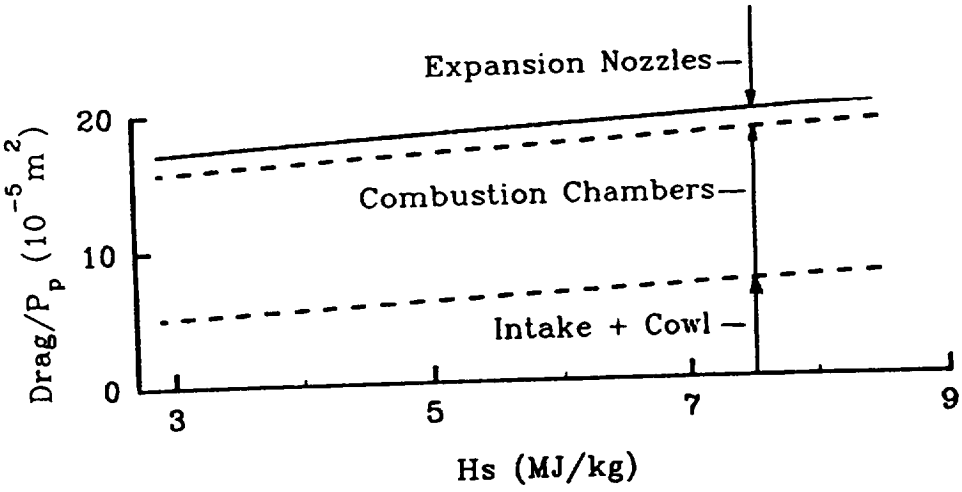


Hs (MJ/kg) 3.2 4.3 5.5

Fig 5



(a) Inviscid Axial Force



(b) Viscous Drag

Fig 16

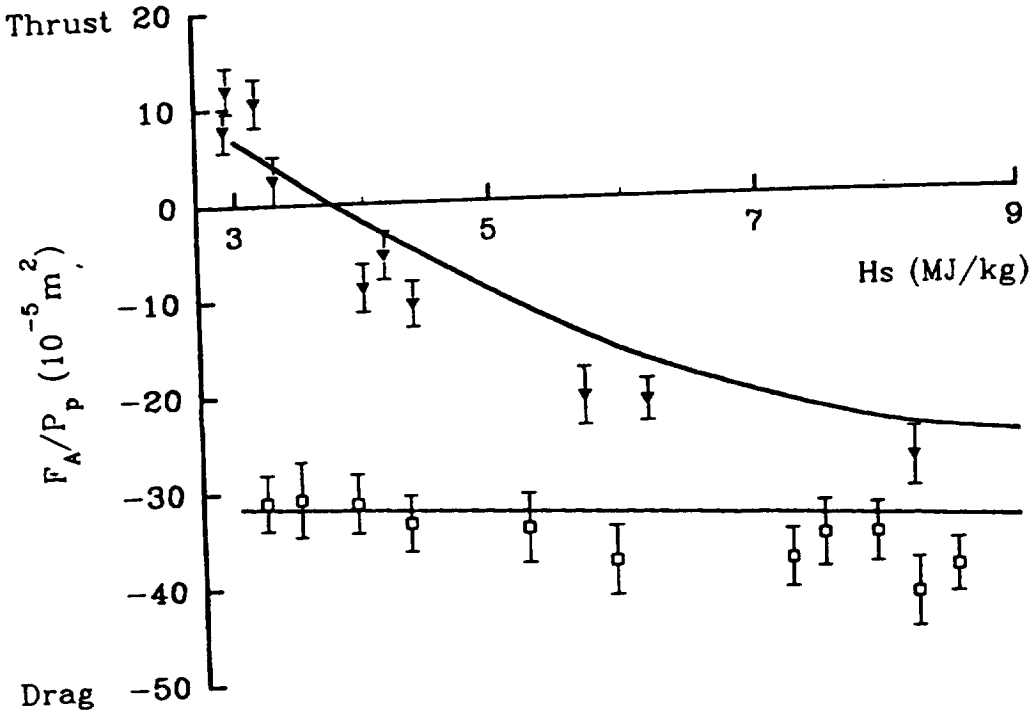


Fig 17

SPECIES MEASUREMENTS IN A HYPERSONIC, HYDROGEN-AIR, COMBUSTION WAKE

(Running Title: Species in a Combustion Wake)

K.A. Skinner* and R.J. Stalker†

Department of Mechanical Engineering

The University of Queensland

Brisbane Queensland 4072

ABSTRACT

A continuously sampling, time-of-flight mass spectrometer has been used to measure relative species concentrations in a two-dimensional, hydrogen-air combustion wake at mainstream Mach numbers exceeding 5. The experiments, which were conducted in a free piston shock tunnel, yielded distributions of hydrogen, oxygen, nitrogen, water and nitric oxide at stagnation enthalpies ranging from 5.6 MJ kg^{-1} to 12.2 MJ kg^{-1} and at a distance of approximately 100 times the thickness of the initial hydrogen jet. The amount of hydrogen that was mixed in stoichoimetric proportions was approximately independent of the stagnation enthalpy, in spite of the fact that the proportion of hydrogen in the wake increased with stagnation enthalpy. Roughly 50% of the mixed hydrogen underwent combustion at the highest enthalpy. The proportion of hydrogen reacting to water could be approximately predicted using reaction rates based on mainstream temperatures.

* Postgraduate Student

† Emeritus Professor of Space Engineering

1. INTRODUCTION

The mixing and burning of a hydrogen wake or jet in air at hypersonic speeds is an essential process of very high speed scramjet propulsion[1,2]. It may occur in the combustion chamber of a scramjet, where rapid mixing and combustion is desirable, or it may occur in the inlet, in which case injection of the hydrogen with rapid mixing but delayed combustion is required. It has received limited attention up to the present[3,4]. Most studies of hydrogen-air wakes have been confined to air stagnation enthalpies below 2 MJ kg^{-1} [5]. With precombustion temperatures of 800 K or more required for hydrogen, this implies that airstream Mach numbers have been limited to around 2.8.

Measurements of relative species concentrations in a two-dimensional wake at stream Mach numbers of 5.2 and above are reported here. The measurements were done in a shock tunnel, using a continuously sampling time-of-flight mass spectrometer, and involved a range of freestream temperatures sufficient to produce wake flows with and without combustion. Accompanying Pitot measurements in the wake were also made. The freestream Reynolds' number, based on the length of the wake, varied from 1.3×10^6 to 2.9×10^6, indicating that the wake was well and truly turbulent.

2. EXPERIMENTAL ARRANGEMENT

The experiments were conducted in the free piston shock tunnel T4 at The University of Queensland[6]. This employed a 75 mm diameter shock tube with a free piston driver, and was operated in the shock reflection mode. A contoured nozzle, with a 25 mm diameter shock and a nominal area ratio of 110, was located at the downstream end of the shock tube, and produced a hypersonic free jet with a uniform core diameter of approximately 200 mm at the nozzle exit. Mixtures of argon and helium were used as driver gas.

The experimental arrangement is shown schematically in fig. 1. The hydrogen-air wake was formed inside a rectangular duct, located with its leading edge 120 mm from the nozzle exit. A fuel injection strut was mounted in the midplane of the duct, spanning the shorter dimension, and hydrogen was injected from its trailing edge. The mass spectrometer was mounted to traverse the wake in the centre of the duct at 500 mm from the injection strut trailing edge.

The duct and fuel injector are shown in more detail in fig. 2. The injector was 7.6 mm thick, and the hydrogen was injected at a Mach number of 3.2 through a two-dimensional nozzle which spanned the full 80 mm width of the duct. The leading edge of the duct was a wedge of 6.6° included angle and, as shown by the dotted lines in the figure, it was arranged that the flow disturbances from the wedge passed downstream of the measuring station without influencing the wake. The boundary layer on the strut was expected to be laminar, with a displacement thickness at the trailing edge of a fraction of a millimetre[7], and this was not expected to have a significant effect on the development of the wake.

3. THE MASS SPECTROMETER

As shown in fig. 1, the flow was sampled continuously through a 2 mm diameter orifice in the first of three conical skimmers. The cavity between the second and third skimmer was connected to a pre-evacuated dump volume, and the cavity after the third skimmer, containing the gas analysis equipment, was connected to a separate pre-evacuated dump volume. Pressures were low enough to ensure that the test gas passed into the latter cavity in the form of a molecular beam. This beam was bombarded by an electron gun, and the ions produced were extracted from the beam and accelerated before passing into the drift tube, to be ultimately detected by the electron multiplier at the end of the drift tube. The electron gun

was pulsed on for 200 nanoseconds every 55 microseconds, and each pulse produced a packet of ions which, because their time of flight depended on the individual mass of the ions, could be detected and analysed for mass at the electron multiplier. Thus a complete mass spectrum, with a signal proportional to the numbers of ions of each mass arriving at the electron multiplier, was produced every 55 microseconds during the shock tunnel test time. This was recorded using a 50 MHz storage oscilloscope. More detail on the mass spectrometer is given in refs. 8 and 9.

To interpret the signal in terms of the number of particles of each species sampled by the mass spectrometer, published ionization cross-sections were used[9]. These were incorporated into calibrations which accounted for mass separation effects in forming the molecular beam, and in collecting the ions for passage through the drift tube, by using the mass spectrometer to sample known mixtures of helium-nitrogen, argon-nitrogen, and hydrogen-nitrogen in the tunnel freestream at varying stagnation enthalpies and Pitot pressures. The calibrations resulting from this process are considered to be accurate to within 20% in the measurement of hydrogen, 25% in water, 10% in oxygen, nitrogen, nitric oxide and argon, and 5% in helium.

Fig. 3 displays typical records of hydrogen and water mole fractions obtained in the wake, with a reading every 55 microseconds. The mainstream flow wake transit time was approximately 150 microseconds, so results were taken in the time interval from 0.5 milliseconds to 1 millisecond, in order that a steady flow state could be achieved. The error bars display the uncertainty in reading the records. It can be seen that, in this case, the mole fractions are not steady after 0.75 milliseconds, so readings were not taken after that time.

4. FLOW CONDITIONS

Experiments were conducted at the four flow conditions set out in table 1. The composition of the shock tunnel driver gas was varied with stagnation enthalpy to ensure that the pressure at the end of the shock tube remained steady (to within ± 5%) after shock reflection. The stagnation enthalpy was obtained by using the shock speed and the shock tube filling pressure to calculate the conditions after shock reflection, and expanding to the measured pressure where necessary. The Pitot pressure and static pressure were measured at the entrance to the test duct, and were used to guide the choice of area ratio for the shock tunnel nozzle expansion. Using this area ratio, the test conditions were calculated numerically[10] for a one-dimensional steady expansion from the reservoir conditions at the end of the shock tube.

The hydrogen fuel was injected parallel to the mainstream flow, but was slightly over expanded and therefore the jet experienced some recompression to bring it to the mainstream pressure. The conditions in the jet after it was recompressed are displayed in table 1, and are based on calibrations of the injector with hydrogen flow[11]. The fuel flow rates were chosen so that, at the lowest stagnation enthalpy, an equivalence ratio of one would be obtained if a section of the mainstream of 50 mm height was being fuelled. As will be seen below, this is slightly greater than the height of the wake at the measuring station, and therefore can be regarded as encompassing all of the mainstream involved in the mixing process. This "relative equivalence ratio" was increased with stagnation enthalpy, in accordance with what might be expected in a scramjet application.

Table 1. Test Conditions

Mainstream				
Stagnation enthalpy (MJ kg^{-1})	12.2	9.4	7.8	5.6
Driver gas composition (Ar/He)	12/88	17/83	23/77	25/75
Nozzle reservoir pressure (MPa)	40	40	40	40
Mach number	5.2	5.4	5.6	5.7
Temperature (K)	1750	1340	1050	760
Density (kg m^{-3})	0.037	0.045	0.052	0.069
Velocity (M s^{-1})	4260	3840	3550	3120
Pitot pressure measured (kPa)	600	630	620	570
calculated (kPa)	625	615	605	618
Static pressure measured (kPa)	20	17	13	11
calculated (kPa)	19.4	17.6	15.8	15.1
Hydrogen Fuel Jet				
Mach number	2.8	2.8	2.9	2.8
Temperature (k)	117	114	113	114
Density (kg m^{-3})	0.041	0.036	0.028	0.024
Velocity (m s^{-1})	2280	2300	2310	2300
Thickness (mm)	4.8	5.2	5.3	5.1
Relative equivalence ratio	2.2	1.9	1.4	1.0

It will be noted that the thickness of the jet after recompression was approximately 5 mm. The traverse measurements were done at a downstream distance which was 100 times greater than this, to enable a wake structure to be formed. This was confirmed by calculations of the air-hydrogen mixing layer at the top and the bottom of the jet[12,13], which showed that the two

mixing layers closed to eliminate the inviscid core of hydrogen flow and form a wake at approximately 125 mm downstream.

5. RESULTS AND DISCUSSION

The number of particles of each species sampled by the mass spectrometer was converted into mole fractions by dividing by the total number of particles, and the results plotted in fig. 4 for each of the major species present, at each of the four stagnation enthalpies tested. Atomic species and the hydroxyl radical were not present in measurable quantities. The points plotted represent the mean of the values obtained from the sequence of mass spectra obtained in any one test, with the error bars representing the standard errors of those mean measurements.

The figure displays an increasing predominance of hydrogen in the wake as the enthalpy is raised, with an associated reduction in nitrogen. This is a reflection of the increased flow of hydrogen, as noted by the relative equivalence ratio of table 1. This also causes a reduction in the mole fraction of oxygen, but at the higher enthalpies this is due to combustion as well. This is shown by the increasing mole fraction of water formed. It will be noted that contamination of the test flow by the helium-argon driver gas increases with the stagnation enthalpy. However, this is not expected to significantly influence the results as the driver mixture is chemically inert, and a 20% mole fraction of the mixture would reduce the stagnation enthalpy by less than 10%.

As indicated by the vertical arrows, the measured levels of oxygen are some 50% in excess of expected values, in relation to nitrogen, at 15 mm at 9.4 MJ kg^{-1} and 5 mm and 10 mm at 5.6 MJ kg^{-1}. This phenomenon has occurred occasionally in other tests with the mass spectrometer, and is not yet explained. Fortunately, the error incurred is not sufficient to

significantly affect the results below.

The results of Pitot surveys of the wake are shown at the top of fig. 5. The distribution of the average molecular mass, calculated from the results in fig. 4, is also presented and is seen to be similar to the Pitot pressure profile. Since the Pitot pressure may be closely approximated by ρu^2, where ρ is the density and u the velocity, this similarity suggests that, through its influence on the density, the effect of hydrogen on the molecular mass is the main factor determining the variation of Pitot pressure across the wake.

Since the wake is well developed at the traverse station, it would be expected that the velocity and temperature throughout the wake would be reasonably close to the freestream values. This was confirmed by noting that the wake developed at constant pressure, and therefore it was possible to equate the momentum in the wake (as measured by the Pitot pressure profile) to the initial momentum of the hydrogen jet together with that of the mainstream fluid captured by the wake. Then, by assuming a linear variation of velocity with distance normal to the wake centreline, an estimate of the magnitude of the velocity could be obtained. The temperature was then related directly to the square of the velocity by making the further assumption that the distribution of Pitot pressure across the wake is identical with the distribution of average molecular mass, and the static pressure is constant. For the four test conditions considered, this process yielded a mean velocity in the wake which was within 95% of the mainstream velocity, and a mean temperature which was within 90% of the mainstream value.

Having established that the velocity variation across the wake is relatively small, it becomes possible to make an approximate check on the magnitude of the hydrogen concentrations

measured by the mass spectrometer. The mass of hydrogen flow in the wake can be written as

$$\begin{aligned} m_H &= 2\int_0^{\delta} c_H \rho u \, dy \\ &= 2\rho_\infty u_\infty \left\{ \int_0^{\delta} c_H \left(\rho u^2 / \rho_\infty u_\infty^2 \right) dy + \int_0^{\delta} c_H \left(\rho u^2 / \rho_\infty u_\infty^2 \right) \left(u_\infty / u - 1 \right) dy \right\} \end{aligned} \qquad (1)$$

where c_H is the mass fraction of hydrogen (in any form) at any point, y is the distance normal to the wake centreline, with δ its value at the edge of the wake, and ρ_∞ and u_∞ are values of ρ and u at some reference condition; in this case the mainstream values given by table 1. Thus, putting $\rho u^2/\rho_\infty u_\infty^2$ equal to the ratio of Pitot pressures, multiplying the total mole fraction of hydrogen (i.e. hydrogen + water) by the ratio of the molecular mass of hydrogen to the average molecular mass to obtain c_H, and integrating from the centre to the edge of the wake, the first term on the right hand side of eq. (1) is obtained. Noting that m_H is also given by the mass flow from the injector, which may be obtained from the density, velocity and thickness of the hydrogen jet in table 1, and that u has been assumed to be nearly equal to u_∞ it is clear that the ratio of m_H obtained in this manner, to the first term on the right hand side of eq(1) should be a little greater than one. In fact, the results yield an average value of 1.15 for the ratio, with a variation of +13% and -8%, thereby approximately confirming the mass spectrometer measurements.

The total mole fraction of hydrogen is also plotted in fig. 5 for the four test conditions, along with the fraction of hydrogen which is mixed with air in proportions approximate to complete combustion. Where the mixture is lean in hydrogen, all the hydrogen is counted, and where the mixture is rich, only an amount of hydrogen sufficient for combustion with the oxygen and nitric oxide is counted. This is referred to on the figure as mixed hydrogen. At any point, the ratio of mixed hydrogen to total hydrogen can be taken as a local mixing efficiency, η_m.

Strictly, to obtain an overall mixing efficiency in the wake would require knowledge of the distribution of ρu in the wake, but if it is once again assumed that the velocity variation across the wake is relatively small, it is possible to follow the procedure leading to eq. (1), and to obtain the mixed hydrogen as

$$\begin{aligned} m_{Hm} &= 2\int_0^\delta \eta_m c_H \rho u \, dy \\ &= 2\rho_\infty u_\infty \left\{ \int_0^\delta \eta_m c_H \left(\rho u^2 / \rho_\infty u_\infty^2 \right) dy \right\} \{ 1 + 0(u_\infty/u - 1) \} \end{aligned} \tag{2}$$

Performing the integration from the centre to the edge of the wake, and neglecting the term in $(u_\infty/u - 1)$, yields an approximation for the amount of hydrogen which is mixed. It is found that this amount is constant with ±15% for the results presented here, with no indication of a systematic variation over the test conditions.

An approximation for the overall mixing efficiency in the wake may be obtained from eqs. (1) and (2), again neglecting terms in $(u_\infty/u - 1)$, as

$$\eta_{mw} = \left\{ \int_0^\delta \eta_m c_H \left(\rho u^2 / \rho_\infty u_\infty^2 \right) dy \right\} \Big/ \left\{ \int_0^\delta c_H \left(\rho u^2 / \rho_\infty u_\infty^2 \right) dy \right\}$$

This yielded the values of η_{mw} presented in table 2. Because the amount of hydrogen injected was increased with stagnation enthalpy, but the amount of hydrogen mixed remained approximately constant, the wake mixing efficiency reduced with increasing enthalpy. It would seem that the increase in fuel flow serves no useful purpose, until it is noted that the hydrogen which is not "mixed", in the sense in which the term is used here, will still be effective in reducing post-combustion temperatures.

Table 2. Measurements of Overall Mixing Efficiency

Stagnation Enthalpy (MJ kg^{-1})	12.2	9.4	7.8	5.6
Mixing Efficiency η_{mw} (%)	30	42	63	60

The ratio of water concentration to that of mixed hydrogen indicates the proportion of mixed hydrogen that has reacted, and forms a local reaction efficiency. This is shown on the lower portion of fig. 5, where it is plotted as a series of bars indicating the expected uncertainty. It can be seen that more than half of the mixed hydrogen has reacted at the highest enthalpy, and very little indeed at the low enthalpies.

It is of interest to make a simple, first order estimate of the level of reaction. This can be done by assuming that the hydrogen-air mixture may be regarded as mixed for a period of time given by L/u_∞ where L is the length of the wake, measured from the point of injection of hydrogen to the traverse station. During that time it first undergoes an ignition delay, given by [14]

$$\tau_i = 8 \times 10^{-3}\, p^{-1} \exp(9600/T) \quad . \tag{3}$$

Here the time τ_i is measured in microseconds, the pressure p in atmospheres, and the temperature T in K. In the remaining time it reacts, and the proportion of hydrogen which burns to form water can be expressed as

$$\alpha_H = (L/u_\infty - \tau_i)/\tau_R$$

where τ_R is the heat release time in microseconds, given by[14]

$$\tau_R = 105\, p^{-1.7} \exp(-1.12\, T/1000) \quad . \tag{4}$$

These expressions for τ_i and τ_R are subject to considerable theoretical uncertainty [15], but are taken as the best estimate of reaction rates for the present purpose. Assuming that T is equal to the mainstream static temperature then yields the levels for the ratio of water to mixed hydrogen which are shown by the broken lines in the lower part of fig.5 at 12.2 and 9.4 MJ kg^{-1}. It can be seen that they are reasonably consistent with the experimental values. The ignition delay predicted for 7.8 and 5.6 MJ kg^{-1} is too long to permit the formation of water, and it is thought that the small amounts observed may be due to reactions involving nitric oxide [15], together with a very small residual amount, probably associated with outgassing.

6. CONCLUSION

Mass spectrometric traverses of a hypersonic combustion wake have yielded the distribution of hydrogen, oxygen, nitrogen, water and nitric oxide. Comparison with Pitot traverses indicated that the variation of Pitot pressure was largely due to the influence of hydrogen on the molecular weight, suggesting a wake structure dominated by hydrogen diffusion. The amount of hydrogen that was mixed in stoichiometric proportions was approximately independent of the stagnation enthalpy, in spite of considerable combustion taking place, and considerably more hydrogen being injected, at the highest enthalpy. When combustion took place, the degree of combustion could be approximately predicted using reaction rates based on mainstream conditions.

The prime purpose of the experiments was to assess the utility of the mass spectrometer in this shock tunnel application. However, it is worth making some remarks concerning possible implications of the results for scramjet operation. In a scramjet combustion chamber, pressures are expected to be almost an order of magnitude higher than in these tests and, as

shown by eqns(3) and (4), combustion will occur much more rapidly in relation to mixing. Thus, if fuel injection takes place in the combustion chamber, mixing limitations will be predominant. However, pressures in the inlet are likely to be an order of magnitude lower than in these tests, so that combustion will occur much more slowly. Noting that flow temperatures at the two lower enthalpy conditions tested are likely to be typical of inlet temperatures in flight, and that because of the lower pressures ignition delay and heat release times will be much greater than the minimum values of 0.5 milliseconds and 1 millisecond respectively which can be calculated from eqns(3) and (4) for the conditions of these tests, it is clear that wake lengths of several metres can be sustained without significant reaction. Therefore Reynolds' numbers equal to or greater than those obtained in the present tests can be achieved, leading to the same or a greater degree of mixing. Thus it appears that wake mixing efficiencies in the inlet exceeding 60% can be obtained without reaction, indicating that inlet injection [16] may offer an effective method of relieving mixing problems in the combustion chamber.

Acknowledgments. The authors gratefully acknowledge the support received for this work from the Australian Research Council and under NASA grant NAGW-674.

REFERENCES

1. Ferri, A. *J. Royal Aero. Soc.* 68:575 (1964).
2. Billig, F.S. *J. Propulsion & Power* 9:499 (1992).
3. Casey, R.T., Stalker, R.J. & Brescianini, C. *J. Royal Aero. Soc.* 96:200 (1992).
4. Bakos, R.J., Tomagno, J., Rizkalla, O., Pulsonetti, M.V., Chinitz, W. & Erdos, J.I. *J. Propulsion & Power* 8:900 (1992).
5. Evans, J.S. & Schexnayder, C.J. Jr., *AIAA Journal* 18:188 (1980).

6. Stalker, R.J. in "Current Topics in Shock Waves" AIP Conference Proceedings 208 (Y.W. Kim, ed) American Institute of Physics, New York, 1990, pp 96-105.

7. Anderson, J.D. Jr., "Fundamentals of Aerodynamics" 2nd ed, McGraw-Hill, New York, 1991. Ch.17, p711.

8. Skinner, K.A. & Stalker, R.J., *AIAA Journal.* 32:2825 (1994).

9. Skinner, K.A., "Mass Spectrometry in Shock Tunnel Experiments" PhD Thesis, Univ. of Qld. (1994).

10. Lordi, J.A., Mates, R.E. & Moselle, J.R. NASA CR-472 (1966).

11. Buttsworth, D.R. "Shock Induced Mixing and Combustion in a Scramjet" PhD thesis, Univ. of Qld. (1994).

12. Dimotakis, P.E., in "High Speed Flight Propulsion Systems" (Murthy, S.N.B. & Curran, E.T. eds), Progress in Astronautics & Aeronautics, V137, pp265-340 (1991).

13. Papamoschou, D. & Roshko, A. *J. Fluid Mechanics* 197:483 (1988).

14. Huber, P.W., Schexnayder, C.J. Jr. & McClinton, C.A. NASA Tech. Paper 1457 (1979).

15. Rogers, R.C. & Schexnayder, C.J. Jr. NASA Tech. Paper 1856 (1981).

16. Rubins, P.M. & Bauer, R.C., *J. Propulsion & Power* 10:593 (1994).

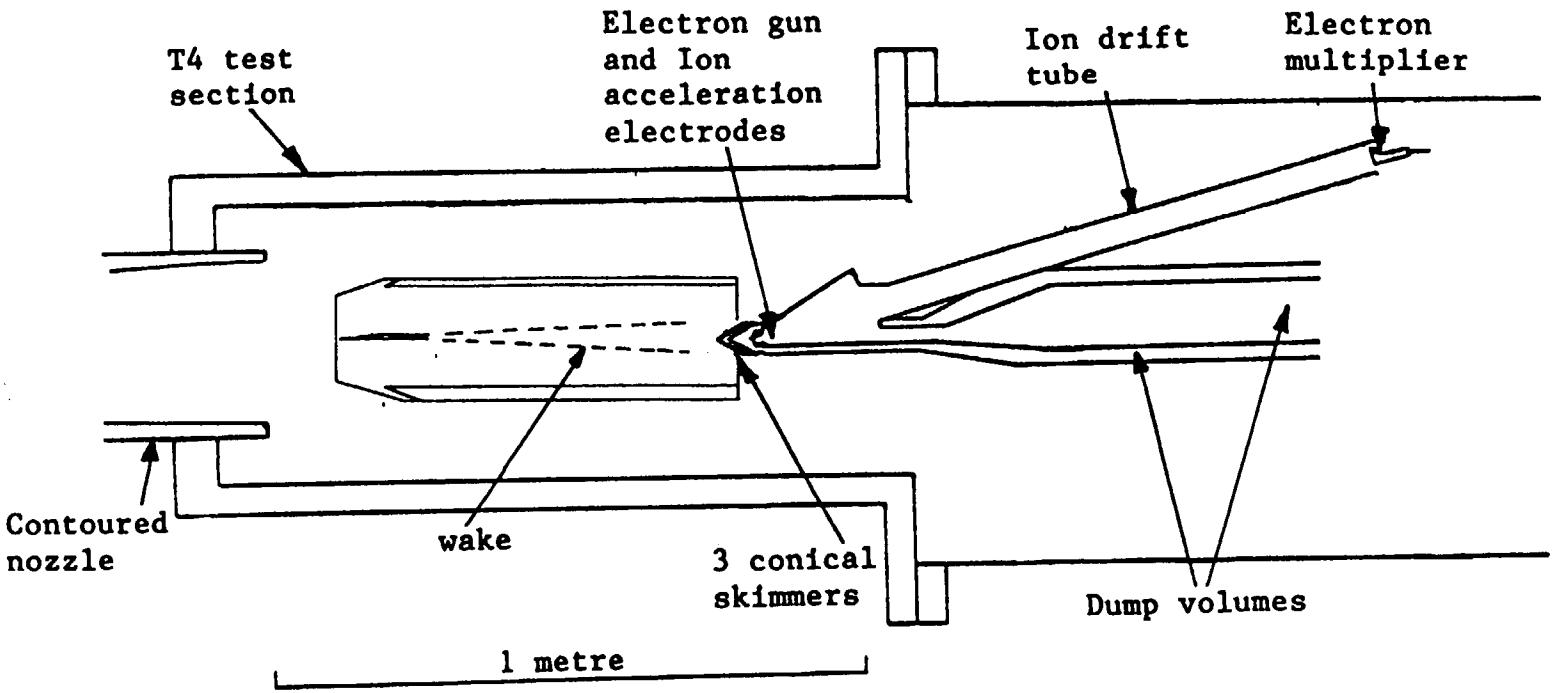


Fig. 1 Experimental arrangement.

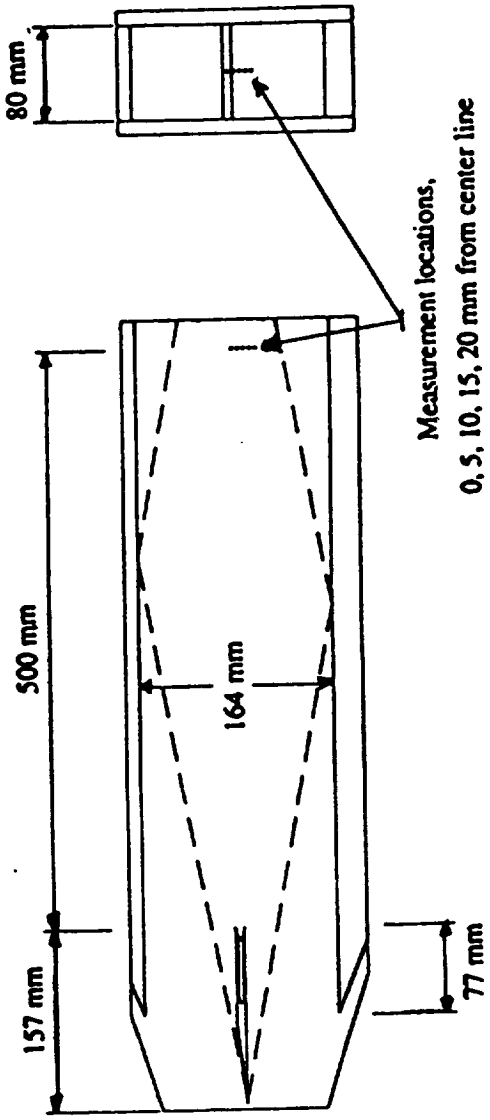


Fig. 2 Detail of experimental duct.

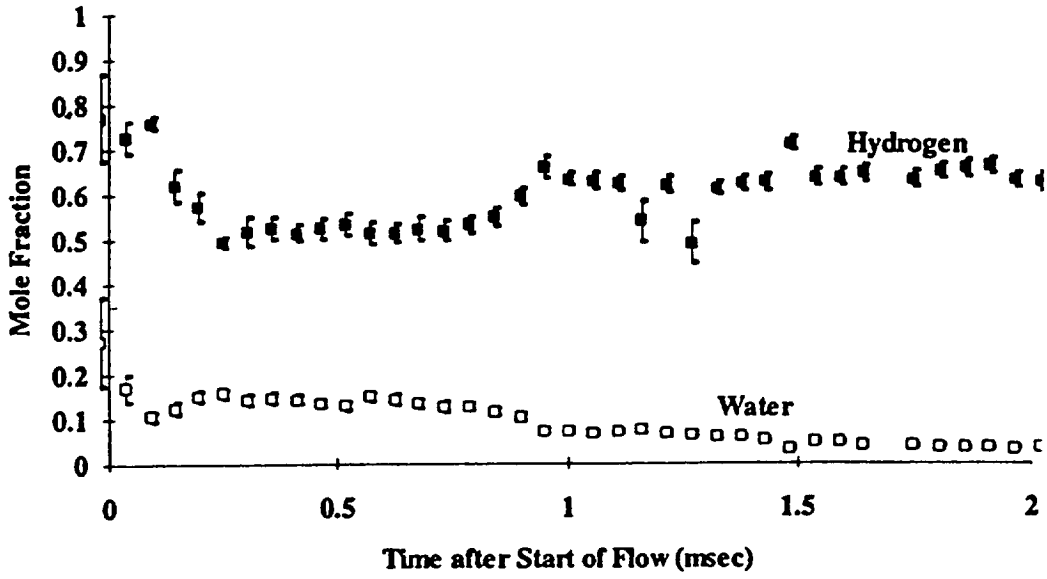


Fig. 3. Mass spectrometer records of hydrogen and water components (stagnation enthalpy = 12.2 MJ kg^{-1}, 10 mm from centre line)

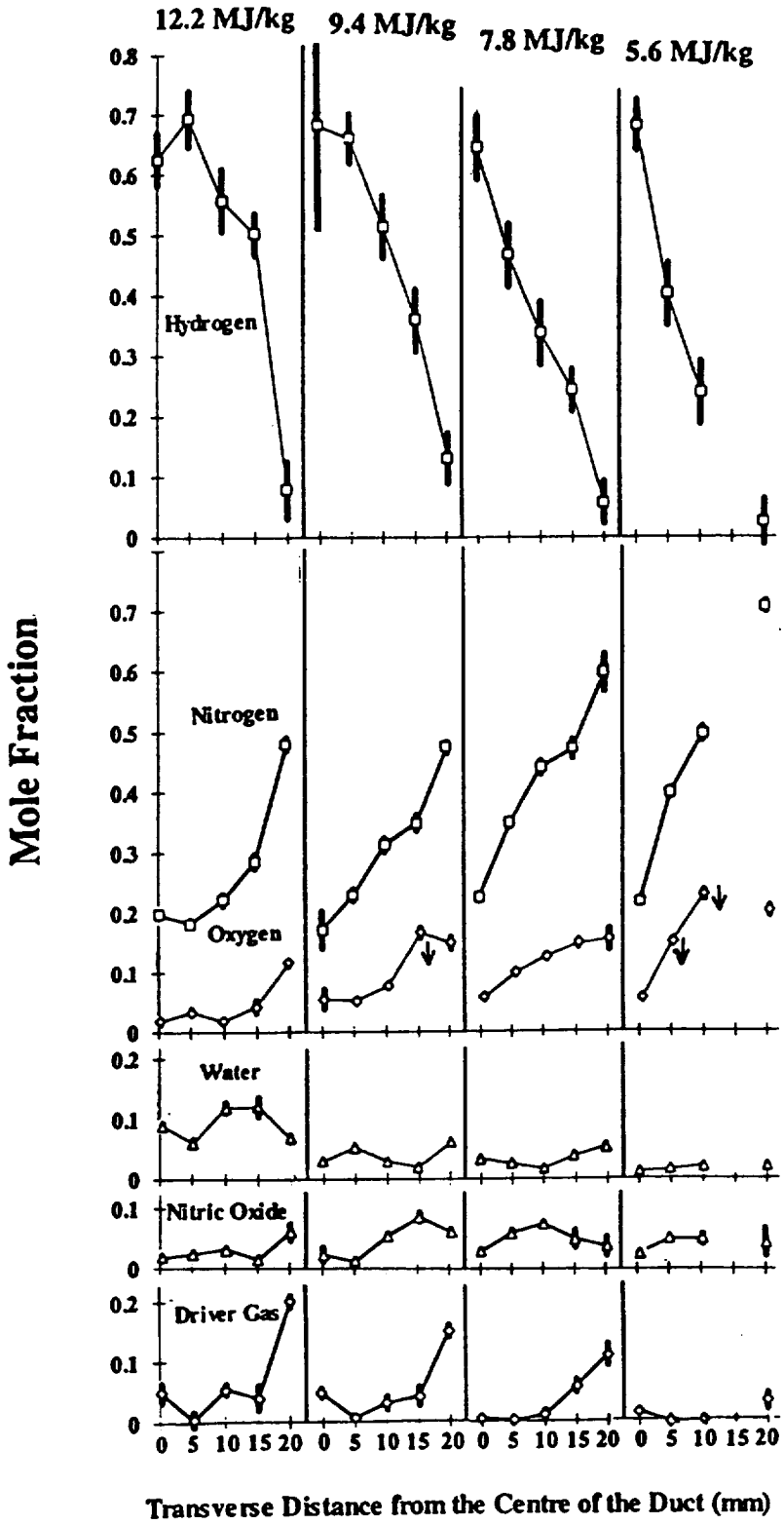


Fig. 4 Species distributions across wake.

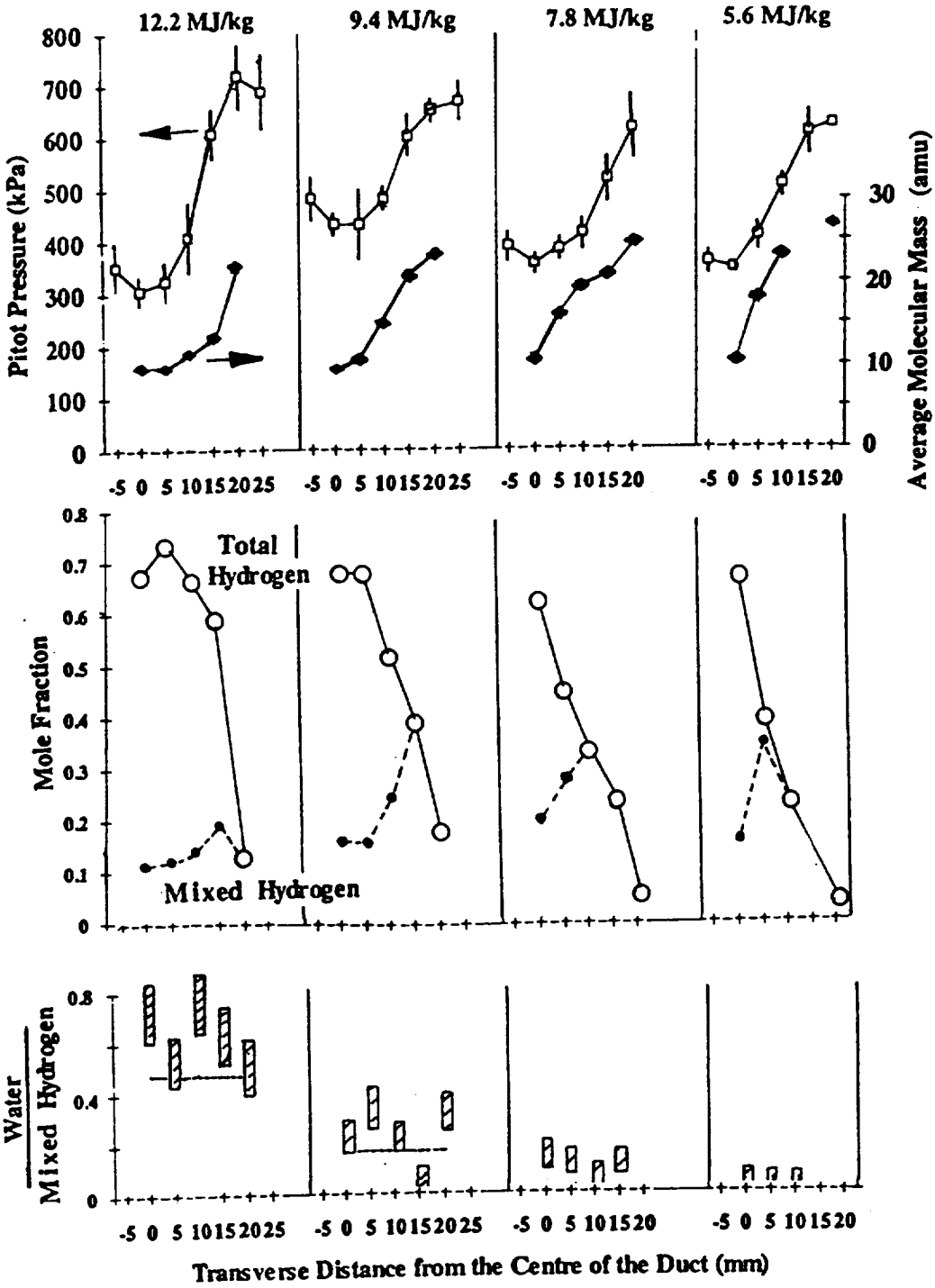


Fig.5 Diffusion of hydrogen and mixing and combustion in wake.
(Reaction efficiency: ▯ expt, ------ theory.)

AIAA 95-3152

A Skin Friction Gauge for Impulsive Flows

C. P. Goyne, A. Paull and R. J. Stalker
Department of Mechanical Engineering
The University of Queensland
Brisbane, Australia

31st AIAA/ASME/SAE/ASEE
Joint Propulsion Conference and Exhibit
July 10-12, 1995
San Diego, California

A SKIN FRICTION GAUGE FOR IMPULSIVE FLOWS

C.P.Goyne*, A. Paull# and R.J. Stalker**
Department of Mechanical Engineering
The University of Queensland, 4072
Australia

Abstract

A new skin friction gauge has been designed for use in impulsive facilities. The gauge was tested in the T4 free piston shock tunnel, at The University of Queensland, using a 1.5 m long plate that formed one of the inner walls of a rectangular duct. The test gas was air and the test section free stream flow had a stagnation enthalpy of 4.7 MJ/kg. Measurements were conducted in a laminar and turbulent boundary layer. The measurements compared well with laminar and turbulent analytical theory.

Nomenclature

A	acceleration (m/s^2)
a	shear calibration constant (V/Pa)
b	pressure calibration constant (V/Pa)
c	acceleration calibration constant (Vs^2/m)
p	pressure (Pa)
τ	shear stress (Pa/m^2)
V	voltage (v)

Subscripts

i	orientation independent
s	shear
w	wall
0	0 degrees
1	measuring element
2	acceleration element
180	180 degrees

* Graduate student. Student Member AIAA.
\# Research Fellow.
** Emeritus Professor. Fellow AIAA.
Copyright © 1995 by the American Institute of Aeronautics and Astronautics, Inc. All rights reserved.

Introduction

The accurate prediction of skin friction is of vital importance in the analysis of supersonic and hypersonic combustion ramjet performance. Pitot pressure surveys and surface measurements of heat transfer and pressure are routinely used as a means of experimentally assessing performance of combustors in high enthalpy impulsive facilities. These parameters, however, can not be conclusively used without the knowledge of viscous drag levels, particularly at higher simulated flight speeds[1]. Although methods using stress wave force balances to investigate viscous drag and net thrust levels are currently under development[2,3], measurements of skin friction at discrete locations are still required.

In order to directly measure skin friction in high enthalpy impulsive flows, an improved skin friction gauge is currently under development using the T4 free piston shock tunnel at The University of Queensland. The gauge design follows the work of Kelly et al.[4] and employs a different principle to the strain gauge type sensor used by Novean et al.[5] because a faster rise time is required.

This paper presents progress made on the new gauge in addition to measurements made in a laminar boundary layer and tentative turbulent boundary layer measurements. The experiments were conducted using a 1.5 m long flat plate. The test gas was air with a nominal free stream condition of Mach 6.2 and stagnation enthalpy of 4.7 MJ/kg.

Gauge Design and Calibration

Design

The gauge, shown in figure 1, is a piezoelectric transducer with a measuring element exposed to the flow and an acceleration

compensating element that experiences only acceleration forces. Each element consists of a lead zirconate titanate, (PZT-5H[4]), piezoceramic block, nominally 7x7x1.5 mm, glued to a 10 mm diameter, 0.8 mm thick invar disk. The invar disk has a nominal 0.16 mm gap with the gauge housing. An aluminium base is used to locate the elements in the gauge housing and the configuration results in a transducer natural frequency of 30 kHz. Apart from the piezoceramics, each of the gauge components are electrically earthed. Each ceramic is wired to an internally mounted charge amplifier which is physically isolated and electrically shielded from the test flow. The amplifiers have a decay time constant of 47×10^{-3} s.

The piezoceramic is operated in shear mode with silver electrodes on the 7x7 mm faces and a pole parallel to the 7x7 mm faces. This combination results in a polarised charge output linearly proportional to a shear stress applied to the ceramic. Theoretically, this design should produce zero pressure sensitivity. In practice, however, some pressure response is apparent.

The configuration results in a voltage output ,V_1 , linearly proportional to the shear, τ_w, pressure, p_w, and acceleration, A, applied to the measuring element according to,

$$V_1 = a\tau_w + bp_w + c_1A \ , \qquad (1)$$

where a, b and c_1 are corresponding calibration constants. The output of the acceleration compensation element, V_2, is proportional to the acceleration , A, according to,

$$V_2 = c_2A \ , \qquad (2)$$

where c_2 is the acceleration calibration constant.

The invar disk is mounted flush with the model surface and because of it's low coefficient of thermal expansion, protects the piezoceramic with little thermal stressing. Using a one dimensional heat transfer analysis it was ensured that the thickness of this component was sufficient to protect the piezoceramic from heat transfer loads before and during the test time[7].

A series of felt washers and a threaded brass sleeve are used to mount the gauge in the model. This mounting system has been designed to maximise vibration and acceleration isolation of the gauge while adequately locating the transducer within the model.

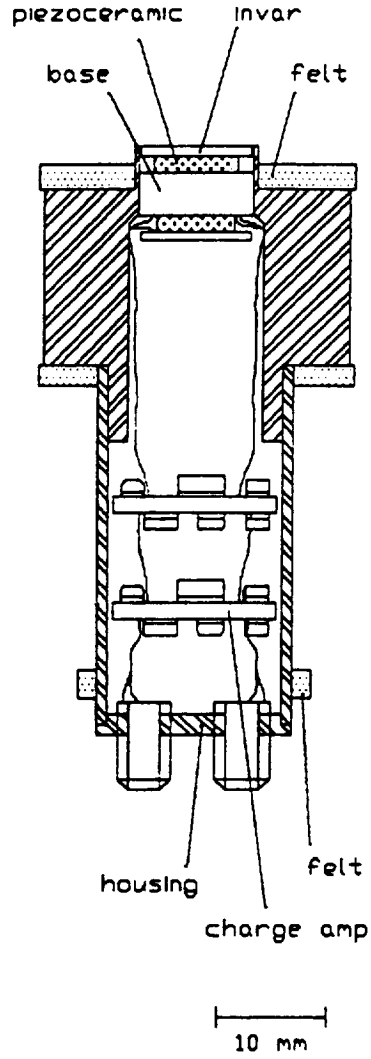


Figure 1: Schematic of skin friction gauge.

Gauge Calibration

The gauge was calibrated for acceleration, shear and pressure separately in bench tests. The developed techniques were chosen to match service conditions as closely as possible.

A calibration for acceleration was obtained by mounting a gauge in the model and impulsively loading the model with a hammer. The model was impacted over a series of tests in varying directions. It was ensured that the output of the acceleration compensation element was of

the same order of magnitude as that expected during service. By dividing the output of the measuring element by the compensating element, the ratio c_1/c_2 was obtained. Figure 2 shows a calibration run example.

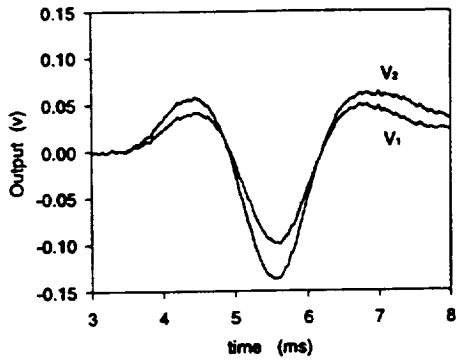


Figure 2: Typical gauge acceleration calibration, average c_1/c_2=0.7.

The shear calibration was conducted by impulsively releasing a series of known loads from the gauge measuring element. The gauge was mounted in a prone position and a cotton thread adhered to the measuring surface of the gauge. Known weights were then suspended by the thread and impulsively released. Gravity acting on each weight produced a known force and an effective wall shear stress was calculated using the surface area of the measuring disk. The output from the compensation element, V_2, was found to be negligible and using the measuring element output, V_1, the shear calibration constant, a, was determined. Step loads with 2 ms rise times were generally achieved and the calibration was repeated at 180° to confirm the results. A typical shear calibration is presented in figure 3.

Pressure calibrations were obtained using a small atmospherically driven shock tube placed over a mounted skin friction gauge. The shock tube was 430 mm long and had an internal bore of 25 mm. By manually bursting a cellophane diaphragm located on the end of the evacuated tube, the skin friction gauge was exposed to step pressure changes with rise times near 130 µs. The gauge output was compared to that of a PCB quartz pressure transducer and using equation 3 to compensate for acceleration, the pressure calibration factor, b, was obtained;

$$b = (V_1 - c_1c_2^{-1} V_2)p_w^{-1} \qquad (3)$$

A typical pressure calibration is presented in figure 4.

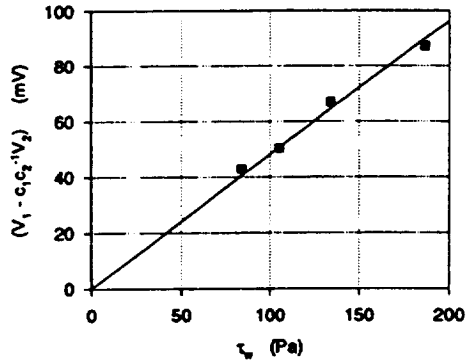


Figure 3: Typical gauge shear calibration.

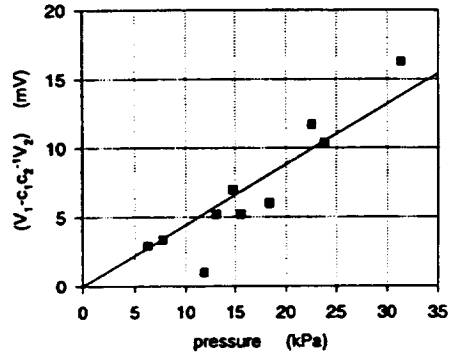


Figure 4: Typical gauge pressure calibration.

Test Facility and Model

The gauge was tested in the T4 free piston shock tunnel at The University of Queensland. The facility consisted of a 10 m long, 76 mm diameter shock tube in which the temperature and pressure of the air test gas was raised by a helium/argon driver gas. This driver gas was supplied by a free piston compression process with a reservoir pressure of 3.9 MPa and a 3 mm mild steel diaphragm. A contoured hypersonic nozzle with a 25 mm diameter throat and a 262 mm test section diameter was used.

The laminar and turbulent skin friction measurements were conducted on an instrumented 1.5 m long flat plate that formed one of the inner walls of a rectangular duct, 120 by 60 mm at the inlet. The instrumented and side walls each had a 20° sharp leading edge and the

lower wall had a 30° swept leading edge with a 20° wedge angle. To allow for boundary layer displacement, the non-instrumented walls each had a 0.5° divergence. This ensured a relatively constant pressure down the instrumented plate. The model was made of steel, except for the instrumented plate which was made of cast iron.

The skin friction gauge measurements were conducted at 370, 770, 970 and 1170 mm from the leading edge along the plate center line. A single skin friction gauge was used for the series of measurements and sealed blanks were used to fill the gauge tapping holes when not in use. PCB quartz pressure transducers and thin film heat transfer gauges were mounted axially every 50 mm, 25 mm each from the plate center line. The first measurement station was located at 370 mm from the leading edge. Five pressure transducers were located in a transverse line at 520 mm from the leading edge. The arrangement was centered on the instrumented plate with 20 mm between each transducer.

Data acquisition was conducted using the T4 data acquisition system. The skin friction gauge signals were sampled at frequencies not below 500 kHz and the pressure and heat transfer signals were sampled at frequencies not below 250 kHz.

Experimental Results and Analysis

The skin friction measurements were conducted using one gauge located at different positions during separate runs in T4. The flow conditions were nominally the same in each run. The heat transfer and pressure measurements presented in this paper are for a single run. Repeatability of the facility has been demonstrated to be less than ± 9% for a 95% confidence interval[8].

The static wall pressure, Pitot pressure and stagnation pressure were measured at 5.0 kPa, 370.1 kPa and 26.6 MPa, respectively. An example of the static wall pressure time history is presented in figure 5. A test time from 5.3 to 5.6 ms was confirmed with a steady ratio of Pitot to stagnation pressure during this time. Using ESTC[9] and NENZF[10], the test section free stream stagnation enthalpy, Mach number and static temperature were calculated to be 4.7 MJ/kg, 6.2 and 498.9 K, respectively.

Normalised pressure and heat transfer levels during the test time as a function of distance down the instrumented plate are presented in figure 6. The pressure along the plate is constant to within ±20%. The heat transfer levels indicate that transition is occurring at 470 mm from the leading edge during the test time. The levels will be shown to be consistent with that predicted by theory. The heat transfer time histories at 370 mm and 420 mm are presented in figure 7.

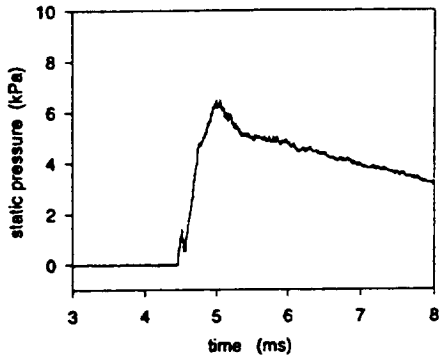


Figure 5: Static wall pressure on the instrumented plate at 370 mm as a function of time.

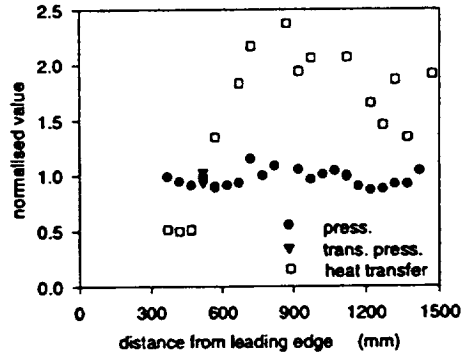
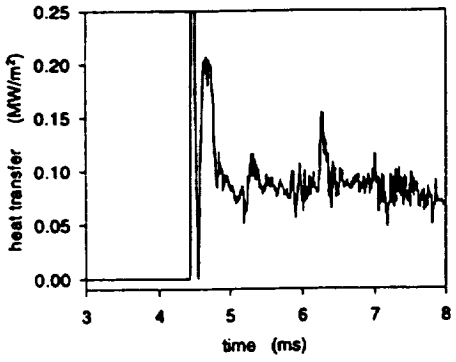
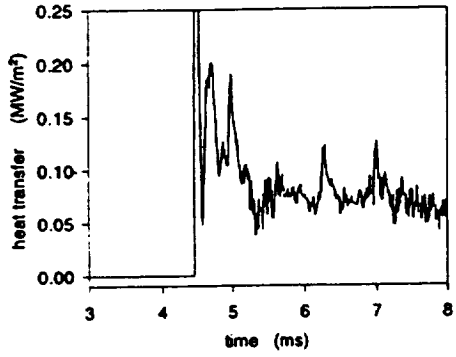


Figure 6: Static pressure, normalised by the nominal free stream static pressure, and heat transfer, normalised by 0.15 MW/m^2, down the instrumented plate during the test time.



(a)



(b)

Figure 7: Wall heat transfer history at (a) 370 mm and (b) 420 mm from the leading edge.

Figure 8 presents an uncompensated skin friction gauge output for a measurement with 0° orientation, (gauge pole facing the flow direction), at 370 mm. The calibration constants for this gauge for shear, a, pressure, b, and acceleration, c_1/c_2, were 4.78×10^{-4} V/Pa, 4.37×10^{-7} V/Pa, and 0.7, respectively. As was expected a positive signal resulted from the measuring element. After acceleration compensation of the gauge output, however, the level was found not to match the corresponding output of the gauge orientated at 180°, (figure 9), once acceleration calibrated. It is believed that this spurious effect was most likely due to heat transfer between the gauge and test flow. This effect, however, was independent of gauge orientation to the flow and could therefore be subtracted out by combining the 0° and 180° traces. This is possible because the shear components of the acceleration compensated 0° and 180° signals are equal in magnitude but opposite in sign while the orientation independent components are equal in magnitude and sign. Using equation 4, therefore, the shear component, V_s, of the signal can be extracted. V_0 is the acceleration compensated output for the 0° gauge orientation and V_{180} is the acceleration compensated output for the 180° gauge orientation;

$$Vs = 0.5 (V_0 - V_{180}) \quad (4)$$

where,

$$V_0 = (V_1 - c_1 c_2^{-1} V_2)_0$$

$$V_{180} = (V_1 - c_1 c_2^{-1} V_2)_{180}$$

In a similar manner, the orientation independent component of the signal, V_1, which includes pressure, is given by equation 5;

$$V_1 = 0.5 (V_0 + V_{180}) \quad (5)$$

The resulting shear signal, processed by equation 4, is presented in figure 10. This trace is for the gauge in the laminar region of the boundary layer, at 370 mm from the leading edge. Comparison of the trace with figure 7 confirms that the skin friction measured is following the wall heat transfer measured near the gauge, as implied by Reynolds analogy. Also shown in figure 10 is the prediction of the skin friction level using the calibration constant, a, and the theory of van Driest[11] for a laminar boundary layer. It can be seen that the measured and predicted values agree to within 20% during the test time.

With application of equation 5 to the gauge output, the orientation independent component of the gauge output is obtained. This is presented in figure 11. It can be seen that the level obtained during the test time is 45.2 mV and represents 46.5% of the original 0° acceleration compensated signal. This is much higher than the level predicted by the pressure calibration alone, 2.2 mV. It is believed that this increased level is due to heat transfer from the flow because this spurious effect followed the measured heat transfer trends and was found to be amplified in other experiments at higher stagnation enthalpies.

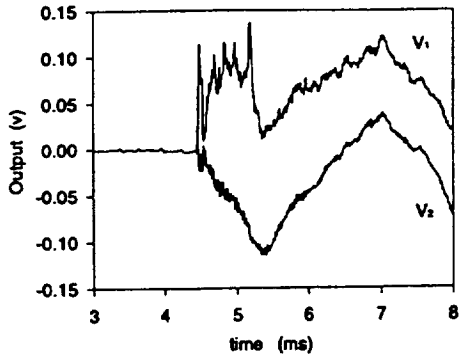


Figure 8: Uncompensated skin friction gauge output, 0° orientation, 370 mm. Measuring element, V_1, and compensation element, V_2. Time average 30μs.

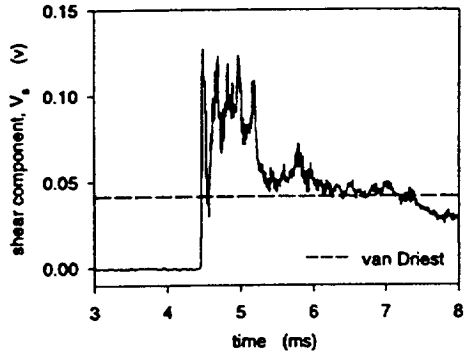


Figure 10: Processed gauge shear signal, V_s, at 370 mm, and theory of van Driest. Time average 50μs.

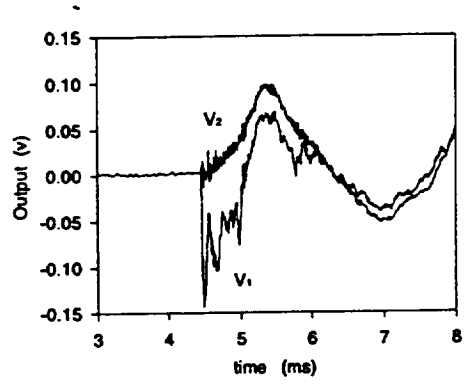


Figure 9: Uncompensated skin friction gauge output, 180° orientation, 370 mm. Measuring element, V_1, and compensation element, V_2. Time average 30μs.

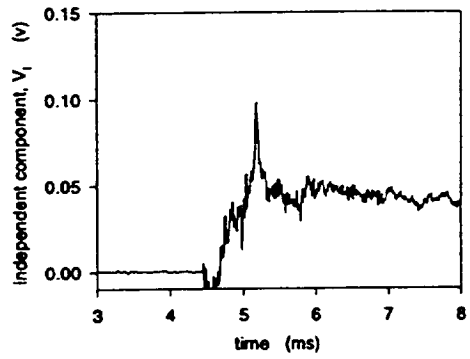


Figure 11: Processed gauge orientation independent signal, V_i, at 370 mm. Time average 50μs.

Measurements of skin friction were conducted in the turbulent part of the boundary layer at 770, 970 and 1170 mm from the leading edge. In the series of measurements, the skin friction gauge was orientated at 0° to the flow only. The turbulent boundary layer measurements are therefore considered tentative.

The gauge measurements were compensated for the spurious effect, as previously mentioned, by subtracting out 46.5% of the 0° acceleration compensated signals. Alteration of the signals in this way was justified by taking into account that the spurious effect, due to heat transfer, was measured in the laminar part of the boundary layer. It was 46.5% of the 0° acceleration compensated measurement. The amount subtracted, therefore, should scale with the heat transfer and according to Reynolds analogy, also scale with the skin friction down the plate.

These measurements and the laminar measurement are presented as a function of distance down the plate in figure 12. Also presented are predictions for turbulent wall shear by the compressible theories of White and Christoph[12], van Driest II[13] and Spalding and Chi[14]. The calculations were performed with a virtual turbulent origin at 470 mm. As a reference, the heat transfer measurements with Reynolds analogy applied are also presented. A Reynolds analogy factor of 1 was used for the turbulent boundary layer and 0.8 for the laminar boundary layer. It can be seen that the turbulent skin friction measurements fall within the range predicted by the turbulent theories. Many authors[15] recommend the theory of Spalding and Chi for high enthalpy flows on cold walls. It is interesting to note that the compensated turbulent skin friction gauge measurements agree with Spalding and Chi to within 18%.

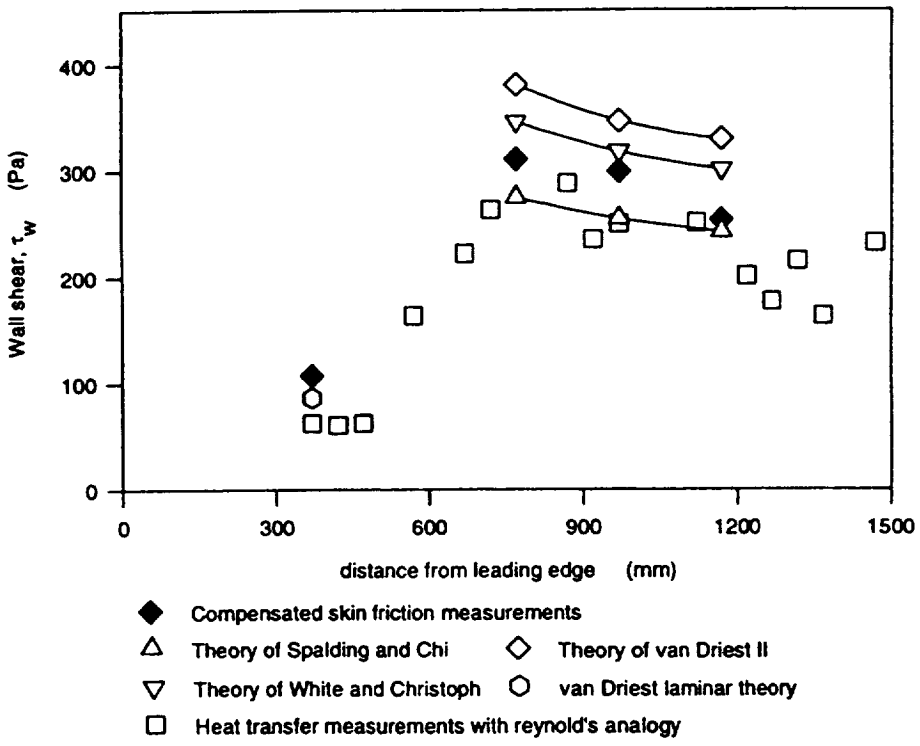


Figure 12: Skin friction gauge measurements and theory vs distance from leading edge.

Conclusions

A new skin friction gauge, designed for use in impulsive facilities, has been presented. The gauge had a natural frequency of 30 kHz and was calibrated for shear, pressure and acceleration separately in bench tests. It has been tested in the T4 free piston shock tunnel using a 1.5 m long plate that formed one of the inner walls of a rectangular duct. The test gas was air and the test section free stream had a stagnation enthalpy of 4.7 MJ/kg and a Mach number of 6.2. A spurious effect was observed in the measurements that was due to heat transfer from the test flow. A technique was devised to compensate for this effect and a compensated measurement in a laminar boundary layer agreed well with that predicted by laminar boundary layer theory.

The gauge was also used to conduct tentative measurements of wall shear in a turbulent boundary layer. The compensated measurements agreed well with compressible turbulent boundary layer theory.

Acknowledgments

The authors wish to thank the support by the National Aeronautics and Space Administration under grant NAGW-674.

References

1.Anderson, G., Kumar, A. and Erdos, J., "Progress in Hypersonic Combustion Technology with Computation and Experiment," AIAA Paper 90-5254, *Second International Aerospace Planes Conference*, October 1990.

2.Paull, A., Stalker, R. and Mee, D. "Scramjet thrust measurement in a shock tunnel," *Aeronautical Journal*, April 1995.

3.Tuttle, S., Mee, D. and Simmons, J. "Lift, Drag and Thrust Measurement in a Hypersonic Impulse Facility," AIAA Paper 94-2596, *18 th Aerospace Ground Testing Conference*, June 1994.

4.Kelly, G., Simmons, J. and Paull, A., "A Skin Friction Gauge for use in Hypervelocity Impulse Facilities," *AIAA J.* vol. 30, no. 3, 1991.

5.Novean, M., Schetz, J., Hazelton, D. and Bowersox, R., "Skin Friction Measurements in Short Duration, High Enthalpy Flows," AIAA Paper 95-6109, *6 th International Aerospace Planes and Hypersonics Technologies Conference*, April 1995.

6.Morgan Matroc Limited, "Piezoelectric Ceramics," product guide, 1995.

7.Holman, J.P., *Heat Transfer*, SI metric edition, McGraw-Hill Book Co., 1989.

8.Mee, D.J., "Uncertainty analysis of conditions in the test section of the T4 shock tunnel," Research Report No. 4/93, Department of Mechanical Engineering, The University of Queensland, Australia, 1993.

9.McIntosh, M.K., "Computer program for the numerical calculation of frozen and equilibrium conditions in shock tunnels," Department of Physics, Australian National University, Canberra, Australia, September 1968.

10.Lordi, J.A., Mates, R.E. and Moselle, R.J., "Computer program for the numerical simulation of non-equilibrium expansion of reacting gas mixtures," NASA CR-472, 1966.

11.van Driest, E.R., "Investigation of Laminar Boundary Layer in Compressible Fluids Using the Crocco Method," NACA TN 2597, 1952.

12.White, F.M. and Christoph, G.H., "A Simple Theory for the Two-dimensional Compressible Turbulent Boundary Layer," *Journal of Basic Engineering*, September 1972.

13.van Driest, E.R., "The Problem of Aerodynamic Heating," *Aeronautical Engineering Review*," October 1956.

14.Spalding , D.B. and Chi, S.W., "The drag of a compressible turbulent boundary layer on a smooth flat plate with and without heat transfer," *Journal of Fluid Mechanics*, vol. 18, pt. 1, January 1964.

15.Bradshaw, P., "Compressible Turbulent Shear Layers," *Ann. Rev. Fluid Mech.*, vol. 9, 1977.

MASS SPECTROMETER MEASUREMENTS OF TEST GAS COMPOSITION IN A SHOCK TUNNEL

K.A. Skinner* and R.J. Stalker†

Department of Mechanical Engineering, University of Queensland

INTRODUCTION

Shock tunnels afford a means of generating hypersonic flow at high stagnation enthalpies, but they have the disadvantage that thermochemical effects make the composition of the test flow different to that of ambient air. The composition can be predicted by numerical calculations of the nozzle flow expansion, using simplified thermochemical models and, in the absence of experimental measurements, it has been necessary to accept the results given by these calculations.

This note reports measurements of test gas composition, at stagnation enthalpies up to 12.5 $MJ.kg^{-1}$, taken with a time-of-flight mass spectrometer. Limited results have been obtained in previous measurements[1]. These were taken at higher stagnation enthalpies, and used a quadruple mass spectrometer. The time-of-flight method was preferred here because it enabled a number of complete mass spectra to be obtained in each test, and because it gives good mass resolution over the range of interest with air (up to 50 a.m.a.)

EXPERIMENTS

The experiments were conducted in the free piston shock tunnel T4 at the University of

* Postgraduate Student

† Emeritus Professor of Space Engineering, Associate Fellow AIAA
Department of Mechanical Engineering
University of Queensland
Brisbane 4072
AUSTRALIA

Queensland[2], using a helium-argon mixture as driver gas. The shock tube, of 10 m length and 75 mm diameter, was operated in the shock reflected mode, and supplied shock heated air to a contoured hypersonic nozzle with a throat diameter of 25.4 mm, and an exit diameter of 261 mm. As shown in fig 1(a), the mass spectrometer sampled the flow from a point on the nozzle centreline, well within the test cone of the nozzle flow field.

The stagnation enthalpy was calculated for equilibrium air from the shock speed and initial shock tube filling pressure, with an isentropic expansion to the measured nozzle reservoir pressure of 14.0±2.5 MPa. The estimated accuracy of the stagnation enthalpy was from +4% to -8%. To avoid problems with driver gas contamination of the test flow, the test time was confined to a period from 0.5 to 1.0 milliseconds after initiation of flow in the test section, and the stagnation enthalpy was limited to 12.5 $MJ.kg^{-1}$.

The mass spectrometer is described in ref.3. Essentially, it sampled the flow through a series of three conical skimmers to form a molecular beam. This was bombarded by a 250 e.V. electron beam for 200 nanoseconds every 55 microseconds, and each time a pulse of ions was produced which passed into the 1 m long drift tube, and hence to an electron multiplier detector at the end of the tube. Since the time of arrival of the ions depended on their mass, a mass spectrum of the type shown in figs 1(b) and 1(c) was obtained every 55 microseconds, and was recorded by a 50 MHz digital oscilloscope.

Peaks of N_2, 0_2, N and 0 are evident in the spectrum of fig 1(b), as well as some residual H_20. The area under each peak is proportional to the number of particles of that particular mass to reach the detector. There is clearly a problem with overlap of the peaks of N_2, N0 and 0_2, and this particularly effects measurement of the N0 peaks. Therefore some tests were made in which fewer spectra were taken, but the sampling rate of the oscilloscope was increased. The resolution was therefore improved, as shown in fig 1(c), and these spectra were used for measurements of the N0 peak.

RESULTS AND DISCUSSION

The ratio of the measurements of peak sizes is presented in fig. 2 for $0_2/N_2$, NO/N_2 and $0/0_2$. Each of the points plotted is the mean of a number of readings during a test, and therefore may be regarded as the mean of a statistical sample. The error bars indicate the standard deviation of that mean.

The measurements are compared with theoretical curves for the relative peak sizes. These were obtained by first performing numerical calculations[4] of the inviscid nonequilibrium steady expansion through the shock tunnel nozzle to yield the freestream species concentrations. These were then used to obtain values for the relative size of the mass spectra peaks. The effect of mass separation in the molecular beam was assessed by testing in the shock tunnel with known mixtures of nitrogen and helium, and nitrogen and argon. This indicated that the relative enhancement of the molecular species considered was less than 10%. The relative number of ions produced was determined from the ionization cross-sections given in table 1, and the relative efficiency with which ions were collected was taken as unity. This was checked by operating the instrument "ex tunnel" (ie. outside the shock tunnel), with the first of the three skimmers replaced by a solenoid valve, which delivered a short pulse of room air to the mass spectrometer. The measured ratio of the 0_2 peak area to N_2 peak area was 0.30 ± 0.02 which, allowing for the uncertainty in ionization cross sections, compared satisfactorily with the expected value of 0.25.

Table 1. Electron Impact Ionization Cross-Sections at 250 e.V.

Process	Cross-Section (cm^2)	Error (%)	Reference
$0_2 + e \rightarrow 0_2^+ + 2e$	1.57×10^{-16}	13	5
$0 + e \rightarrow 0^+ + 2e$	1.08×10^{-16}	5	6
$N_2 + e \rightarrow N_2^+ + 2e$	1.68×10^{-16}	8	7
$NO + e \rightarrow NO^+ + 2e$	1.89×10^{-16}	20	8

To calculate theoretical values for the peaks of atomic oxygen, the combined effect of mass separation and ion collection efficiency was obtained from the helium/nitrogen and nitrogen/argon results by assuming that these effects varied linearly with the mass ratio of the two species, yielding a factor of 2.0±0.4 for enhancement of 0 with respect to 0_2. This was applied to the predicted numerical values for relative concentrations of 0 and 0_2 and, taking account of the ionization cross-sections, the theoretical curve in fig. 2(c) was obtained. Because of uncertainties in mass separation and ion collection efficiencies, as well as in ionization cross-sections, a possible error attaches to all the theoretical curves. The limits of this are indicated by the broken lines on either side of each curve.

It will be noted that the effect of dissociative ionization of the 0_2 molecule in the mass spectrometer, with production of ionized 0 atoms, has not been taken into account in obtaining the theoretical curve of fig. 2(c). This is because the experimental results in the tunnel show the ratio of peak sizes increasing with enthalpy from a value near zero, and this is not consistent with the presence of a substantial number of 0 ions due to dissociative ionization. On the other hand, it must be observed that results of the "ex tunnel" tests shown in fig. 2(c) demonstrate that substantial dissociative ionization does indeed take place in air which is supplied from a room temperature source. It may be speculated that this difference is due to thermal excitation of the 0_2 molecules in the tunnel flow, leading to an increased velocity spread and consequent lowered collection efficiency of the 0 ions resulting from dissociative ionization. However, until this apparent anomaly is resolved, some doubt must attach to the experimental results of fig. 2(c). Therefore, not withstanding the remark made below concerning their validity, their worth is mainly in indicating the stagnation enthalpy at which the rise in 0 atom concentration due to free stream dissociation takes place.

The overall ratio of the number of atoms of oxygen in any form to nitrogen in any form can be obtained from the results in fig. 2. If the "ex tunnel" result in fig. 2(a) is used to generate a calibration factor for the $0_2/N_2$ ratio, values of 0.33±0.04, 0.27±0.03 and 0.30±0.04 are obtained

for the overall ratio at stagnation enthalpies of 8.3 MJ kg^{-1}, 10 MJ kg^{-1} and 12.5 MJ kg^{-1} respectively. The expected value is 0.27±0.05, the quoted error limits resulting from residual uncertainties in the ionization cross-sections, together with the mass separation and ion collection efficiencies, after the calibration for the $0_2/N_2$ ratio has been taken into account. Thus, the values for the overall oxygen/nitrogen ratio fall within the quoted limits of error, and provide confirmation of the experimental measurements.

It is worth remarking that, at 12.5 $MJ.kg^{-1}$, the measured $0/0_2$ value in fig. 2(c) contributes a substantial 0.08 of the total oxygen/nitrogen ratio of 0.30, thereby providing an indirect confirmation of the $0/0_2$ measurement.

It can be seen that the experimental measurements in fig. 2 generally fall outside the theoretical limits indicated by the broken lines. In fig. 2(a) the proportion of molecular oxygen exceeds theoretical limits as the stagnation enthalpy is increased. This is consistent with the results in fig. 2(c), which shows the proportion of atomic oxygen remaining at low levels for much higher enthalpies than predicted. The proportion of nitric oxide is shown in fig. 2(b), and is seen to be in excess of predicted values, at least for the range of stagnation enthalpies covered by the results. The numerical model[4] on which the theoretical curves are based gives free stream compositions which are consistent with those given by other numerical models[9]. Therefore, even when allowance is made for the experimental uncertainties, there are clear discrepancies between the theory of non-equilibrium nozzle flow and the results of these experiments, indicating a need for further experimental and theoretical work. Until these discrepancies are resolved predictions of the composition of test section flows in high enthalpy facilities should be treated with caution.

Acknowledgments

The authors gratefully acknowledge the support received from the Australian Research Council and through NASA grant NAGW-674.

REFERENCES

1. Crane, K.C.A., and Stalker, R.J, "Mass-spectrometric Analysis of Hypersonic Flows" J. Phys. D: Appl. Phys., Vol 10, 1977, pp 679-695.

2. Stalker, R.J., "Recent Developments with Free Piston Drivers". Proceedings of the 17th Int. Symp. on Shock Waves & Shock Tubes. AIP Conference Proceedings 208, New York, 1990, pp 96-105.

3. Skinner, K.A., and Stalker, R.J. "A Time-of-Flight Mass Spectrometer for Impulse Facilities" AIAA Journal, Vol 32, No 11, 1994, pp 2325-2328.

4. Lordi, J.A., Mates, R.E., & Moselle, J.R., "Computer Program for the Numerical Solution of Non-Equilibrium Expansions of Reacting Gas Mixtures", NASA CR-472, May 1966.

5. Krishnakumar, E., & Srivastara, S.K., "Cross-Sections for Electron Impact Ionization of O_2", Int. J. Mass. Spec. Ion Proc., Vol 113, 1992, pp 1-12.

6. Bell, K.L., Gilbody, H.B., Hughes, J.G., Kingston, A.E. & Smith, F.J. "Recommended Data on the Electron Impact Ionization of Light Atoms and Ions". J. Phys. Chem. Ref. Data Vol 12, 1983, pp 891-916.

7. Krisnakumar, E., & Srivastava, S.K., "Cross-Sections for the Production of N^+_2, N^+, N_2^{2+} and N^2 by Electron Impact on N_2", J. Phys. B: At. mol. Opt. Phys., Vol 23, 1990, pp 1893-1903.

8. Rapp, D. & Englander-Golden, P., "Total Cross-Sections for Ionization and Attachment in Gases by Electron Impact. I. Positive Ionization"., J. Chem. Phys., Vol 43, 1965, pp 1464-1479.

9. Sagnier, P., & Marraffa, L., "Parametric Study of Thermal and Chemical Nonequilibrium Nozzle Flow" AIAA Journal, Vol 29, No. 3, 1991, pp 334-343.

LIST OF FIGURES

Fig 1. Mass Spectrometer.

(a) Experimental arrangement

(b) Typical mass spectrum

(c) Improved resolution mass spectrum.

Fig 2. Relative Size of Mass Peaks.

(a) Molecular oxygen Vs molecular nitrogen

(b) Nitric oxide Vs molecular nitrogen

(c) Atomic oxygen Vs molecular oxygen.

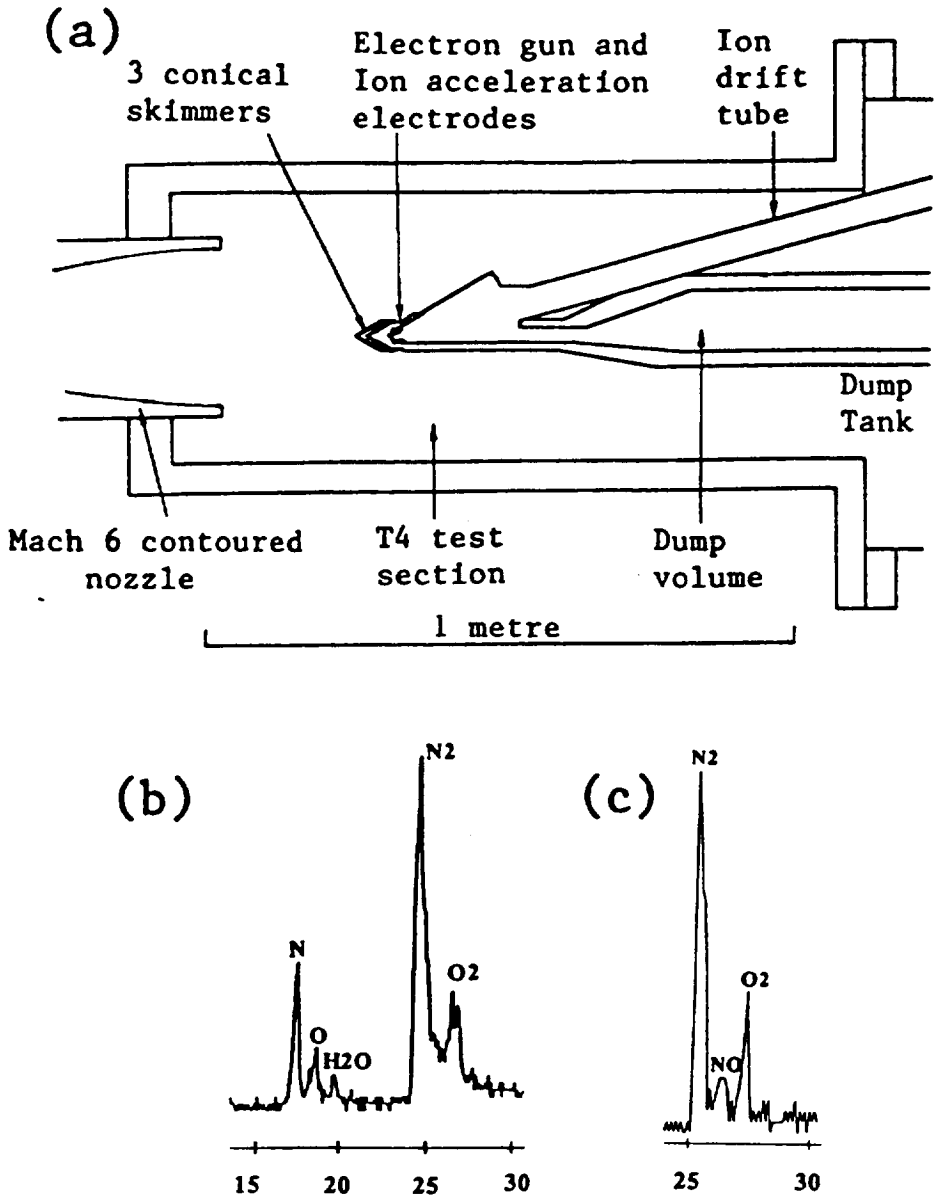


Fig 1. Mass Spectrometer.

(a) Experimental arrangement

(b) Typical mass spectrum

(c) Improved resolution mass spectrum.

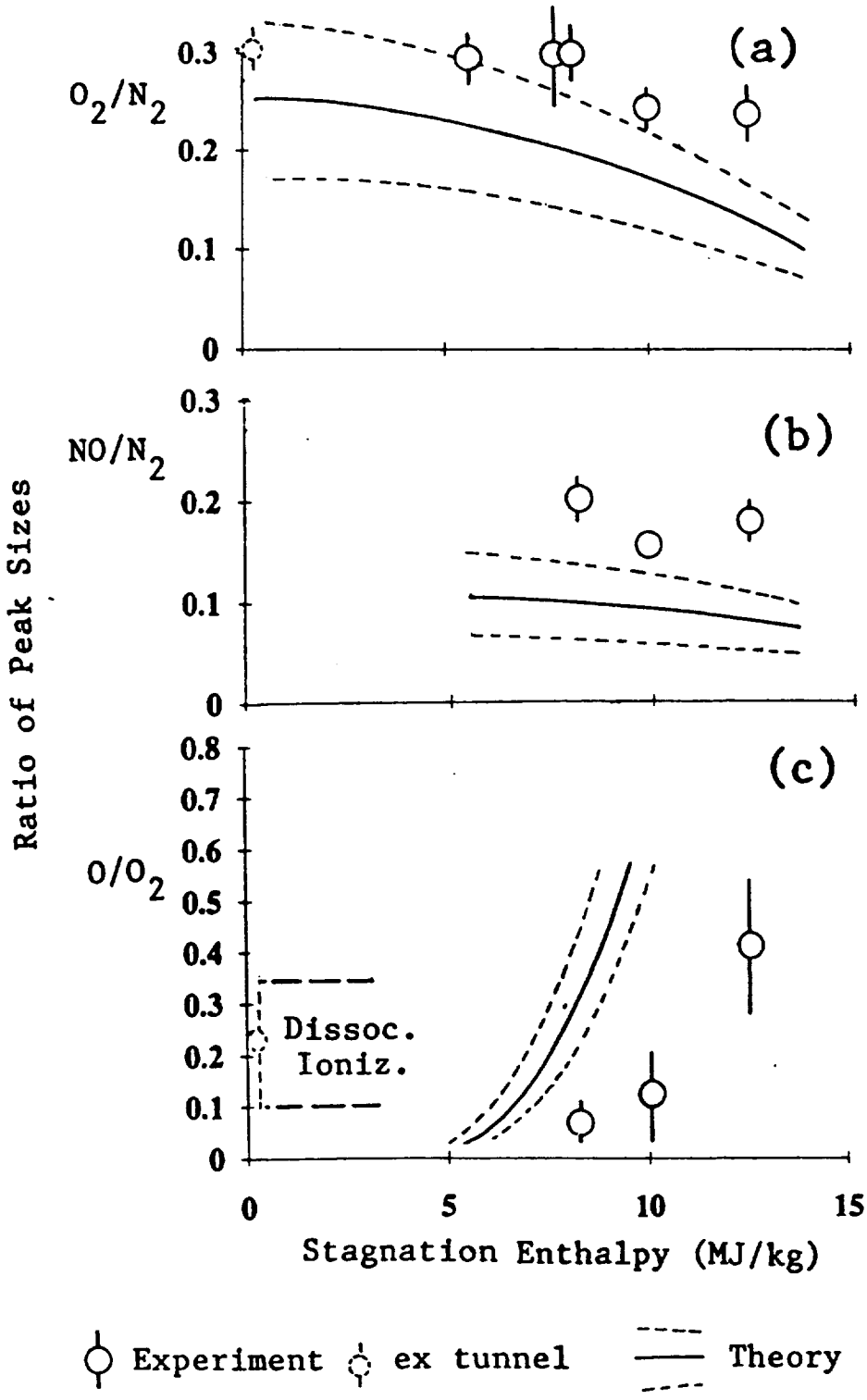


Fig 2. Relative Size of Mass Peaks.

(a) Molecular oxygen Vs molecular nitrogen

(b) Nitric oxide Vs molecular nitrogen

(c) Atomic oxygen Vs molecular oxygen.

REPORT DOCUMENTATION PAGE

Form Approved
OMB No. 0704-0188

Public reporting burden for this collection of information is estimated to average 1 hour per response, including the time for reviewing instructions, searching existing data sources, gathering and maintaining the data needed, and completing and reviewing the collection of information. Send comments regarding this burden estimate or any other aspect of this collection of information, including suggestions for reducing this burden, to Washington Headquarters Services, Directorate for Information Operations and Reports, 1215 Jefferson Davis Highway, Suite 1204, Arlington, VA 22202-4302, and to the Office of Management and Budget, Paperwork Reduction Project (0704-0188), Washington, DC 20503.

1. AGENCY USE ONLY (*Leave blank*)	2. REPORT DATE	3. REPORT TYPE AND DATES COVERED
	April 1997	Contractor Report

4. TITLE AND SUBTITLE
Shock Tunnel Studies of Scramjet Phenomena, Supplements 11 and 12

5. FUNDING NUMBERS
G NAGW-674

WU 522-51-31-10

6. AUTHOR(S)
R. G. Morgan, A. Paull, and R. J. Stalker

7. PERFORMING ORGANIZATION NAME(S) AND ADDRESS(ES)
University of Queensland
St. Lucia
Brisbane, Qld., Australia

8. PERFORMING ORGANIZATION REPORT NUMBER

9. SPONSORING / MONITORING AGENCY NAME(S) AND ADDRESS(ES)
NASA Langley Research Center
Hampton, VA 23681-0001

10. SPONSORING / MONITORING AGENCY REPORT NUMBER
NASA CR-201693

11. SUPPLEMENTARY NOTES
Langley Technical Monitor: R. C. Rogers

12a. DISTRIBUTION / AVAILABILITY STATEMENT
Unclassified/Unlimited
Subject Category 34

12b. DISTRIBUTION CODE

13. ABSTRACT (*Maximum 200 words*)

Reports by the research staff and graduate students of the Mechanical Engineering Department at the University of Queensland are collected and presented. These reports cover various studies related to the advancement of scramjet technology and the operation of advanced hypervelocity shock-expansion tubes. The report topics include the experimental studies of mixing and combustion in a scramjet flow path, the measurement of integrated thrust and skin friction, and the development of a free-piston-driven expansion tunnel capable of delivering a test gas at superorbital velocities. This research constitutes supplements 11 and 12 of the NASA Grant NAGW-674, for calendar year 1994.

14. SUBJECT TERMS
Scramjets, pulse facility, shock tunnel, expansion tube

15. NUMBER OF PAGES
159

16. PRICE CODE
A08

17. SECURITY CLASSIFICATION OF REPORT	18. SECURITY CLASSIFICATION OF THIS PAGE	19. SECURITY CLASSIFICATION OF ABSTRACT	20. LIMITATION OF ABSTRACT
Unclassified	Unclassified	Unclassified	